The Electrochemical Deposition Of Mercury On Glassy Carbon Electrodes

A thesis in partial fulfilment of the
requirements for the degree of
Masters of Science
in
Chemistry
At Massey University, Palmerston North
New Zealand

Giovanna Lucia Moretto
July 2000

ABSTRACT

The mechanism for the reduction of Hg^{2+} on glassy carbon in aqueous acetate and nitrate electrolyte was studied. This deposition process is of interest due to the wide electroanalytical applications of mercury thin film electrodes. It was found in the early stages of this work that even though the use of these electrodes is wide spread, there has been little investigation into how the deposition stage occurs.

The electrochemical techniques used were cyclic voltammetry and chronoamperometry. A range of experiments were undertaken including concentration dependence, rotation dependence, scan rate dependence, electrochemical-cleaning, and the dependence of the length of time left at open potential. The acetate experiments were carried out at a constant pH of 5.0 and all experiments were carried out at a constant temperature of 20°C.

Significant dependence was established in the cyclic voltammetry work for all the experimental conditions. In acetate electrolyte the development of peaks C1 and C2 were seen after cycling of the electrode without mechanical-cleaning. A shift in the reduction potential from a mechanically-cleaned electrode cycle to the next cycle without intervening cleaning was also observed. Two new anodic peaks, A2 and A3, were also seen in acetate electrolyte. At high concentrations cathodic current spikes were observed at the extreme cathodic limits of the voltammograms.

The response that was observed in nitrate electrolyte was dissimilar to that in acetate. The shift in reduction potential, current spikes, peaks C1, C2, A2, and A3, were never observed for the deposition of Hg^{2+} in nitrate electrolyte.

The chronoamperometry work on microelectrodes led to a number of new phenomena. Transients that were obtained from these experiments lead to the development of a quantitative nucleation and growth model for the growth of hemispherical mercury droplets. At the onset of reduction the transients follow a t^2 function which is in accordance with surface area dependence growth of the droplet. However, after a short length of time, the transients start to follow a function of $t^{1/2}$, which is suggestive of perimeter growth control. This is assumed to be due to the formation of a semi-passivating $Hg_2(OAc)_2$ film over the mercury droplet where Hg_2^{2+} forms as a result of a disproportionation reaction.

A qualitative model was also developed to account for the observations of both the microelectrode results and most of the features seen in the cyclic voltammetry work.

ACKNOWLEDGEMENTS

First, I guess that I would like to thank my chief supervisor, Dr. Simon Hall, without whom I would have never have able to finish this thesis. Thank you Simon. For all your talks (of which a lot of the time you were saying the same thing over and over just in a different way, and I still didn't get it), your guidance and support, but most of all for just being you, it didn't matter when it was, you always found time to help.

Thanks must also go to my second supervisor, Dr. Simon Brown for his encouragement, guidance, and for always having time to see me.

I would like to thank the Massey University Research Projects and Funding Committee for the Stipend and consumables money provided throughout my MSc.

I would also like to thank the Institute of Fundamental Sciences Graduate Research Fund for the support they gave me to get to Australia to carry out some research and also to all the staff in IFS for the help each of them has given me over the years.

Thanks to all the 'kids' at Massey that have made the last few years great, Massey wasn't just a place to come and work, it was somewhere to see your friends to, and now it isn't going to be the same, I will miss you all. Special thanks must go to a few people though, Jo, Paul, Ant, Emad, Michael, Gav, and Steven.

To all my friends in Welly who have given me somewhere to run away to when Palmy got to much, but mostly Claire and Del.

To Adrian for being a good friend over the years and for making chemistry fun and exciting, without you there is a good chance that I would have a BCA and would be counting beans somewhere in an office.

The biggest thanks to my friends has to go to Justin. You the man! We have been through thick and thin together over the last few years, and you have made doing this thing at Massey great. It isn't going to be the same without you kid. I'm going to miss you beating me up every second day and just being there. What ever you end up doing you will do well, and wherever you go you better stay in touch.

Gino, thanks for always being there and being the best big brother someone would have.

Lastly, but by no means by least, I would like to thank my parents. Mum, Dad, thank you so much. Without you two I would never have been able to do everything that I have done

over the last 25 years. The both of you have always believed in me, even when I didn't, and have just always been there for me. No one could ask for two better parents than the ones that I have. I love you both.

TABLE OF CONTENTS

LIST OF FIGURES

LIST OF TABLES

LIST OF SYMBOLS

Symbol		Unit
A	area	cm^2
A_s	area of a sphere	cm^2
A_h	area of a hemisphere	cm^2
A1	first anodic peak	
A2	second anodic peak	
A3	third anodic peak	
c_b	bulk concentration	mM
c_s	surface concentration	mM
C1	first cathodic peak	
C2	second cathodic peak	
D	diffusion coefficient	m^{2}s^{-1}
E	potential	mV
E_red	reduction potential	mV
E_ox	oxidation potential	mV
E_1	initial potential	mV
E_2	finial potential	mV
f	rotation rate	rps
F	Faraday constant	C mol^{-1}
h	height	cm
$[\mathrm{Hg}^{2+}]_\mathrm{bulk}$	bulk mercury concentration	mM
$[\mathrm{Hg}^{2+}]$	surface mercury concentration	mM
i	current density	mA cm^{-2}

i_{Al}	Al peak current	mA cm^{-2}
i_{d}	diffusion current	mA cm^{-2}
i_{L}	limiting current	mA cm^{-2}
i_{k}	kinetic current	mA cm^{-2}
i_{ss}	steady state current	mA cm^{-2}
I	current	mA
j	flux	m^{-2}s^{-1}
k	rate constant	m s^{-1}
k_{f}	heterogeneous electron transfer rate constant	m s^{-1}
$k_{\mathrm{red,nuc}}$	rate constant for nucleus growth	m s^{-1}
l	length of electrode	cm
M	concentration	mol L^{-1}
M	molecular weight	g mol^{-1}
n	number of electrons	
n_{Hg}	moles of mercury	mol
Q	charge	
Q_{A}	total anodic charge	
Q_{ra}	accumulated non-faradic charge	
Q_{oc}	charge where oxidation occurs	
r	radius of electrode	cm
r_{s}	radius of a sphere	cm
r_{h}	radius of a hemisphere	cm
Re	Reynolds number	
t	time	sec

t_0	time nucleus first forms	sec
x	distance	cm
x	power function	
v	kinematic viscosity	$m^2\ s^{-1}$
v	scan rate	$mV\ s^{-1}$
v	velocity of the electrode	
V	volume	cm^3
ω	angular velocity	$rad\ s^{-1}$
δ	Nernst diffusion layer thickness	cm
ρ	density	$g\ cm^{-3}$

LIST OF ABBREVIATIONS

BAS	Bioanalytical Systems Inc.
CA	chronoamperometry
CE	counter electrode
CV	cyclic voltammetry
Hg^0	mercury metal
Hg^{2+}	aqueous mercury
$Hg^{2+}{}_2$	mercurous dimer
$Hg_2(OAc)_2$	mercurous acetate
ME	microelectrode
RDE	rotating disc electrode
RE	reference electrode
rpm	revolutions per minute
SHE	standard hydrogen electrode
WE	working electrode

CHAPTER 1

Introduction

1.1 Introduction

This thesis is concerned with the electrochemical formation of thin films of mercury metal on glassy carbon electrodes. These so-called thin films (actually numerous individual droplets) find use in a number of electroanalytical techniques, in particular polarography and anodic stripping voltammetry.

1.2 Overview of polarography

Polarography is a particular type of voltammetry that was developed by the Czechoslovakian chemist Jaroslav Heyrovsky in the early 1920s [1, 2].

In voltammetry, a variable potential excitation signal is impressed upon an electrochemical cell containing an electrode. This excitation signal elicits a characteristic current response upon which the quantitative and qualitative analytical method is based.

The signal is due to the reduction of the analyte (usually a metal) from a solution species $M^{n+}{}_{(aq)}$ to the zero oxidation state as a mercury amalgam

$$M^{n+}{}_{(aq)} \quad + \quad ne^- \quad \rightarrow M(Hg) \tag{1.1}$$

A steady state current or plateau on the polarography curve is determined by the mass transport of the analyte to the electrode and is proportional to the bulk analyte concentration. This current is also proportional to the droplet surface area.

In linear scan polarography the applied potential is changed linearly as a function of time. The current is monitored continuously and the complicated signal is recorded as bulk mercury droplets (typically 0.1 – 2.0 mm diameter) form and then drop off. Linear scan polarography is the simplest polarographic technique and allows detection of analytes to 2×10^{-6} M. With more rigid control of the mercury droplet through use of mechanical piston burette, together with current sampling over the last 5 ms of each droplet, detection limits may be decreased to 1×10^{-6} M.

More recent developments have incorporated this current sampling concept and aim to further decrease the detection limit. These have been based on modifying the applied potential waveform from the simple linear function. In the case of normal pulse polarography each new droplet experiences a different potential as a short 60 ms pulse at the end of the 2 second life of the droplet. This decreases the non-faradaic noise contribution of the overall response and hence increases the diffusion related response and increases the signal to noise ratio. The detection limit is consequently lowered to 5×10^{-7} M for this technique.

Differential pulse polarography is an adaptation of normal pulse and records the difference between two successive potential pulses. This permits cancellation of the non-faradaic current whilst retaining the enhanced faradaic response. Detection limits with differential pulse are generally two to three orders of magnitude lower than those for linear scan polarography and lie in the range of 10^{-7} to 10^{-8} M. This type of polarography is also widely used in the field of electroanalytical chemistry [3,4,5].

1.3 Stripping voltammetry

Despite the marked improvements in detection limits in polarography with the development of controlled droplet growth and potential pulse techniques, these are not sufficient in most cases to satisfy the need for even lower detection limits in many applications - in particular environmental - where concentration of less than 1×10^{-9} M may be required.

One of the main analytical methods for the analysis and detection of metal ions in solution is that of stripping voltammetry. Stripping voltammetry methods have been developed to achieve these goals. In anodic stripping voltammetry (ASV), the analytical response arises not from the reduction step described by equation 1.1 but by the deliberate and controlled oxidation of the reduced analyte

$$\mathrm{M(Hg)} \rightarrow \mathrm{M^{n+}_{(aq)}} + n\mathrm{e^-} \qquad (1.2)$$

This is known as the stripping step.

The formation of the analyte amalgam with mercury takes place over long periods of time and may be in a separate electrolyte from that which originally contained the analyte. This effectively provides a pre-concentration method where the analyte is transferred from a very dilute solution to a thin amalgam layer on the mercury droplet electrode

Cathodic stripping voltammetry (CSV) is the opposite of ASV. Here the analyte is pre-concentrated on an oxidising step and stripped in a reducing step.

Adsorptive stripping voltammetry (AdSV) is similar to ASV and CSV. Deposition of the analyte occurs by a physical adsorption on the electrode surface rather than by electrolytic deposition and may not involve reduction or oxidation. The analytes form complexes rather than an amalgam on the electrode surface. The stripping step of this adsorbed layer may involve either reduction or oxidation. The key point in AdSV is that the complex formation must be reversible. Both surface-active organic compounds and inorganic ions have been determined in different matrices using this method [6].

Combinations of these techniques have been shown to b used by Ghoneim [7], where differential pulse ASV was first used with a HDME, followed by differential pulse CSV for the detection of a different analyte in the same sample solution.

1.4 Mercury based electrodes

One of the main advantages with using mercury-based electrodes for polarographic analysis techniques is that mercury has one of the least electronegative potentials in the electrochemical series. This determines that the mercury electrode will remain in the Hg^0 state while most metals for analysis may be selectively alternated between the zero and higher oxidation states. A second major advantage with the use of mercury metal electrodes in aqueous or protic solutions is the markedly low rate of hydrogen production at these electrodes compared to other metals. The exchange current density for hydrogen reduction on mercury is 12 orders lower than that on Platinum for example [8].

The liquid presentation of mercury metal has several advantages over other metals. First, the high surface tension ensures a predicable surface area for an electrode. Secondly, the possibility of irreversible contamination adsorption on the electrode surface need not be a concern since the electrode can frequently be discarded and reformed. The range of liquid mercury-based electrodes include dropping mercury electrodes (DME), hanging drop mercury electrodes (HDME), and controlled growth mercury electrodes (CGME) [9].

In that range of liquid mercury-based electrodes the sample solution requires stirring to control the hydrodynamic effects. Controlling this hydrodynamic effect can be overcome using different methods other than stirring. Brett [10] has used ultrasonic radiation of the sample, which he has shown, causes high mass transport and leads to enhanced sensitivity. MTFE have been used in conjunction with flow injection systems where the hydrodynamics are controlled by the flow through a small cavity of fixed and known diameter [11-15]. Mercury microelectrodes are also used which have good hydrodynamic control. Hemispherical diffusion is obeyed with these electrodes therefore no stirring is required [16].

As recently as 1990, mercury was readily available in a relatively low-cost high purity form. However since this time with the increase in health and safety legislation worldwide and the banning of airfreight of this material mercury has become expensive to purchase and dispose of.

These economical considerations have lead to the development of alternative concept to bulk mercury electrodes - that of mercury thin film electrodes (MTFE) formed on inert but conductive electrode substrates. The previous advantage of the ability to frequently reform new droplets from a capillary column has been obviated through the increased use of stripping techniques. Here mercury is employed either as a CGME or HDME where individual droplets are retained over the entire analytical cycle. Also, it was recognised that the key feature for electrochemistry was the surface of the mercury droplet rather than the bulk. Considerable work has been undertaken to explore the use of MTFE with low loading of mercury [17-20]. It is generally assumed by many electroanalytical chemists that a film of mercury is formed. There is strong microscopy evidence however, showing that the mercury is present in the form of droplets [21]. Hence the word 'film' is a misnomer since it is numerous closely packed small droplets which are found to form leading to high surface area, the use of the term MTFE, however, remains.

Many electrode substrates can be used for MTFE work, such as Platinum [22], but the substrate of choice is glassy carbon (GC). Here, MTFE are usually formed prior to the analytical task by electrochemical reduction of Hg^{2+} solution at GC electrodes.

$$Hg^{2+} + 2e^- \rightarrow Hg_{(l)} \qquad (1.3)$$

According to Stulikova [23] nucleation preferentially occurs at active sites on the GC material and adatom deposition leads to droplet formation. There has been little discussed about the nature of the active sites.

1.5 Glassy Carbon

Glassy carbon electrodes were applied for the first time in electroanalytical chemistry by Zittle and Miller [24]. In 1962, Yamada and Sato prepared a gas-impermeable carbon which they called 'glassy carbon' [25]. This was manufactured by slow pyrolsis of phenolic resins under vacuum.

Glassy carbon is generally formed by means of a carefully controlled heating of the polymeric (phenolformaldehyde) resin in an inert atmosphere [26]. At temperatures above 300°C oxygen and nitrogen are removed (300-500°C) and the carbonization process commences [27]. This carbonization process must occur slowly to ensure that the gaseous products can all diffuse to the surface. Hydrogen is then eliminated between 500 and 1200°C. This last elimination and heating process leaves behind the final product, glassy carbon.

Glassy carbon has interesting physical properties in comparison with other carbons such as impregnated carbon, as shown in Table 1.1 [28]. Depending on the method of formation various shapes can be produced. For example, glassy carbon produced at higher temperatures is far less susceptible to chemical oxidation than graphite. In combination with having very small pore-size and inertness to chemical attack, glassy carbon makes an attractive material for the preparation of inert electrodes. The low porosity prevents contamination of the electrode material

Jenkins and Kawamura [29] by means of X-ray diffraction, infrared spectroscopy and the determination of hardness, Young's modulus and tensile strength have extensively studied the formation of the final structure of glassy carbon. From their studies they concluded that glassy carbon is made up of aromatic ribbon molecules, which are oriented randomly and tangled in a complicated manner [28]. Figure 1.1 shows a schematic structural model for

	Glassy carbon	Impregnated carbon
Heat proof to (°C)	1300	1300
Hardness	4–5 (Mohs)	45–55 (Shore)
Tensile strength (kg cm^{-2})	500-1000	400-500
Ash content (%)	0.1	0.2
Coefficient of thermal expansion (10^{-6} K)	1.8–2.2	2.0–2.5
Gas permeability ($\mathrm{cm}^2\ \mathrm{s}^{-1}$)	10^{-11}–10^{-12}	10^{-4}–10^{-6}

Table 1.1 Some properties of glassey carbon in comparison with impregnated carbon [28].

glassy carbon [30]. It can be seen from Fig 1.1 that these ribbon molecules twist, bend, and intertwine, yielding to the end product of glassy carbon.

Glassy carbon has been shown to have the widest potential range of all carbonaceous electrodes [31], a wider potential range than platinum, other metals, and semiconductors [32]. This factor, with those of low porosity, high conductivity, chemical inertness and hardness, makes GC the most attractive material to use with MTFEs.

Glassy carbon electrodes with MTFs have also been used in conjunction with substances which chemically modify the electrode surface [5]. It is thought in some areas that the use of polymers on GC electrodes protects the surface against fouling [33,34]. Polymer coatings are also not only thought to protect the GC electrode surface but the MFTE itself [35]. Most commonly it appears to be organic polymers that are used to coat the GC electrodes, for example, poly (ester sulfonic acid) [36], and nafion [34]. Although organic coating appear to be most common this technique is not limited to only organic products as bismuth has been used as a coating material [37].

1.6 Reasons for this work

There have been a many advancements and successes in the use of mercury thin films electrodes over the last 25 years. MTFEs have all but replaced the use of the HDME at the present point in time and have been used in a wide variety of applications. One of these was a study using anodic stripping semidifferential electroanalysis [38]. This study showed that the reproducibility and sensitivity achieved using MTFEs is far superior to those with HDMEs. MTFEs can also capable of being used with a variety of samples including natural waters, blood, blood plasma and urine [39]. MTFE's can perform multi-analyte analysis well, with the simultaneous determination of Ni^{2+} and Co^{2+} as an example [40].

These successes, however, have been entirely focused on the post-production use of the MTFE. Mercury deposition onto GC electrodes from aqueous chloride media was studied has been studied using a electrochemical quartz crystal microbalance (EQCM) [41], but little work has been undertaken to gain understanding of the events leading to the preparation of MTFE, that of the nucleation and growth of mercury droplets on GC-henceforth described as the 'deposition' process in this thesis.

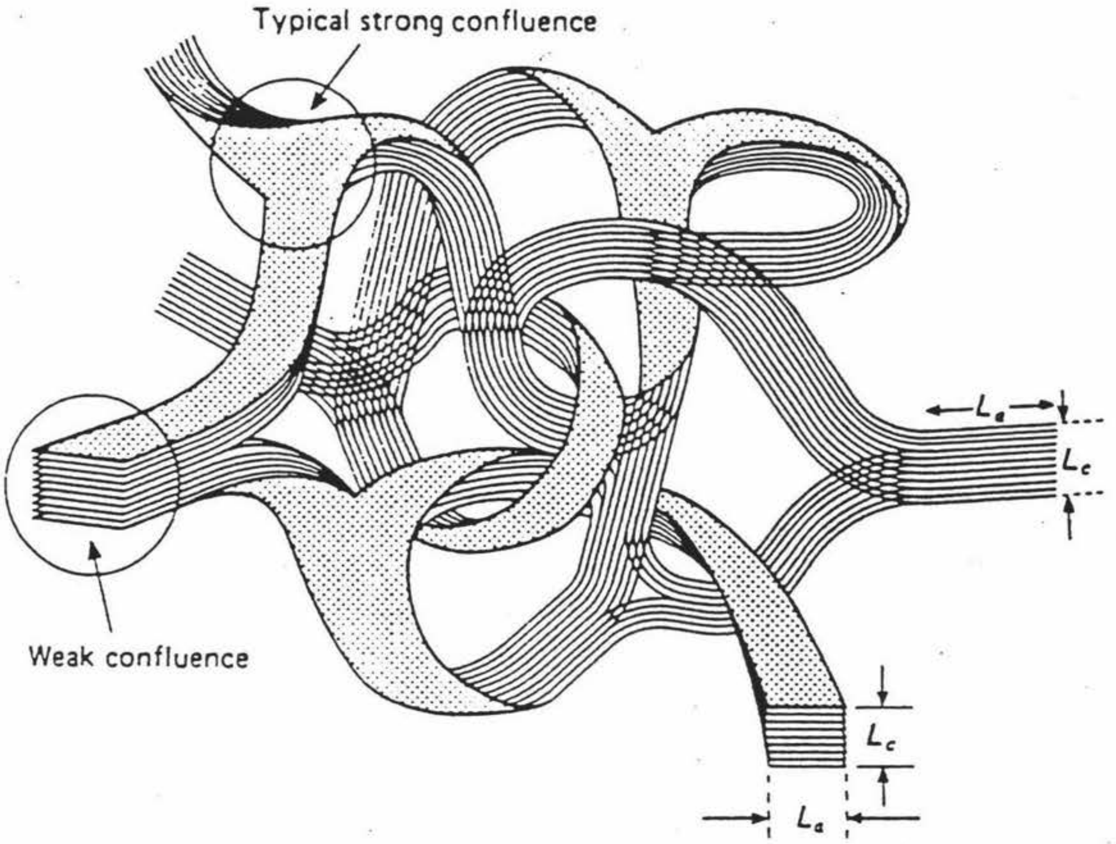

Fig 1.1 Schematic structural model for glassy carbon [30].

Those using MTFE's for electroanalytical purposes report wide ranging conditions, without comment or regard to selection of these for the deposition of mercury on GC. A direct communication with Fielden in 1998 [42] helped confirm that in many cases there is really no experimentally sound reason for selection of the conditions. Table 1.2 and Table 1.3 provide an overview of a selection of conditions reported for this process. It is likely that the mercury concentration, electrolyte, deposition time and potential, hydrodynamic conditions, and degassing of the solution, all will contribute to the final presentation of the MTFE. In the cases reported in both Tables 1.2 and 1.3, the deposition of mercury was done prior to the analyte deposition. The deposition step is not always undertaken in this manner [63,64]. When the deposition of mercury is combined with the deposition of the analytes the stripping step will not be as well defined. This is due to the fact that there is analyte in its zero oxidation state may diffuse throughout the mercury during the deposition stage. Not all the analyte will be at the surface during the stripping step.

Many features can be seen in Tables 1.2 and 1.3. The first significant feature is the number of 'not stated', (n/s), symbols in the tables. This strongly indicates that conditions leading to the deposition of the MTFEs are frequently not reported in the literature. A very wide range of mercury concentrations, [Hg^{2+}], appear to be used throughout by these electroanalytical chemists. There is also a great variation in deposition times, though from these tables it appears that with increased mercury concentration there is a decrease in the deposition time used in general. There are wide ranging deposition potentials with no apparent trends. The seemingly few times that it was stated that the solution was stirred, wide ranging rotation rates were reported. In the case of the supporting electrolyte there is also a wide variety in what was selected. In most cases the pH of the supporting electrolyte was not stated.

This means that the pH of the deposition solution is not important. It is also uncertain from the conditions stated if the need for the degassing of the solution prior to, and during, the deposition step is important or not.

The work undertaken in this thesis was to investigate the effect of the mercury concentration, potential, hydrodynamic conditions and electrolyte on the nucleation and growth of mercury on GC electrodes. The second aim of this work was to propose a mechanism for the deposition process.

$[Hg^{2+}]$	Supporting electrolyte	Deposition Time	Deposition Potential	Stirring	Degassed	Reference
n/s	n/s	n/s	n/s	n/s	n/s	43
100 mg L^{-1}		20 sec at each 0.1 interval followed by 4 min	−0.2 to −0.8 V followed by −1.0 V vs n/s	Stirred for 4 min	n/s	44
n/s	n/s	600 sec	10 mV s^{-1} scan from −0.97 +0.10 V vs n/s	n/s	n/s	45
100 mg L^{-1}	0.5 M HCl	8 to 15 min	−0.90 V vs Ag/AgCl	n/s	n/s	46
5 mg L^{-1}	n/s	3 min	−1.0 V vs Ag/AgCl	rotation	Argon	21
1 mM	0.1 M KNO_3 0.01 M HNO_3	2 min	−1.0 V vs Ag/AgCl	10 Hz	n/s	40
10 mM $Hg(NO_3)_2$	100 mM KNO_3 10 mM HNO_3	10 min	−0.90 V vs Ag/AgCl	1800 rpm	n/s	38
8×10^{-4} M Hg^{2+}	Acetate buffer	5 min	−0.25 V vs Ag/AgCl	3600 rpm	N_2	39

Table 1.2. A summary of the range of mercury deposition conditions carried out on non-modified GC electrodes reported in the literature. Where conditions are not stated this is indicated by n/s.

[Hg^{2+}]	Supporting electrolyte	Deposition Time	Deposition Potential	Stirring	Degassed	Reference
1 x 10^{-4} M	1 x 10^{-3} M KNO_3	10 min	−1.1 V vs Ag/AgCl	400 rpm	n/s	47
1 x 10^{-3} M[1]	0.1 M KNO_3 0.01 M HNO_3	60 sec	n/s			48
80 mg L^{-1}	0.02 M HCl	15 min	−0.90 V vs SCE	stirred	Not degassed	49
1 x 10^{-4} M	0.1 M KNO_3 5 mM HNO_3	n/s	−1.0 V vs Ag/AgCl	n/s	n/s	50
n/s	n/s	n/s	n/s	n/s	n/s	51
1 mM	0.10 M HCl	60 sec	−1.00 V vs SCE	stirred	n/s	52
0.10 M	0.10 M KNO_3 0.002 M HNO_3	60 sec	−1.00 V vs SCE	n/s	n/s	53
n/s	n/s	n/s	n/s	n/s	n/s	20
0.5 mM	0.1 KCl	n/s	n/s	n/s	n/s	54

Table 1.2 (continued)

$[Hg^{2+}]$	Supporting electrolyte	Deposition Time	Deposition Potential	Stirring	Degassed	Reference
1 mM	0.1 M KNO_3 0.001 M HNO_3	n/s	n/s	n/s	n/s	55
0.1 M	0.1 M KNO_3 0.002 M HNO_3	60 sec	-1.0 V vs SCE	n/s	n/s	34
10 mM $Hg_2(NO_3)_2$	pH < 1 acidificed with nitric acid	n/s	−0.2 V vs Ag/AgCl	n/s	n/s	56
n/s	n/s	n/s	n/s	n/s	n/s	57
2.2×10^{-5} M	n/s	10 min	−900 mV vs Ag/AgCl	n/s	n/s	58
5×10^{-4} M	0.07 M acetate pH = 4	6 min	−800 mV vs Ag/AgCl	n/s	n/s	59
2.5×10^{-5} M	Acetate buffer	10 min	−1.0 V vs SCE	n/s	degassed	60
5×10^{-4} M	0.07 M acteate buffer pH = 4	6 min	−800 mV vs Ag/AgCl	n/s	n/s	61
1 mM	0.1 $HClO_4$	n/s	0.0 V vs NaCl calomel electrode	n/s	N/S	62

Table 1.3 A summary of the range of mercury deposition conditions carried out on either modified GC electrode or on other electrode surfaces reported in a sample of the literature. Where conditions were not stated this is indicated by n/s.

balance the faradaic process at the WE but in the opposite direction (i.e. if oxidation occurs at the WE then an equal amount of reduction will occur at the CE). The processes at the CE are of no interest usually and they do not have an influence on the processes occurring at the WE. The reference electrode monitors the potential change in the WE relative to its own potential by circuit combination with the potentiostat. The potential of the WE is quoted with respect to the RE unless otherwise stated.

2.3.1 *Working electrodes*

The electrochemical cells used in this work consisted of three electrodes where the electrochemical reactions of interest occur at the WE with the generation of a faradaic current due to electron transfer processes.

2.3.1.1 Rotating Disc Electrode

A glassy carbon disc electrode (RDE) which had a geometric area of 0.0615 cm^2 (Bioanalytical Systems Inc., West Lafayette, Indiana, USA) was used for the cyclic voltammetry and chronoamperometry experiments. For each set of CV experiments the RDE was cycled on CV mode seven times from +1000 mV to −1000 mV and back to +1000 mV, with a rotation rate of 1000 rpm, and a scan rate of 100 mV, to achieve a constant response. By the end of seven cycles the response being achieved was constant.

All the RDE system electrochemical measurements were made in 150 cm^3 of the mercury solutions in a specially designed water-jacketed cell (IFS Glassblower Workshop, Massey University) maintained at the desired temperature with a circulating water bath (Colora, Messtecknik, GMBH, Germany) and monitored with a calibrated thermocouple.

2.3.1.2 Microelectrodes

A BAS MF-2007 glassy carbon microelectrode (ME) with a mean diameter of 11 μm (± 2 μm) (Bioanalytical Systems Inc., West Lafayette, Indiana, USA) was used as the WE in a number of experiments of varying concentrations and rotation rates. The carbon fiber that is used to form the electrode when formed comes out oval in nature, so the mean diameter is

CHAPTER 2

Experimental Methods

2.1 Introduction

The focus of this chapter is to provide an overview of the electrochemical methods and experimental conditions used in this study of the electrochemical deposition of mercury on glassy carbon working electrode. This was performed in two different aqueous electrolytes, (potassium nitrate and sodium acetate), buffers at a fixed temperature of 20°C, and over a range of concentrations and rotation rates. The two main electrochemical techniques used in this work were cyclic voltammetry (CV) and chronoamperometry (CA).

Two different types of glassy carbon electrodes were used in this study: planar rotating disc and microelectrode.

2.2 Instrumentation

2.2.1 *Potentiostatic Equipment*

During this work one type of potentiostat was used for the experiments involving rotating disc electrode and microelectrodes. This potentiostat was a BAS 100B/W Electrochemical Analyzer and accompanying BAS 100 B/W Version 2.0 software (Bioanalytical System Inc., West Lafayette, Indiana, USA).

2.3 Electrode Systems

The electrochemical cells used in this work were made up of three electrodes; a working electrode (WE); a reference electrode (RE); and a counter electrode (CE). In these cells the potential of the WE is determined by the use of a potentiostat that controls the potential difference between the WE and the RE by altering the current flowing through the WE and CE. The RE serves purely as a reference potential and does not pass current [65].

The electrochemical reactions of interest occur at the WE with the generation of a faradaic current due to electron transfer processes. The CE is driven by the potentiostatic circuit to

1.7 Organization of this thesis

The format of this thesis has separated the results and discussion from each other. Chapters 3 and 4 report the results for cyclic voltammetry and chronoamperometry respectively. This format was adopted since the discussion of this work has numerous cross-references to both results chapters. This discussion and presentation of the proposed mechanism is given in Chapter 5. Chapter 2 provides details of the experimental conditions and equipment.

The other formatting decision worthy of note is that of the voltammograms displayed in Chapter 3. All have been produced in a landscape format. This was deemed necessary since a relatively wide potential range (x-axis) was used (+1000 to −1000 mV) with features occurring near both potential limits. The use of portrait presentation would unnecessarily contract the visual presentation.

11 µm with a cross-section range of 9 to13 µm. The mechanical polishing and the cycling was identical to that employed for the RDE.

In comparison to conventional size electrodes the special properties of microelectrodes have widened the range of analytical possibilities in different techniques [66]. Main advantages derived from their use can be summarized:

1) Very small currents (rates of electrochemical reaction) can be relatively easily measured

2) The *iR* drop in solution is reduced at small electrodes

3) Capacitance charging currents, the limiting factor of the sensitivity which can be reached in all the transient electrochemical techniques are reduced to insignificant proportions allowing a better discrimination of the faradaic current

4) The rate of mass transport to and from the electrode surface increases as the electrode size decreases. Steady state of mass transfer is rapidly established. Due to both reduced capacitative charging currents and increased mass transport rates ME exhibit a very good signal to noise ratio.

The purpose of using a ME in this work was to evaluate the effect of this enhanced mass transport on varying concentration ℨ scan rate. The ME was placed in a 60 cm^3 cell inside a Faraday cage (Bioanalytical Systems Inc., West Lafayette, Indiana, USA) to minimize noise from external sources which might interfere with the current-potential wave. The microelectrode was connected to a pre-amplifier (PA-1, Bioanalytical Systems Inc., West Lafayette, Indiana, USA) to amplify the small currents, and controlled by the 100 B/W potentiostat. All of the microelectrode work was performed with static electrodes in unstirred solutions, at 20°C.

2.3.2 *Counter electrode*

A piece of platinum wire was used as the counter electrode throughout the course of this study. The CE is driven by the potentiostatic circuit to balance the faradaic process at the WE but in the opposite direction (i.e. if oxidation occurs at the WE then an equal amount of reduction will occur at the CE). The processes at the CE are of no interest usually and they do not have an influence on the processes occurring at the WE.

2.3.3 *Reference electrode*

A 3 M NaCl Ag/AgCl gel electrode (Bioanalytical System Inc., West Lafayette, Indiana, USA) with potential +197 mV *vs* the standard hydrogen electrode (SHE) was used as the RE in the electrochemical cell. The reference electrode monitors the potential change in the WE relative to its own potential by circuit combination with the potentiostat. The potential of the WE is quoted with respect to the RE unless otherwise stated.

2.4 Working electrode pretreatment

2.4.1 *Mechanical pretreatment*

Mechanical cleaning of the electrodes was always undertaken prior to a sequence of experiments unless otherwise stated on both the RDE and microelectrode.

2.4.2 *Electrochemical pretreatment*

Another technique that was available to us in this work was the use of electrochemically cleaning the electrode system using the BAS system. This system works by specifying a cleaning potential and a cleaning time, and then the electrode is exposed to the given potential for the specified time, with the aim of oxidising material off the surface of the electrode.

2.5 Mass transport and the Levich Equation

The RDE consists of a disc electrode embedded in the centre of a plane surface vertically mounted on the shaft of a synchronous digitally controlled motor in the RDE-1 device

(Bioanalytical Systems Inc., West Lafayette, Indiana, USA). Rotation takes place at a constant angular velocity, ω, in rad s^{-1} around the axis with the disc being centered on the axis perpendicular to the plane disc surface. As the electrode rotates the angular velocity is equal to $2\pi f$, where f is the rotation rate in revolutions per second. The result of this motion is that solution adjacent to the electrode is expelled outwards away from the axis of rotation by the centrifugal force. The expelled solution is replaced by flow normal to the electrode surface. Hence the rotating disc acts as a pump which moves solution from the bulk to the centre of the electrode and then across the surface of the electrode as shown in Fig 2.1. [67]. Provided the Reynolds number is not exceeded, laminar flow will occur and the mass transport of solution species may be provided. The Reynolds number for the RDE electrode used in this work was calculated to be 4720. This indicates that the maximum rotation rate achievable, for this electrode system, is 22222 rpm while still maintaining laminar flow conditions.

When using a RDE, material is transported to the electrode surface by a combination of diffusion and forced convection. The current response may be predicted according to Fick's first law and expressed in terms of the Nernst diffusion layer concept [66].

$$|i| = \frac{nFD(c_b - c_s)}{\delta} \tag{2.1}$$

where i is the current density, n is the number of electrons transferred in the reaction, F is the Faraday constant, D is the diffusion coefficient of the electroactive species, c_b and c_s are the bulk and surface concentrations of the electroactive species respectively, and δ is the thickness of the Nernst diffusion layer. In this thesis the convention adopted that is for a reduction reaction the sign of the current density is negative and positive for an oxidation reaction.

A limiting current, i_L, is reached when the surface concentration of the electroactive species becomes effectively zero. Therefore substitution of $c_s = 0$ into Eq. 2.1 provides the relationship for the limiting current

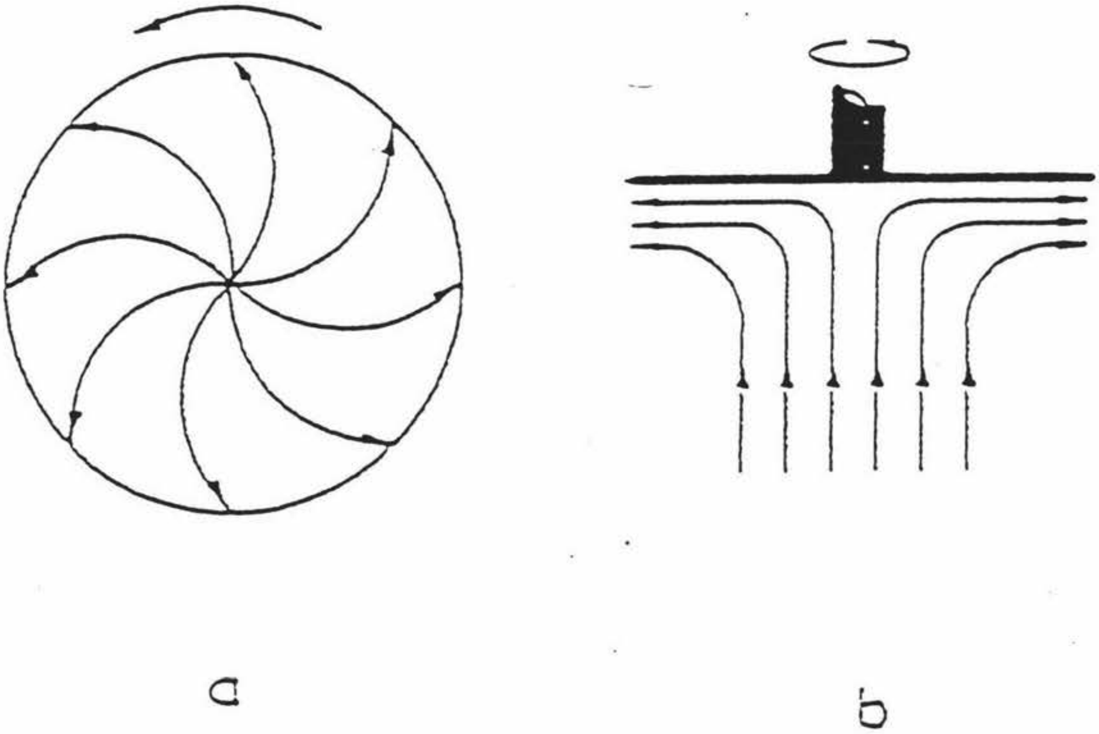

Fig 2.1 The flow patterns created by the RDE, (a) solution flow close to the electrode surface, view from below and (b) view from side showing the pumped solution towards and outwards the disc.

$$i_L = \frac{nFDc_b}{\delta} \tag{2.2}$$

This is qualitatively correct but does not take into account the hydrodynamics of the process, the rotation rate. Under laminar flow conditions and in a liquid medium of kinematic viscosity ν, the thickness of the diffusion layer decreases with increasing electrode angular velocity [68,69] according to the quantitative treatment described by Levich.

$$\delta = 1.61\, D^{1/3}\omega^{-1/2}\nu^{-1/6} \tag{2.3}$$

The combination of both Eq. 2.2 and Eq. 2.3 gives the Levich equation, for the hydrodynamic process at RDEs under mass-transport conditions.

$$i_L = 0.620\, nFD^{2/3}\omega^{1/2}\nu^{-1/6}c_b \tag{2.4}$$

Accordingly under mass-transport the limiting current should be proportional to the square root of the angular velocity [65].

The rotating disc electrode provides an efficient means for establishing reproducible mass transport and therefore analytical measurements may be made with high sensitivity and precision. If the steady state limiting current is controlled purely by diffusional mass transport, a plot of i_L *vs* $\omega^{1/2}$ as a function of c_b should be linear and pass through the origin. If this is the case, then the diffusion coefficient of the electroactive species may be then evaluated from the slope of the linear plot according to Eq. 2.4. Consequently, rotation rates of 630, 1000, 1585, 2500, 4000, 6300, and 10000 rpm were selected, so as to be evenly spread on an $\omega^{1/2}$ axis. Koutecky Levich influence here, i.e. a mix or electron kinetics and mass-transport.

2.5.1 *Turbulent and laminar flow*

In order to correctly interpret the effects of the rotating disc electrode it is important to appreciate the flow patterns likely to operate over the rotation rate range used in this work.

Turbulent flow, in which liquid motion has no regular pattern, occurs in the bulk of the solution away from the electrode. Turbulent mass-transfer relations concerning forced convection are of interest because of their practical importance, since turbulence promotes an increase of transfer rates. Consequently, deliberate turbulent flow is frequently used in electroplating and electroanalytical applications. However, for kinetic studies such as the present case, laminar flow is essential to interpret the electrode kinetics. When the concentration profile is fully developed, the mass transfer rate becomes independent of the transfer length. The point at which the transition to turbulent flow from laminar flow is predicted by a dimensionless number called the Reynolds number, Re, which is defined by,

$$Re = \frac{vl}{\nu} \tag{2.5}$$

Where v is the characteristic velocity of the electrode, l is the characteristic length of the electrode, and ν is the kinematic viscosity.

The characteristic velocity and length are different for each system, so that the critical Reynolds number where flow becomes turbulent from laminar must be evaluated for each electrode. The characteristic velocity is the linear velocity at the outer edge of the RDE, given by

$$v = \omega r \tag{2.6}$$

The characteristic length is the radius of the electrode, r, and the critical Reynolds number is about 1×10^5 [70]. The condition for laminar flow in RDE is thus given by equation 2.7

$$\frac{(\omega r)r}{\nu} = \frac{\omega r^2}{\nu} < 1 \times 10^5 \tag{2.7}$$

The critical *Re* number represents the upper limit for laminar flow over ideal smooth planar surfaces. Consequently, perpendicular to the axis of rotation if the surface is rough, or not perpendicular to the axis of rotation, then turbulent flow may occur at lower Re numbers.

Equation 2.7 may be rearranged to give the maximum rotation rate before turbulent flow is likely to occur

$$\omega < \frac{\nu \times 10^5}{r^2} \tag{2.8}$$

In the present study ν is likely to be close to that for pure water at the maximum ω obtainable on the RDE.

The lower limit for rotation is determined by the need for the limiting current density resulting from rotation be large compared to that which would occur in a static, non-stirred solution due to natural convection. The practical lower limit with the use of the RDE-1 is much lower than the lower limit of rotation in this study, which is 630 rpm. Practically as long as the value for ω was greater than 100 rpm you would still be in the rotation limits to predict laminar flow.

In laminar flow, layers of the liquid slide by one another in a parallel direction to the electrode surface. When using a rotating disc electrode there is a uniform axial velocity toward the disc that depends on the axial distance from the disc only, and consistent with this, the mass-transfer rate is also uniform. A maximum value for the mass-transfer rate occurs at the leading edge of the electrode when the flow is parallel to the electrode. The parallel velocity component in the mass-transfer boundary layer is practically a linear function of the distance to the electrode. This is the flow system that is assumed to be operating in the present work. The minimum rotation rate was selected to be 630 rpm and the maximum 10000 rpm. Both well within the upper and lower boundaries of laminar flow.

2.5.2 *Calibration of Rotation Rate*

The RDE rotation rate was calibrated to ensure correct performance. The calibration procedure was carried out independently using an optical digital tachometer (Extech Instrument, Taiwan) by attachment of a reflective strip to the body of the RDE WE.

The rotation speed on the RDE-1 device was set using the RDE-adjust control over the range of the rotation rate used throughout this work and these were compared to the results given by the optical tachometer. A typical set of readings for these rotation rates is reported in Table 2.1. It can be seen that there was good agreement between the RDE-1 setting and the results that the optical tachometer reported.

2.6 Reagents

All chemicals used in the preparation for this work were of highest available purity and all the electrolyte solutions were prepared in Millipore filtered water (Nanopure II, Barnstead, Newton, Massachusetts, USA).

2.6.1 *Mercuric Nitrate*

All mercuric nitrate solutions were prepared from Mercury (II) nitrate-1-hydrate (Riedel-De Haen, Germany) in 1.00 mol L^{-1} Potassium nitrate (Riedel-De Haen, Germany) and 0.30 mol L^{-1} Nitric Acid (BDH, AnalaR, 69%).

2.6.2 *Mercuric Acetate*

All mercuric acetate solutions were prepared from red mercuric oxide (HgO, Unilab, Germany) in 0.20 mol L^{-1} acetate buffer at pH 5.0. The acetate content in these solutions was prepared by a combination of acetic acid (BDH, AnalaR, Germany) and sodium acetate (R.P. Normapur$^{T.M.}$ AR) in a molar ratio of 34.6:65.4 respectively.

2.7 Determination of pH for Mercuric Acetate solutions

The pH of the mercuric acetate solutions were determined using a high impedance pH-meter (Model 50, Denver Instrument Company, USA) calibrated in advance with standard buffer solutions at the temperature of 20°C.

The pH-meter was fitted with a pH-Ag/AgCl (Denver Instrument Company, USA) combination glass membrane electrode, where the reference electrode compartment was filled with 4 M KCl saturated with AgCl.

Standard buffers of pH 4.0, 5.0, and 6.0 were prepared [71] to enable accurate determination of the desired pH 5.0 of the electrolytes.

Table 2.2 shows the composition of standard buffer solutions over pH range 4.0 to 6.0.

Electrode Rotation Rate / rpm	
RDE-1 RPM Adjust	Optical Tachometer
630	629.6
1000	1000
1585	1585
2500	2500
4000	4000
6300	6300
10000	10000

Table 2.1 Rotation rate calibration for the RDE. The data in the first column represents the rotation rates set on the front panel of the RDE-1 whilst the second column lists the rotation rates detected independently by an Optical Tachometer.

pH	Composition of Standard Buffer Solutions
4.0	50 ml of 0.1 M ($KHC_8H_4O_4$) + 0.1 ml of 0.1 M (HCl).
5.0	50 ml of 0.1 M ($KHC_8H_4O_4$) + 22.6 ml of 0.1 ($NaOH$).
6.0	50 ml of 0.1 M (KH_2PO_4) + 0.1 ml of 0.1 M ($NaOH$).

Table 2.2 The composition of standard buffer solutions [71] over the pH range 4.0 to 6.0.

2.8 Deoxygenation of electrolyte

At room temperature and under normal atmospheric conditions oxygen can be present at up to 10^{-3} M [72]. This dissolved oxygen may undergo reduction in acidic media according to

$$O_2 + 2H^+ + 2e^- \rightarrow H_2O_2 \qquad (2.9)$$

$$H_2O_2 + 2H^+ + 2e^- \rightarrow 2H_2O \qquad (2.10)$$

And in neutral or basic media as

$$O_2 + 2H_2O + 2e^- \rightarrow H_2O_2 + 2OH^- \qquad (2.11)$$

$$H_2O_2 + 2e^- \rightarrow 2OH^- \qquad (2.12)$$

In most of this work the electroanalysis was performed at some point in the negative region where these reactions may occur. This would result in, at the very least, an increase in the background current.

Consequently, all electrochemical measurements were carried out in solutions that had been deoxygenated by purging through a bubblier with oxygen-free nitrogen gas for 15 minutes prior to the commencement of experiments and also throughout experiments.

CHAPTER 3

Cyclic Voltammetry Studies

3.1 Introduction

This chapter is divided into two sections. The first part focuses on an overview of the cyclic voltammetry methodologies used to study the electrodeposition of mercury on GC electrodes. The second part of this chapter details the observations for each of the experimental sections which focus on different aspects of this cyclic voltammetry work: concentration dependence of RDE; scan rate dependence of RDE; rotation rate dependence of RDE; coulometry study; microelectrode studies, and a electrochemical cleaning study. The main focus of this chapter is the work carried out in the acetate buffers, the observations of some nitrate results will be discussed but they are present for a reason of comparison for the acetate observations, rather than a detailed study of there own. Interpretation of the detailed observations will be discussed in Chapter 5.

3.2 Cyclic Voltammetry

Cyclic voltammetry (CV) is a potential-controlled technique where a triangular-wave potential is applied to the cell so that the WE potential is swept linearly and continuously between two potential limits. The number of cycles may be varied from one to a large number to investigate long term changes in electrochemical behavior. The observed faradaic current is dependent on the kinetics and transportation of the electroactive species to the electrode and is reported as a function of applied potential. The resulting plot of i *vs* E is termed a voltammogram. Important parameters for a CV are the initial potential, the initial sweep direction, scan rate, the maximum potential, the minimum potential, and the final potential [67].

The primary use of CV is as a diagnostic tool that provides information about electrochemical processes under various conditions. While CV is not used for routine quantitative analyses, it has become an important tool for the study of mechanisms and rates of oxidation/reduction processes.

The convection adopted in this thesis is that defined in the Bioanalytical Systems Inc. BAS 100 B/W software, positive currents denote net reduction processes and negative currents denote net oxidation processes. Cyclic voltammograms of *i vs* E are plotted with increasingly more negative potentials to the right side of the x-axis with increasingly positive currents up the y-axis. Consequently, the reduction processes of interest in this thesis are located to the top right corner of the voltammograms. All CVs commence and terminate at the upper potential limit in the oxidation region unless otherwise stated. The statement forward sweep refers to scanning to more negative potentials.

3.3 Features of mercury deposition voltammagrams in acetate media

Features of the voltammagrams that will be identified and referred to in this study of the electrodeposition of mercury on GC electrodes are described in this section.

3.3.1 *Peaks C1 and C2*

A typical voltammogram of a numerously cycled GC RDE involving the deposition and removal of mercury, by cyclic voltammetry, is shown in Fig 3.1. Features to be noted in Fig 3.1 are the two peaks in the cathodic region labeled C1 and C2. These peaks form and increase in size as the GC RDE is cycled without intervening cleaning, either mechanical or electrochemical. After peak C2 and on the return cycle a constant, or steady state, current is maintained until the commencement of oxidation.

3.3.2 *Reduction overpotential*

From the first cycle on a fresh mechanically-cleaned electrode to the second cycle, at mercury concentrations of 5.0 mM and higher on GC RDEs, there is a clearly describable change in the potential where the onset of reduction occurs, E_{red}. In this work this change will be referred to as the shift in the reduction overpotential. Fig 3.2 shows this shift for a 10.0 mM Hg^{2+} solution occurring between the first and second cycles, where the onset of reduction for the mechanically-cleaned first cycle occurs at +105 mV, whilst on the second cycle, which commenced immediately after the first with no intervening cleaning, the onset of reduction shifts to +380 mV. C1 and C2 are not evident on the first cycle but are distinguishable on the second cycle.

3.3.3 *Peak A2*

When the concentration of Hg^{2+} is lower than 2.0 mM, a second peak in the anodic region can be seen, this peak is never observed in concentrations of 2 mM and higher, or on freshly mechanically-polished electrodes. In Fig 3.3 this peak can be seen and is labeled as A2.

3.3.4 *Current spikes*

Figure 3.4 illustrates the feature that occurs at Hg^{2+} concentrations 10.0 mM or higher. On multiple cycled electrodes at the cathodic extreme of the cycle (−800 to −1000 mV) seemingly random cathodic current spikes occur. These spikes increase in frequency and size as the electrode surface gradually ages and also with increased rotation or scan rates.

All of these features are only observed when the supporting electrolyte used is the acetate buffer.

3.4 Coulometry

Coulometric analysis is based on the use of Faraday's laws of electrolysis, where the charge passed through the electrolysis cell is determined.

$$Q = n_{\mathrm{Hg}} nF \tag{3.1}$$

Q, the charge, is measured and if n, the number of electrons transferred, is known, then n_{Hg}, the moles of species, can be determined.

The means for obtaining the coulometric results for this work was the coulometric option within the BAS 100/W software (Bioanalytical System Inc., West Lafayette, Indiana, USA). Positive changes in Q relate to an increase in the rate of reduction.

Fig 3.5 shows a typical voltammogram of a 5.0 mM Hg^{2+} solution in 0.20 M acetate and 1.00 M NaOAc at pH 5.0. Under these conditions C1 and C2 are present. Fig 3.6 shows the corresponding coulometric plot produced by the BAS software. The point where reduction commences in Fig 3.5 can be seen in Fig 3.6 as where an increase in the charge occurs. The slight negative charge, accumulated to this point, predominates due to non-faradaic processes and is labeled Q_{rc}. The charge increases from Q_{rc} linearly until −1000 mV and

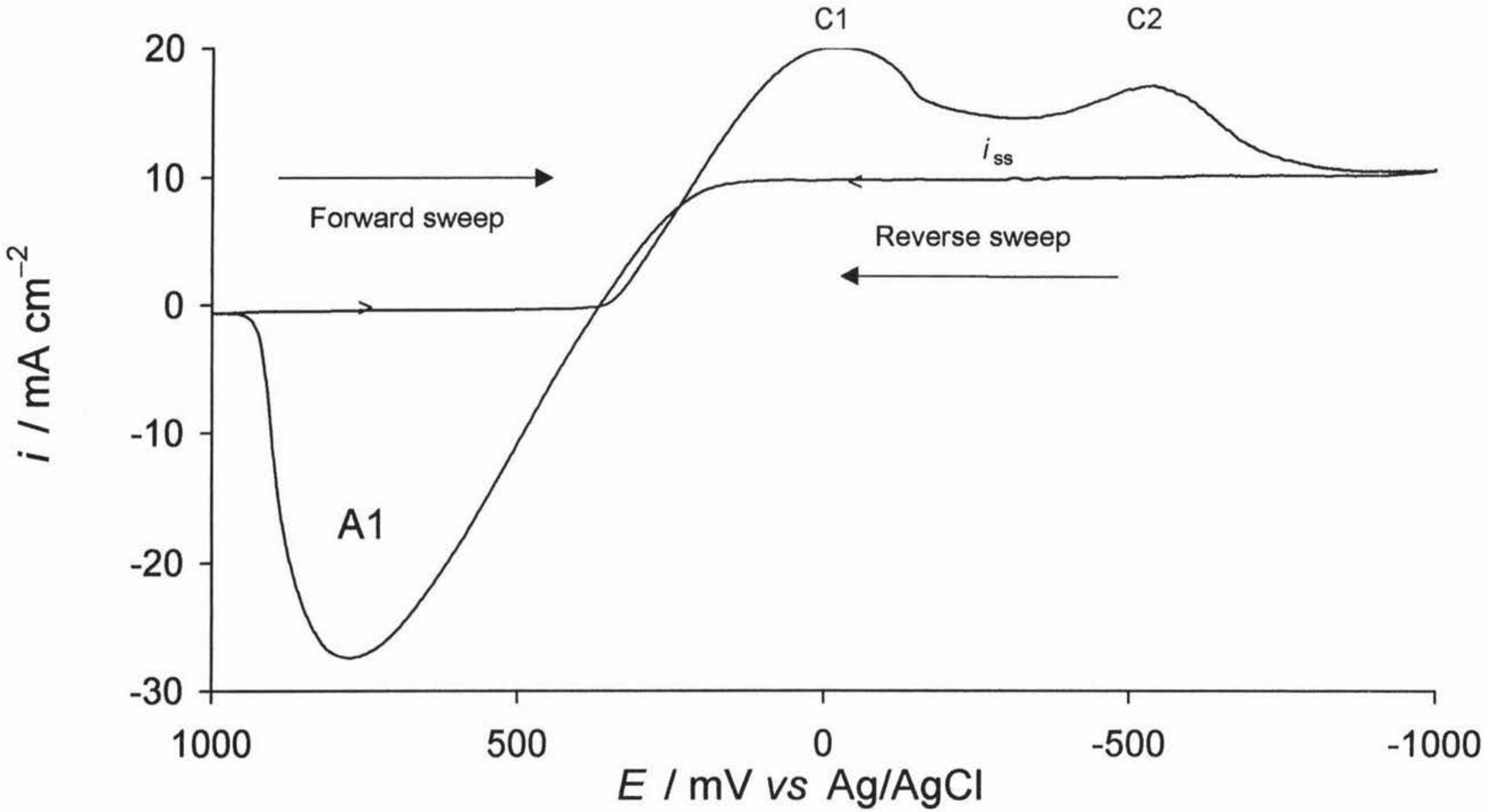

Fig 3.1 A voltammogram displaying peaks C1, C2, and A1, and the steady state current, i_{ss}. The directions for the forward and reverse sweeps are also indicated.

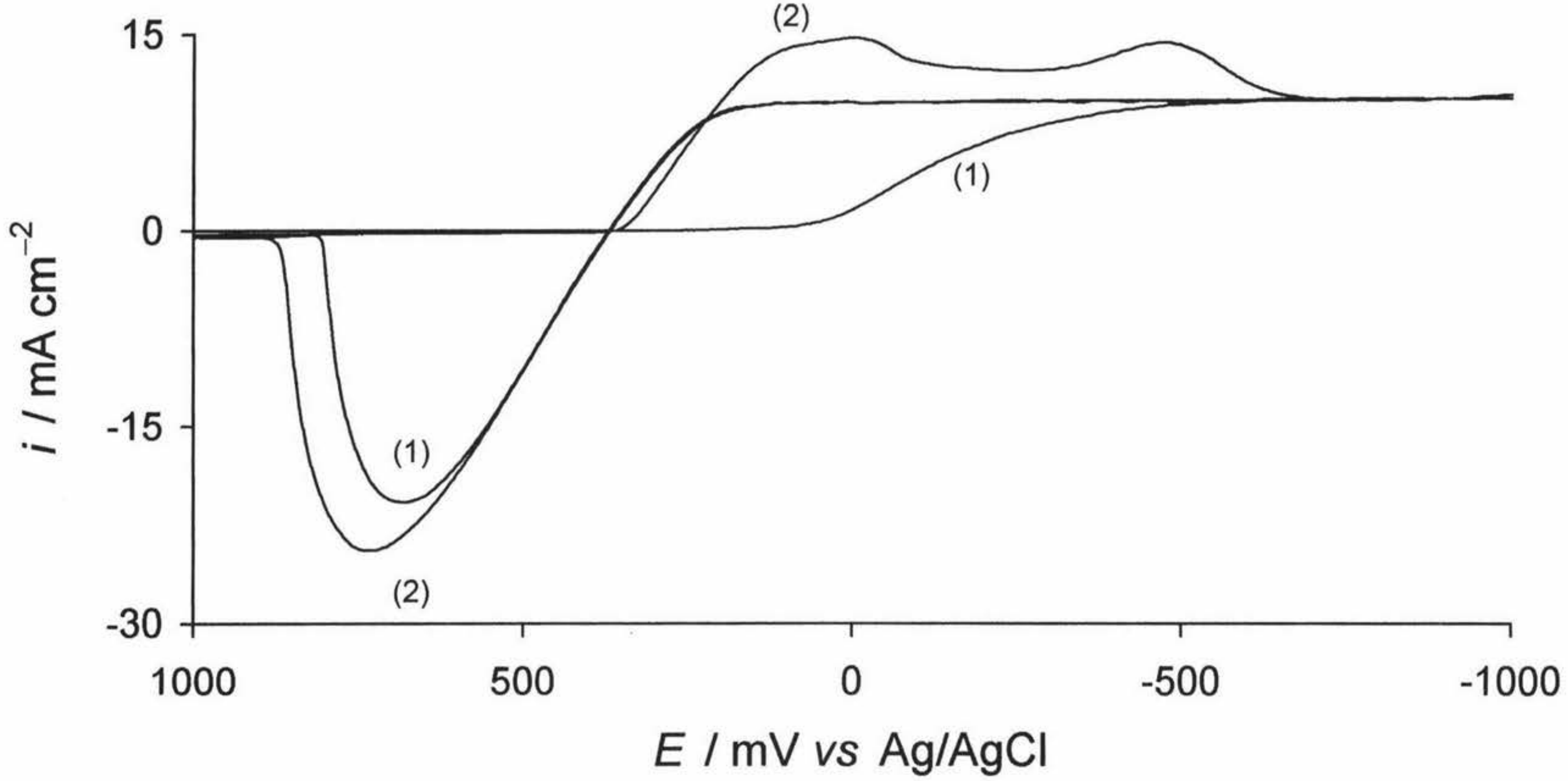

Fig 3.2 Two voltammograms displaying the shift in overpotential for the onset of reduction, E_{red}. (1) a mechanically-cleaned electrode, E_{red} value of +103 mV, and (2) an electrode been cycled seven times without cleaning, E_{red} value of +380 mV. ν = 100 mV s^{-1}, $[Hg^{2+}]$ = 10.0 mM.

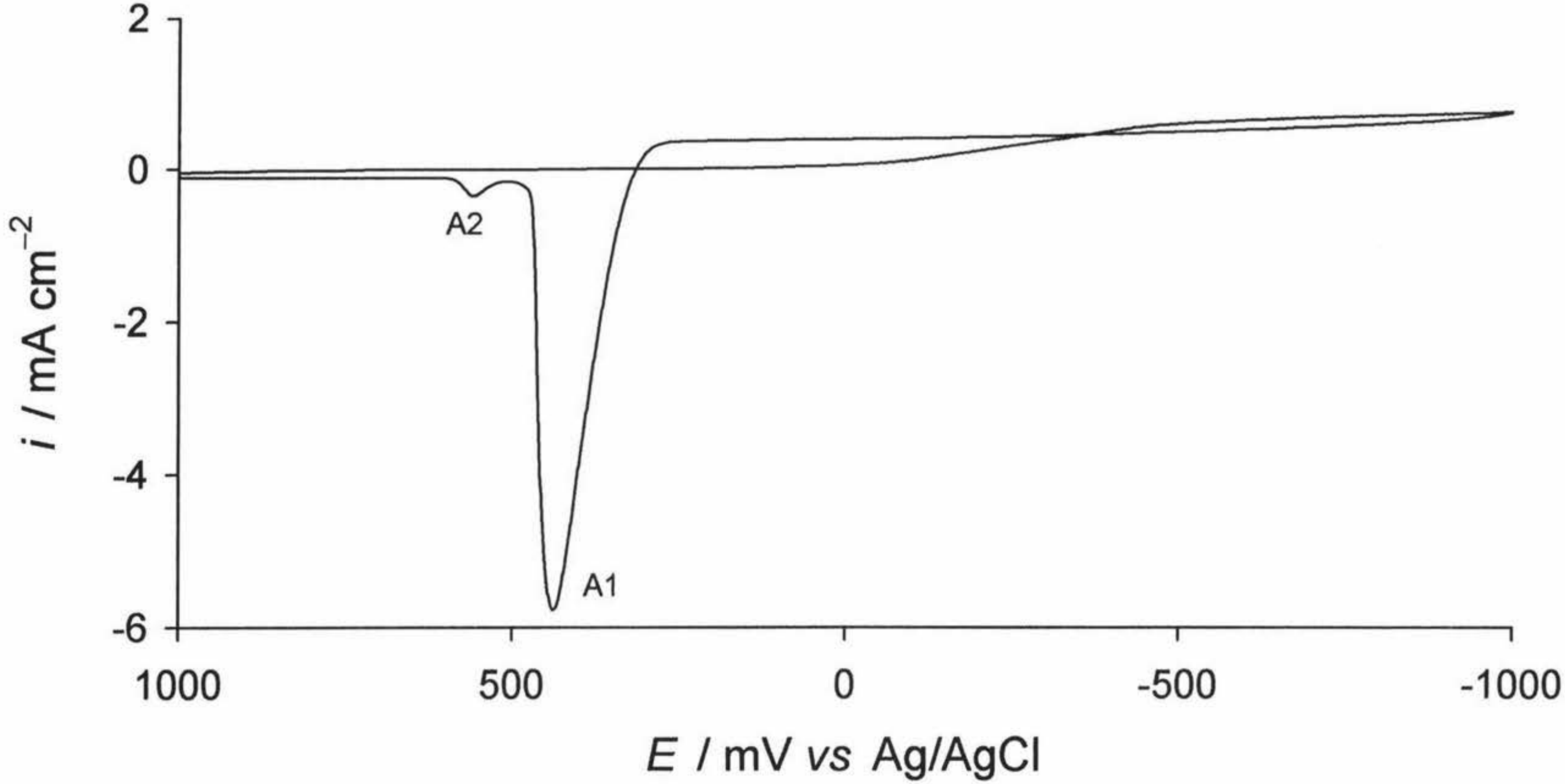

Fig 3.3 A voltammogram displaying A2. $v = 100$ mV s^{-1}, [Hg^{2+}] = 2.0 mM.

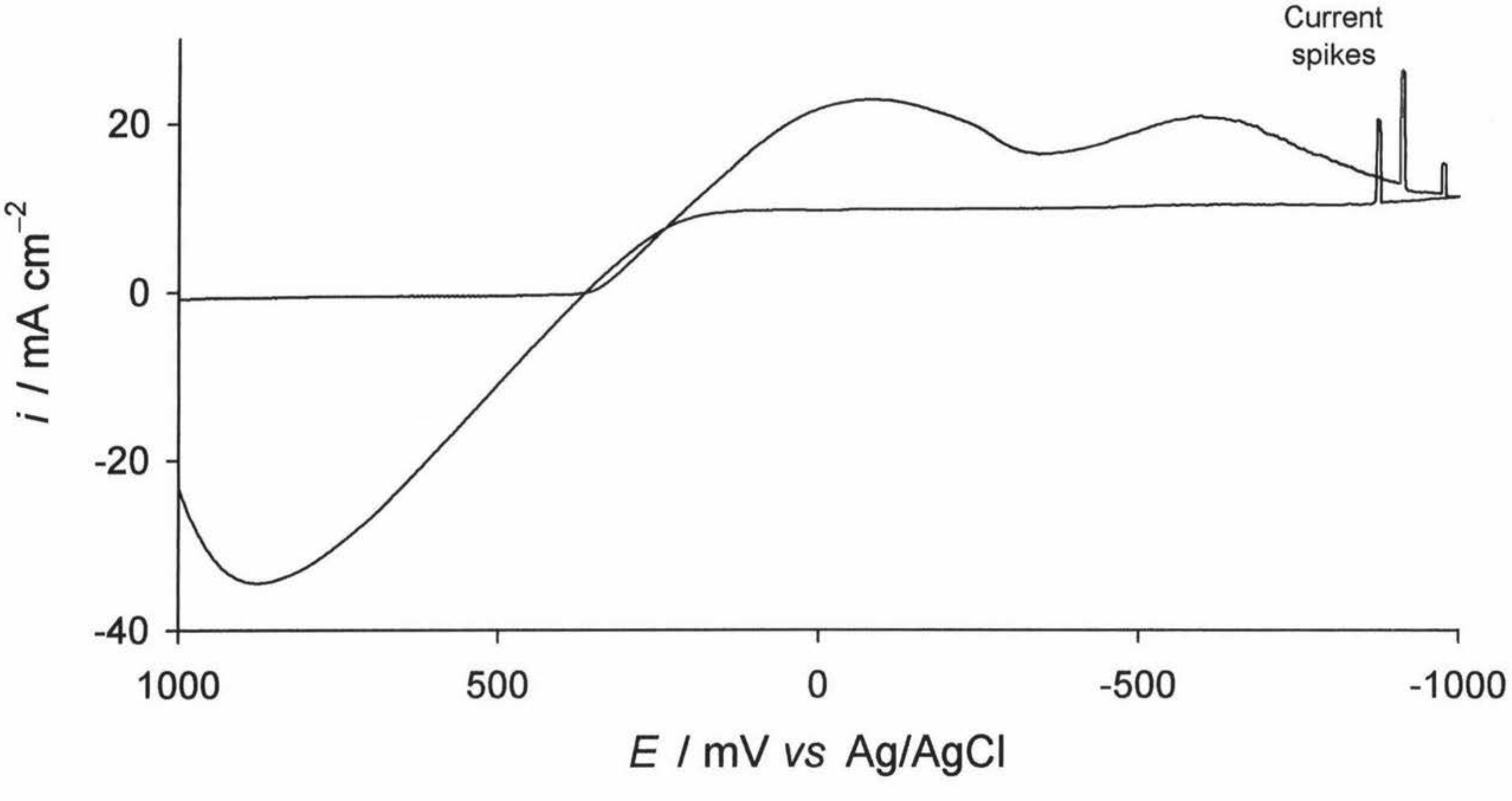

Fig 3.4 A voltammogram displaying cathodic current spikes. $\nu = 100$ mV s^{-1}, [Hg^{2+}] = 10.0 mM.

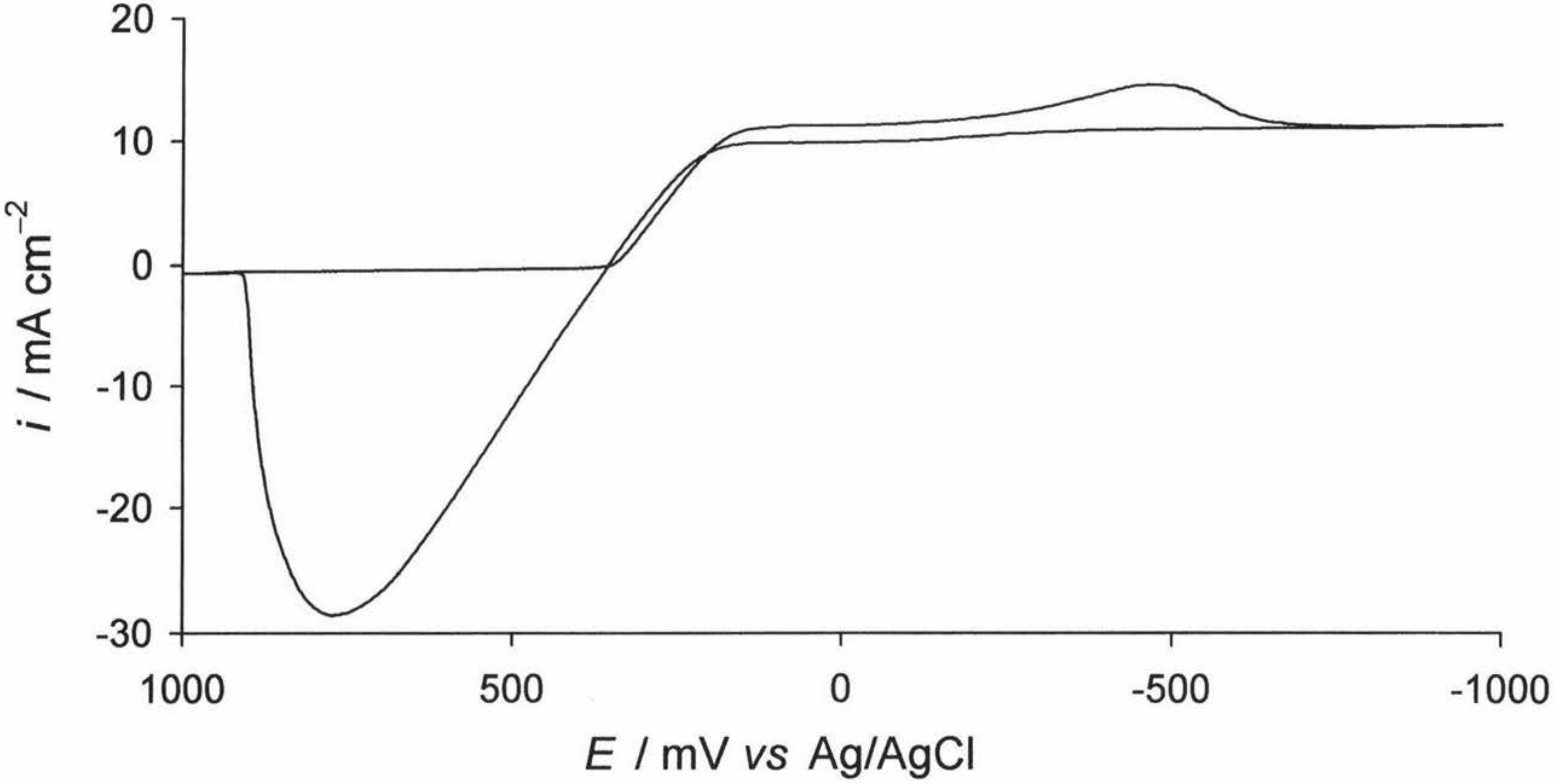

Fig 3.5 A voltammogram where C1 and C2 have formed. $\nu = 100$ mV s^{-1}, [Hg^{2+}] = 5.0 mM

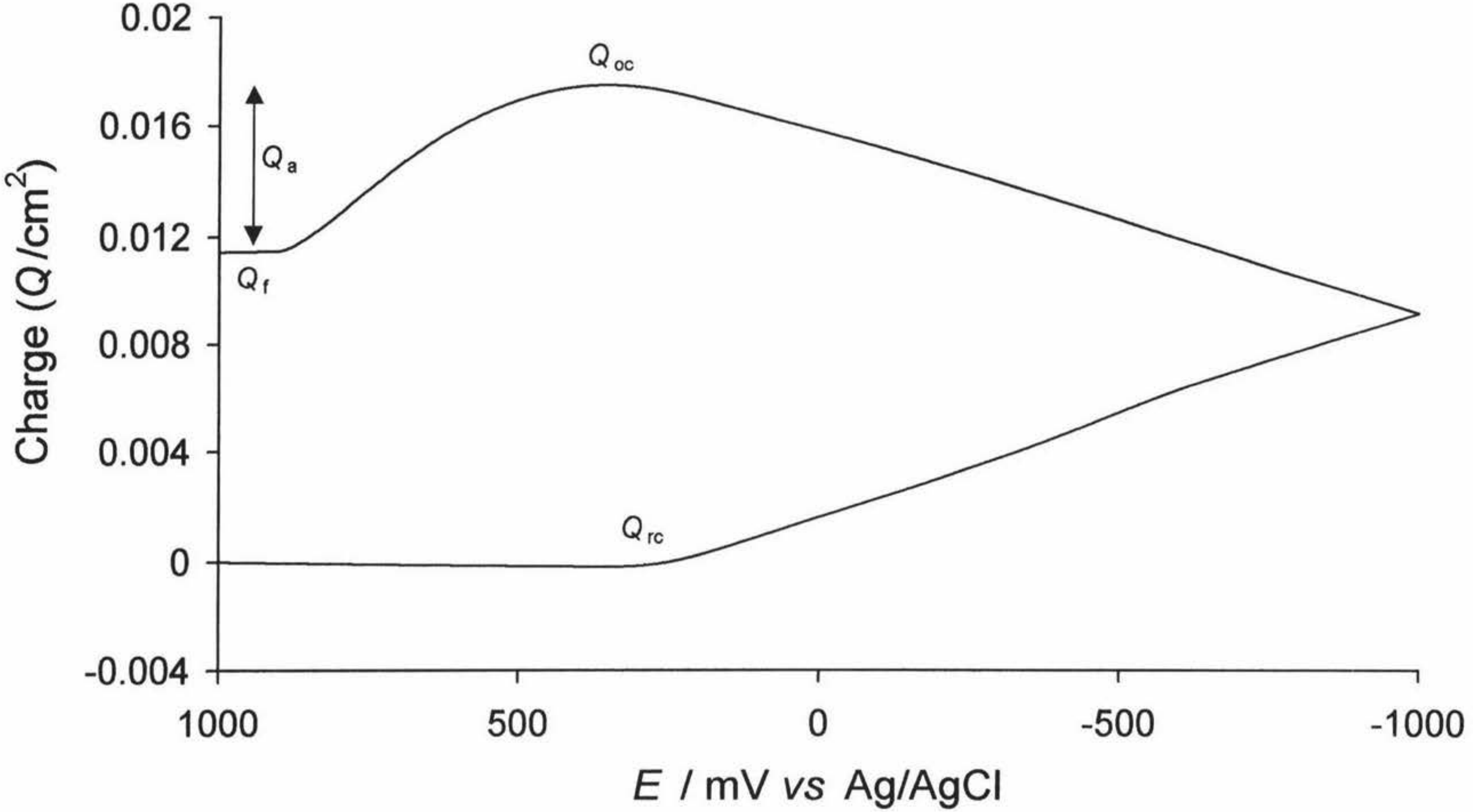

Fig 3.6 A coulometric plot resulting from Fig 3.5. Q_{rc} representing the accumulated charge due to non-faradaic processes, Q_{oc} representing the point where oxidation of mercury commences, and Q_A is the difference between Q_{or} and Q_f, which is the final charge value.

continues to increase linearly on the reverse sweep. The point where the charge starts to decrease is the point at which oxidation of electrodeposited Hg commences as the charge is labeled Q_{oc}. The total cathodic charge is given by

$$Q_c = Q_{oc} - Q_{rc} \tag{3.2}$$

The difference between Q_{oc} and the charge at the end of the cycle is identified as the total anodic charge, Q_a. This coulometric analysis shows that the total charge gained in the reduction of mercury is not all recovered through the oxidation reaction. One interpretation is that some Hg^0 remains on the surface of the electrode at the anodic vertex of the cyclic voltammogram.

3.5 Concentration Dependence

Examination of voltammograms for a range of Hg^{2+} concentrations in acetate buffers reveals a number of interesting features. The concentration of Hg^{2+} alters the height and position of peaks C1 and C2, the shift in the overpotential for the onset of reduction, and the development of new features in addition to those identified in section 3.3.

As the concentration of Hg^{2+} is increased from 0.5 to 10.0 mM there is an increase in the steady state current, i_{ss} as shown in Figs 3.7 and 3.8. With this increase, the oxidation peak, A1, also exhibits an increase in its size and amplitude.

At the lower concentrations of 0.5 and 1.0 mM Hg^{2+} shown in Fig 3.8 the occurrence of a previously unidentified peak, A2, on the reverse sweep becomes evident. This peak was never observed at higher concentrations, as it is likely to have been covered by the A1 current peak for those higher concentrations. Until the concentration was sufficiently low for the dominating A1 peak to decrease in size this small A2 peak would have been masked in the voltammogram. In Fig 3.8 this A2 peak can be seen in the voltammograms for both 0.5 and 1.0 mM Hg^{2+}. It is not observed in the voltammogram for 2.0 mM, but it is clearly evident that the A1 peak for this cycle covers the potential region where A2 is observed at the lower concentrations. Another feature of the lower concentrations is the absence of a shift in the onset of reduction potential, E_{red}, with cycling for the 0.5 and 1.0 mM solutions. The cycles in Fig 3.7 are the seventh cycles of an electrode previously mechanically cleaned. Here E_{red} remains the same value as that for the first cycle after mechanical-cleaning. In contrast E_{red} for the 2 mM Hg^{2+} solution exhibited a shift from that of the first cycle after mechanical-cleaning but not to the same extent as that for concentrations higher than 2 mM. The shift in E_{red} is immediate in concentrations above 2 mM, which means that after the first mechanically cleaned cycle, on the second cycle, E_{red} makes a large anodic shift. Table 3.1 shows E_{red} values for each of the concentrations from the first mechanically cleaned cycle to the eighth cycle of the electrode. Table 3.1 shows that E_{red} for 2.0 mM increased from –4 mV to 191 mV over eight cycles but does not exceed this potential, which is some 150 mV of the final E_{red} for 5.0 and 10.0 mM, no matter how many times the electrode is cycled without intervening mechanical-cleaning. The 0.5 and 1.0 mM solutions show some fluctuation in E_{red} but this is deemed insignificant. The E_{red} for 1.0 mM is +54 mV and for 0.5 mM it is –32 mV.

The lower concentration of 0.5, 1.0, and 2.0 mM do not exhibit the peaks C1 and C2, even after the eighth cycle. In Fig 3.8 a number of features can be seen. The absence of C1 and C2 in the 2 mM cycle can be seen more clearly when shown on the same scale as the 5.0 and 10.0 mM voltammograms. In the 5.0 mM voltammogram the formation of both C1 and C2 is complete and the steady state current, i_{ss}, established by the end of the forward sweep. For the 10.0 mM cycle the formation of C1 is completed on the forward sweep but C2 is not completed until ca. –800 mV on the reverse sweep after which the steady state is established.

The 10.0 mM concentration also exhibits current spikes predominately from –700 to –1000 and back to –700 mV. A representative voltammogram for 10.0 mM Hg^{2+} is shown in Fig 3.7 with six such spikes in this potential region. In contrast to the lower concentration, the A1 peak for 10.0 mM Hg^{2+} is not completed by the end of the reverse sweep.

3.6 Scan Rate Dependence

The scan rate dependence experiments on the GC RDE were performed with a fixed rotation rate of 1000 rpm and an electrochemical-cleaning cycle was executed between each cycle at 900 mV for 5 seconds using the BAS 100/W 'cleaning' software option (Bioanalytical System Inc., West Lafayette, Indiana, USA). The experiments were

Cycle number	0.5 (mM)	1.0 (mM)	2.0 (mM)	5.0 (mM)	10.0 (mM)
1	−60	−12	−4	5	190
2	45	119	191	168	353
3	−21	79	191	345	353
4	−32	73	191	345	353
5	−32	57	191	345	353
6	−32	56	191	345	353
7	−32	54	191	345	353
8	−32	54	191	345	353

Table 3.1 E_{red} as a function of [Hg^{2+}] with varying numbers of cycles from that of a mechanically-cleaned RDE. (mV vs Ag/AgCl)

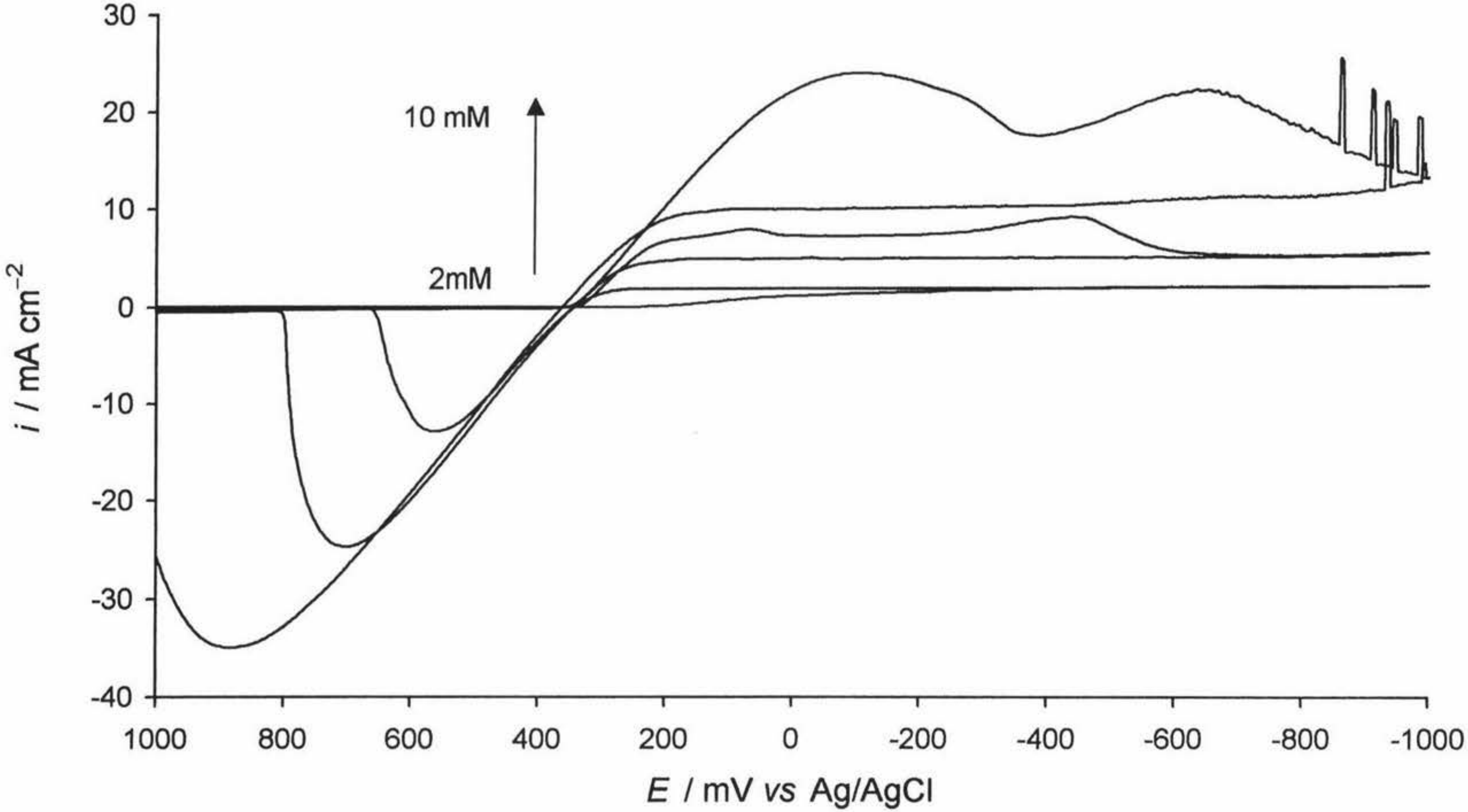

Fig 3.7 A series of voltammograms with varying [Hg^{2+}] of 2.0, 5.0, and 10.0 mM. $\nu = 100$ mV s^{-1}, $\omega = 1000$ rpm.

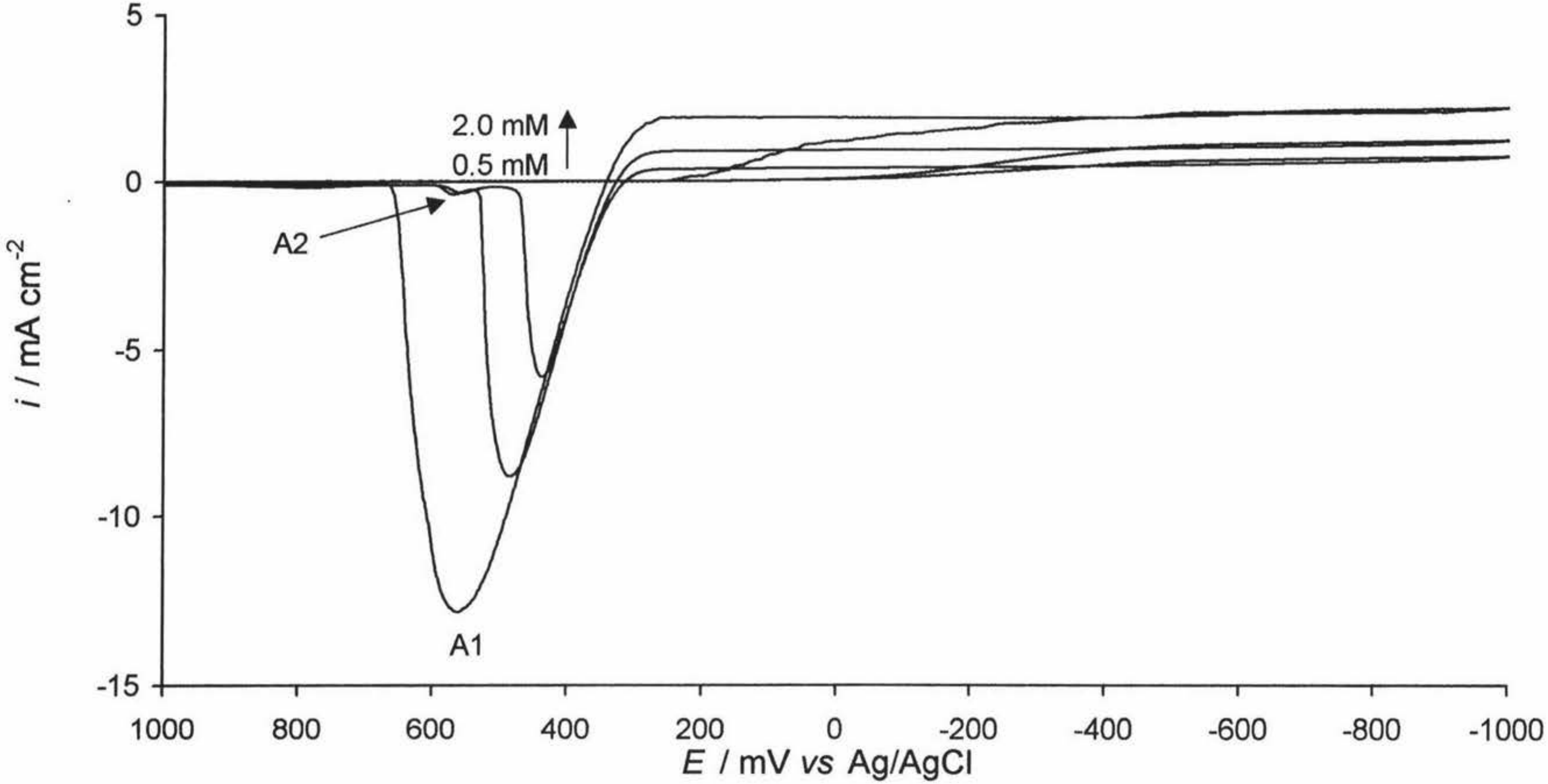

Fig 3.8 A series of voltammograms with varying [Hg^{2+}] of 0.5, 1.0, and 2.0 mM. ν = 100 mV s^{-1}, ω = 1000 rpm.

performed over the 20 mV s^{-1} to 1000 mV s^{-1} scan rate range and collected in groups according to concentration.

Fig 3.9 shows the scan rate dependence for the highest concentration of 10.0 mM Hg^{2+}. The oxidation peak, A1, only reached completion on the reverse sweep for the lowest two scan rates of 20 and 50 mV s^{-1}. The cathodic peak, C1, was observed at 20 mV s^{-1} but C2 was not. C1 and C2 were both observed for the 50 mV s^{-1}. C1 and C2 and both fully formed by the end of the forward sweep in the 50 mV s^{-1} voltammogram. No current spikes were observed for the lowest two scan rates of 20 and 50 mV s^{-1} but were present for the 100 and 200 mV s^{-1}. The 200 mV s^{-1} compared to the 100 mV s^{-1} voltammogram respectively had a greatly increased number of current spikes. Current spikes were not observed for 500 and 1000 mV s^{-1}. It is noted that this may be linked with the observation that the C2 peak at these high scan rates were nowhere near completion by the end of the forward sweep. Steady state currents were attained for all scan rates with the exception of the 500 and 1000 mV s^{-1}. Steady state currents for 100 and 200 mV s^{-1} were only reached on the reverse sweep. The anodic A1 peak was observed to increase with scan rate in all cases.

At 5.0 mM Hg^{2+} A1 peaks reached completion by the end of the reverse sweep, for 20, 50, and 100 mV s^{-1} as shown in Fig 3.10 compared to only 20 and 50 mV s^{-1} for the 10.0 mM Hg^{2+}. In a similar manner to 10.0 mM A1 increases with increasing scan rate. The 20 mV s^{-1} scan rate did not seem to exhibit the development of C1 or C2, it simply reached the steady state current. At 50 mV s^{-1} the formation of C1 and C2 was completed and a steady state current attained by the end of the forward sweep. Current spikes were observed on the scan rate cycles of 200, 500, and 1000 mV s^{-1} and all, had attained more than 50% of the C2 peak by the end of the forward sweep.

The 2.0 mM concentration exhibited a random effect for the location of E_{red}. There was no discernable evident for the onset of reduction at this concentration. However, it can be stated that reduction commences in the potential range of +250 and −100 mV, as shown in Fig 3.11. A steady state current is attained for all scan rates except for 500 and 1000 mV s^{-1} on the forward sweep. There are some indications that C1 could be forming at these high scan rates as well, although to a small extent and at an extremely negative potential of

–600 mV. A1 is completed for all scan rates but on the reverse sweep. There is some evidence of a shoulder at the anodic side of A1 suggestive of an overlap with A2. In contrast to 5.0 and 10.0 mM Hg^{2+}, at 2.0 mM A1 is found to decrease with increasing scan rate.

Figure 3.12 shows the scan rate dependence for a 1.0 mM Hg^{2+} solution. A steady state current is attained for all scan rates. The potential for the onset of reduction, E_{red}, unlike the 2.0 mM, adopts a constant value of 0 mV. Similar to 2.0 mM there is some evidence for C1 again at extremely negative potentials. A1 peaks are all completed by the end of the reverse cycle and similarly to the 2.0 mM these peaks again decrease with increasing scan rate. A2 peaks are now clearly discernable supporting the proposal that the shoulders in A1 at 2.0 mM were due to this peak. Fig 3.13 is an expansion of the A2 region in Fig 3.12. In Fig 3.13 it can be seen that A2 decreases in amplitude as the scan rate is increased, and the peaks also appear to be shifting to more anodic potentials with increasing scan rate. Above the scan rate of 100 mV s^{-1} the A2 peaks have broadened to the extent that it is difficult to determine where A1 finishes and A2 commences. In this graph it can also be seen that the current attained after both A1 and A2 have completed increases with increasing scan rate. This current may be due to the capacitance current in which case it would be expected to increase with increasing scan rate.

The multiple plot of the voltammograms for the scan rate dependence of 0.5 mM Hg^{2+} can be seen in Fig 3.14. Here it can be seen that similar to 1.0 mM Hg^{2+} C1 appears to commence forming at higher scan rates of extremely negative potential of –500 mV. All scan rates reach a steady state current during the reverse sweep. The potential at which the onset of oxidation occurs, E_{ox}, is shifting to more cathodic potentials with increasing scan rate. A1 is fully formed by the end of the reverse sweep and these peaks decrease with increasing scan rate. The A2 peak is present at all scan rates and is distinct from A1 unlike for the 1.0 mM solution. Fig 3.15 is an expansion of the A2 region of Fig 3.14. A2 clearly decreases with increasing scan rate, and shifts progressively to more anodic potentials. A new peak, A3, is seen for the first time at the lowest scan rate of 20 mV s^{-1}.

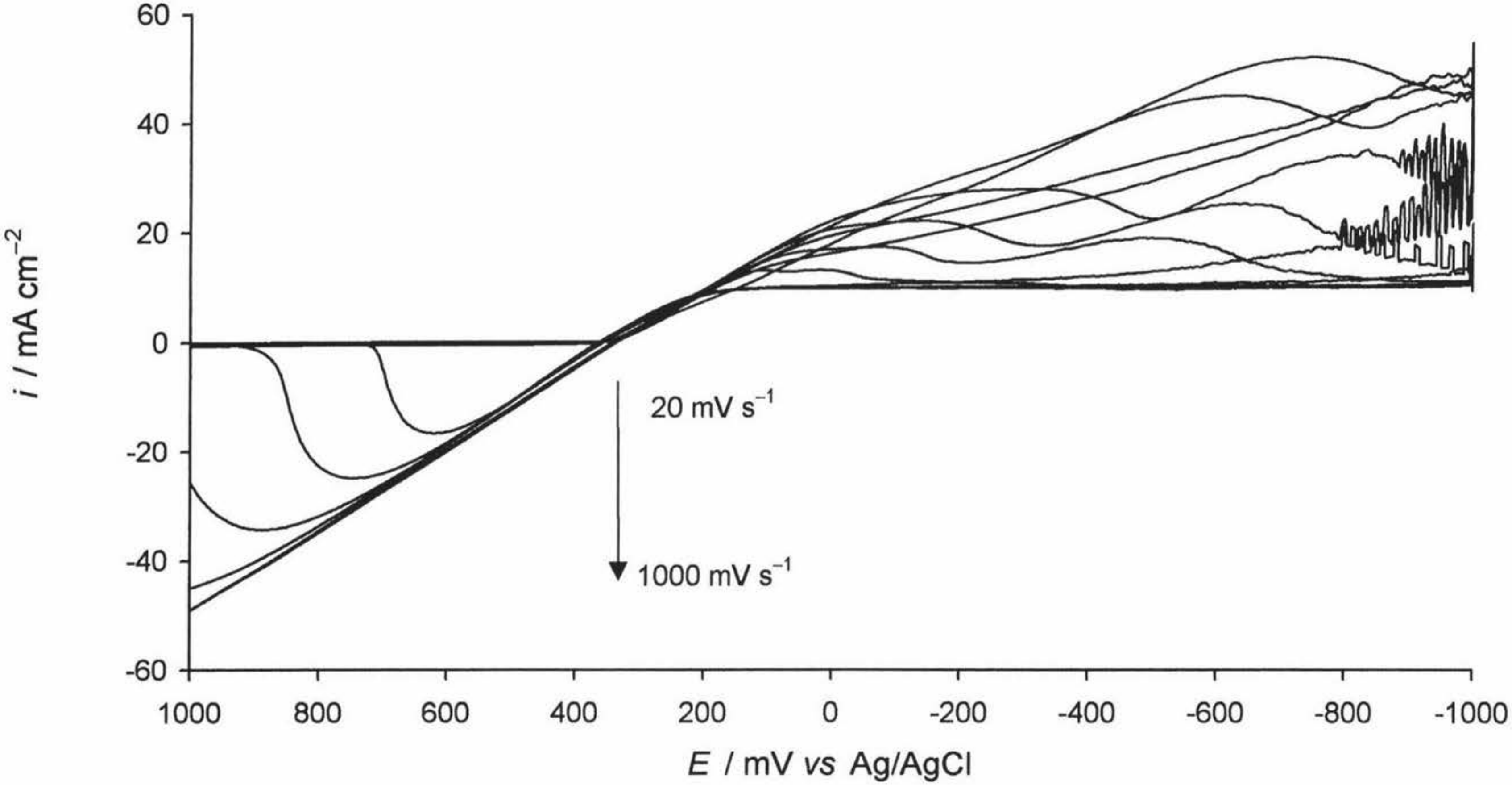

Fig 3.9 A series of voltammograms with varying *ν* of 20, 50, 100, 200, 500, and 1000 mV s^{-1}. $[Hg^{2+}]$ = 10.0 mM, ω = 1000 rpm.

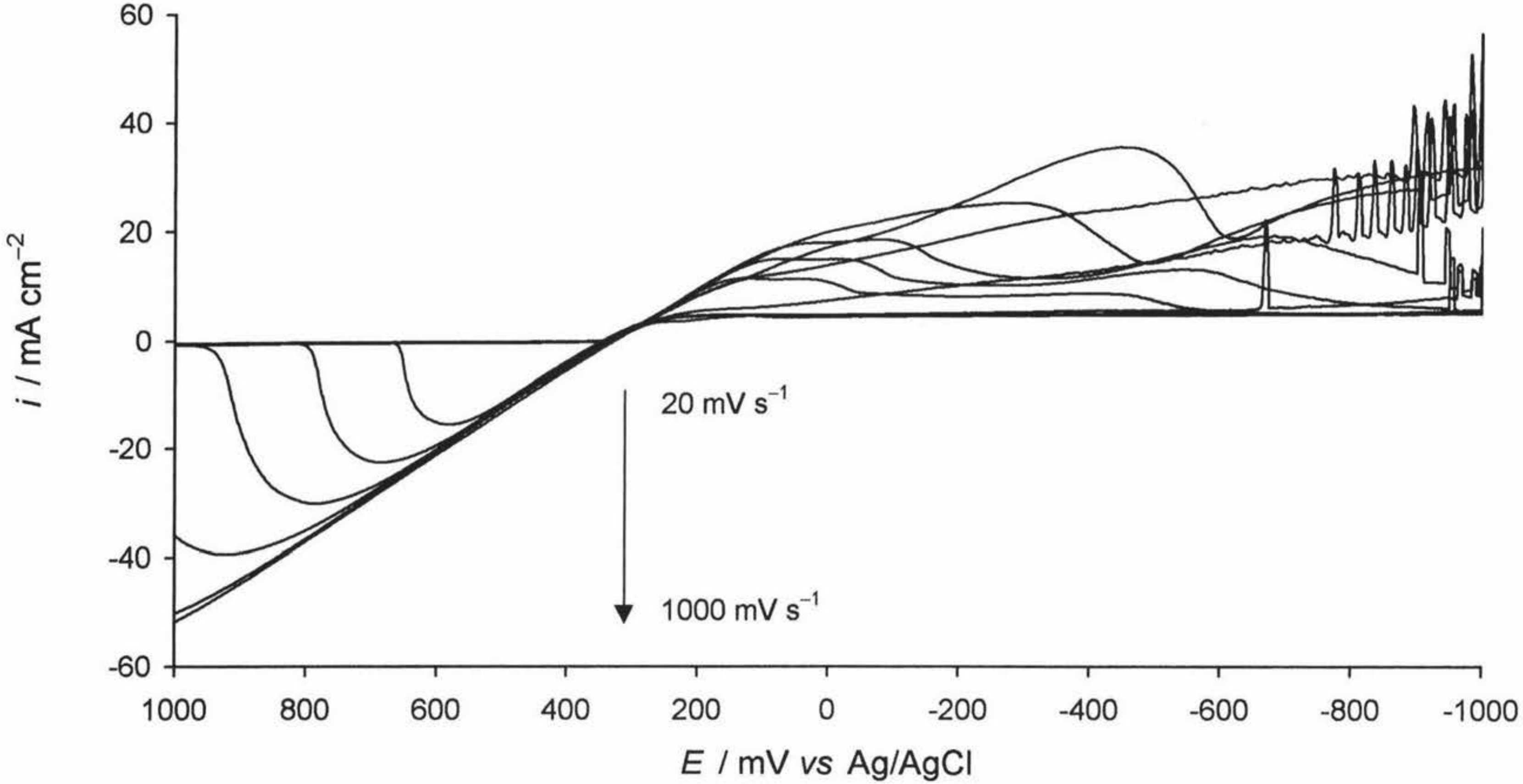

Fig 3.10 A series of voltammograms with varying v of 20, 50, 100, 200, 500, and 1000 mV s^{-1}. [Hg^{2+}] = 5.0 mM, ω = 1000 rpm.

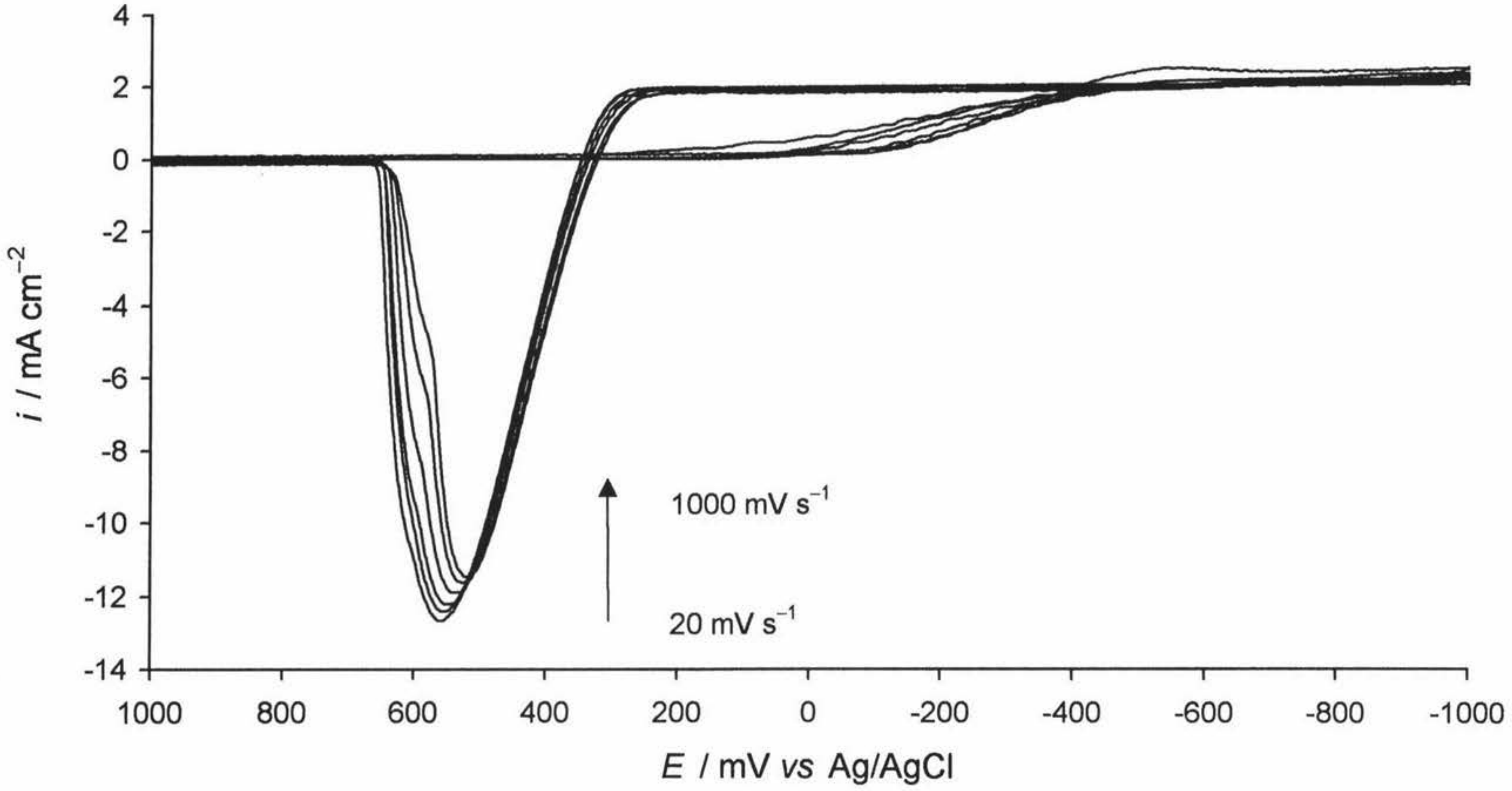

Fig 3.11 A series of voltammograms with varying ν of 20, 50, 100, 200, 500, and 1000 mV s^{-1}. [Hg^{2+}] = 2.0 mM, ω = 1000 rpm.

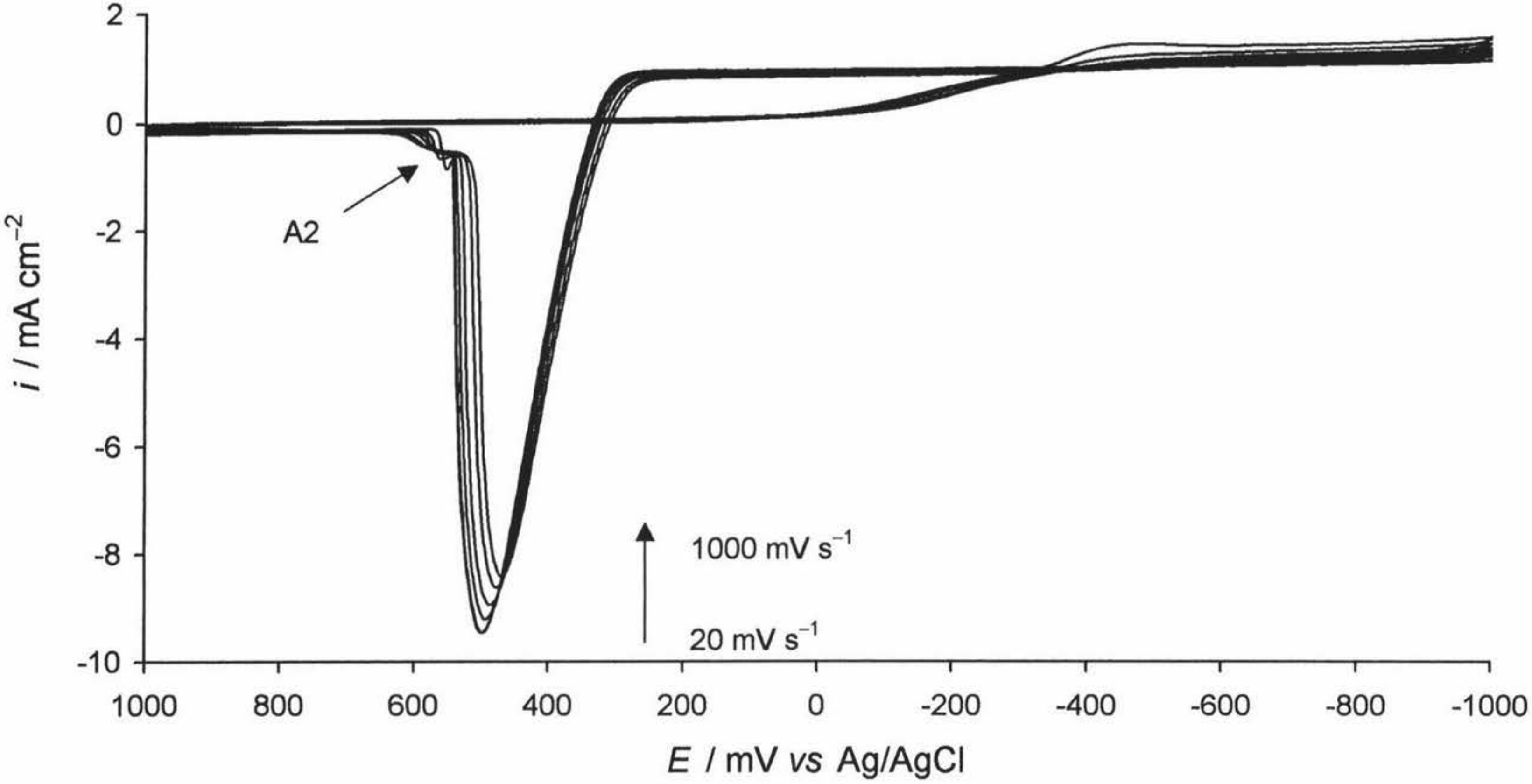

Fig 3.12 A series of voltammograms with varying ν of 20, 50, 100, 200, 500, and 1000 mV s^{-1}. $[Hg^{2+}]$ = 1.0 mM, ω = 1000 rpm.

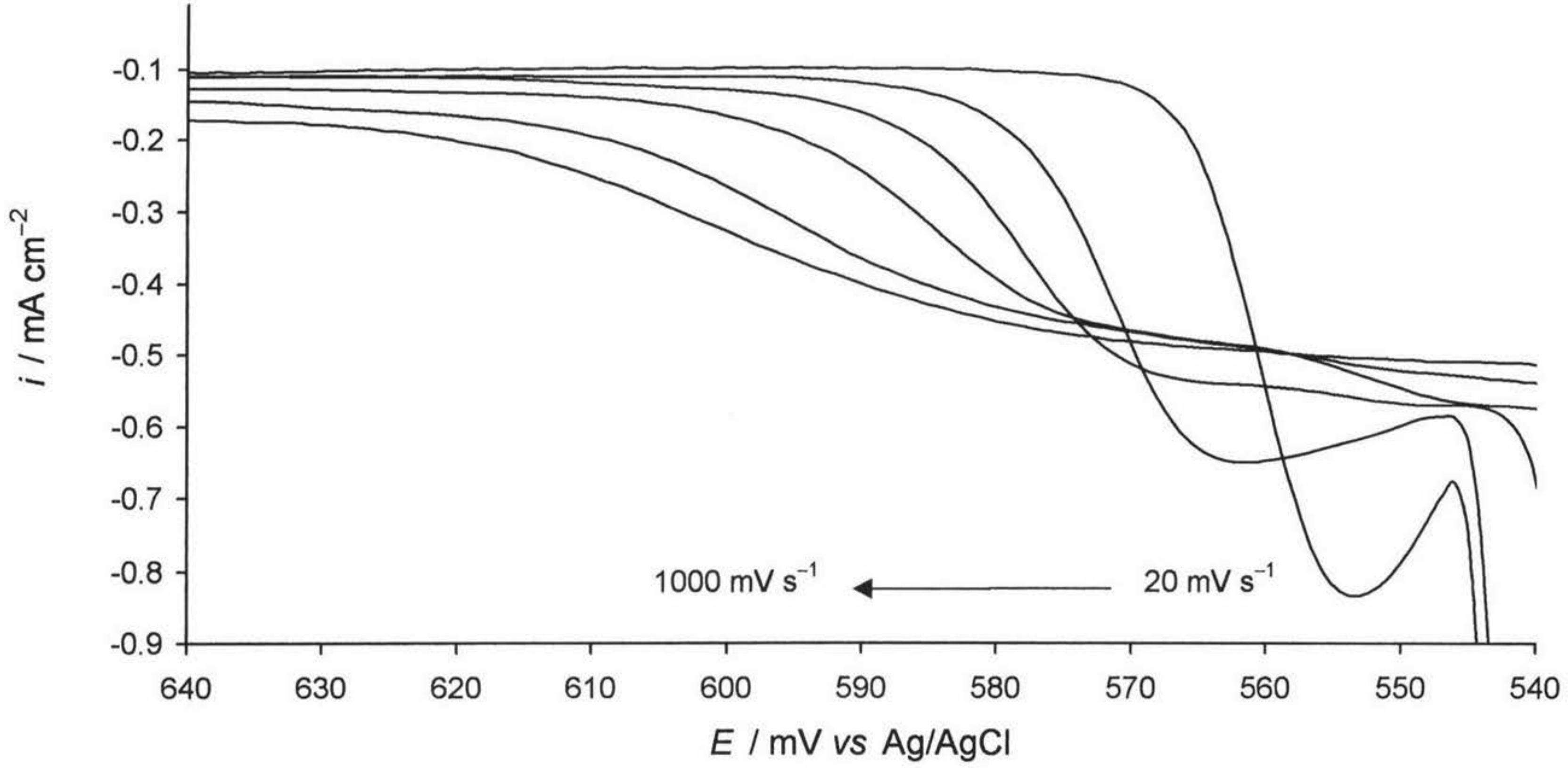

Fig 3.13 An expanded view of the region indicated by A2 in Fig 3.12. ν again varied using 20, 50, 100, 200, 500, and 1000 mV s^{-1} values. [Hg^{2+}] = 1.0 mM, ω = 1000 rpm.

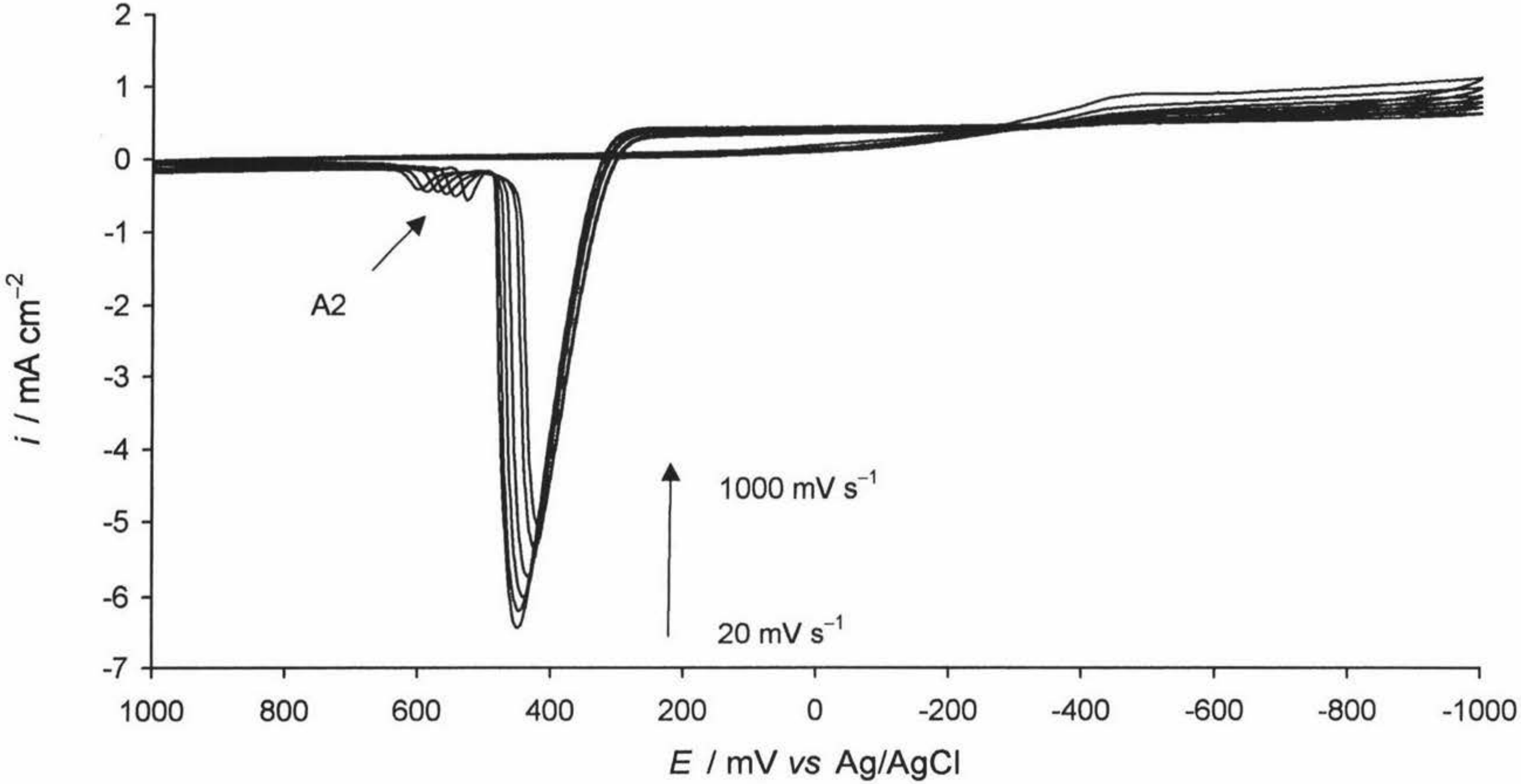

Fig 3.14 A series of voltammograms with varying ν of 20, 50, 100, 200, 500, and 1000 mV s^{-1}. [Hg^{2+}] = 0.5 mM, ω = 1000 rpm.

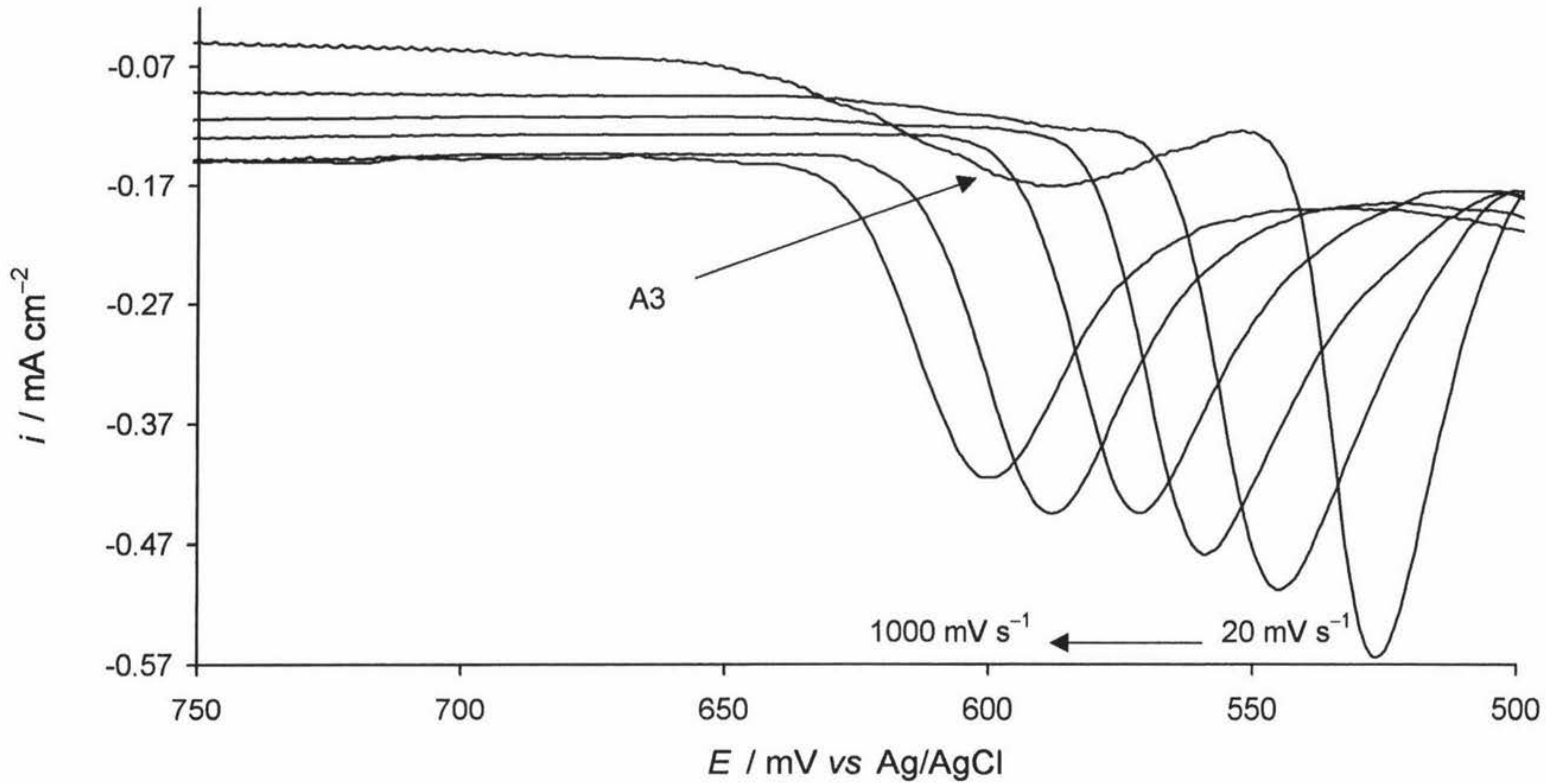

Fig 3.15 An expanded view of the region indicated by A2 in Fig 3.14. ν again varied using 20, 50, 100, 200, 500, and 1000 mV s^{-1} values. [Hg^{2+}] = 0.5 mM, ω = 1000 rpm.

3.7 Rotation Rate Dependence

The rotation rates for all rotation dependence experiments were 630, 1000, 1585, 2500, 4000, 6300, and 10000 rpm selected for regular increase in $\omega^{1/2}$. The rotation dependence was examined for the Hg^{2+} concentration range used earlier in this chapter at a fixed scan rate of 100 mVs^{-1} throughout. All of the voltammograms for the rotation dependence have been obtained after the electrode had previously undergone mechanical-cleaning and cycled seven times until a constant response had been obtained.

Over all concentrations explored as the rotation rates were increased then the observed currents over the entire voltammograms increased and where C1 and C2 form they also increased in amplitude.

Over the rotation range for 10 mM solutions Steady state currents were not attained as shown in Fig 3.16. Current spikes were seen sporadically although they appear to be associated with the C2 peak. As the rotation rate increased the amount of C2 which formed decreased, and the current spikes did not occur above the rotation rate of 2500 rpm.

The oxidation peaks A1 and A2 increased with increasing rotation. The shift in overpotential for onset of reduction with concentration was observed again here for the entire rotation rate, indicating that the shift in E_{red} is not due to any rotation effects.

In the case of 5 mM Hg^{2+}, C1 and C2 were present at each rotation rate and were fully formed with a steady state current being attained by the end of the forward sweeps. The A1 peak was always fully completed by the end of the reverse sweep and increased with increasing rotation rate. The shift in overpotential for E_{red} was seen again here. The rotation dependence of the 5 mM Hg^{2+} concentration is shown in Fig 3.17.

Figure 3.18 shows the rotation dependence for 2 mM Hg^{2+}. C1 and C2 peaks did not form over the rotation rate range. The overpotential shift for E_{red} occurs here but again only to the same extent as detailed in Table 3.1. A1 was always completed by the end of the reverse sweep and it increased steadily with increased rotation rates.

The 1.0 mM concentration also did not have C1 or C2 forming at any of the rotation rates as shown in Fig 3.19. The CV's for this concentration look like that for a freshly mechanically cleaned electrode with rotation rate increases. There was no major shift in reduction overpotential E_{red}. A2 increased with rotation rate, as did A1, but at the rotation rate of 10000 rpm A1 had merged with A2 and could not be observed anymore. A2 appears to shift to more anodic potentials at increased rotation rates.

At the lowest Hg^{2+} concentration of 0.5 mM the A2 peak could also be observed along with A1 as shown in Fig 3.20. Both A1 and A2 increased with increasing rotation rates. A2 was present even at the highest rotation rate of 10000 rpm. C1 and C2 did not form and there was no significant reduction overpotential shift. For this low concentration a steady state current was not achieved on the forward sweep but was achieved on the reverse sweep as seen in Fig 3.20.

3.8 Microelectrode studies

Figure 3.21 shows three voltammograms all of which are from a 5 mM Hg^{2+} concentration in an acetate buffer. One of these voltammograms are taken after mechanical-cleaning, one is after the ME has been cycled without mechanical or electrochemical-cleaning, and the third is the voltammogram after an electrochemical clean has been undertaken.

The E_{red} values for the mechanically-cleaned and the electrochemically-cleaned voltammograms are both +86 mV, and when the ME was cycled without either type of cleaning E_{red} shifts to +360 mV. After the first cycle each voltammogram exhibits many current spikes making it difficult to establish underlying features. There is some evidence for the growth of a peak between –300 and –700 mV but as to whether this peak is C1 or C2 remains unclear. All cycles reach a steady state current by the end of the forward sweep although current spikes are superimposed. There is a very small A2 peak on the cycle associated with no cleaning. The electrochemical cleaning was also performed out on the ME with the 5 mM Hg^{2+} solution. After the first electrochemical-cleaning run of the lowest potential of 1000 mV for 30 seconds, the electrode exhibited voltammograms identical to those collected immediately after mechanical cleaning. The E_{red} value has returned to that of a mechanically cleaned ME, and there are no signs of any peaks or current spikes.

Fig 3.22 shows the voltammagrams for the scan rates of 100, 200, 500, 1000, 2000, 5000, and 10000 mV s^{-1} for 20 mM Hg^{2+}. The voltammograms in Fig 3.22 were collected from an electrode that had not under gone mechanical-cleaning or electrochemical-cleaning prior to their collection.

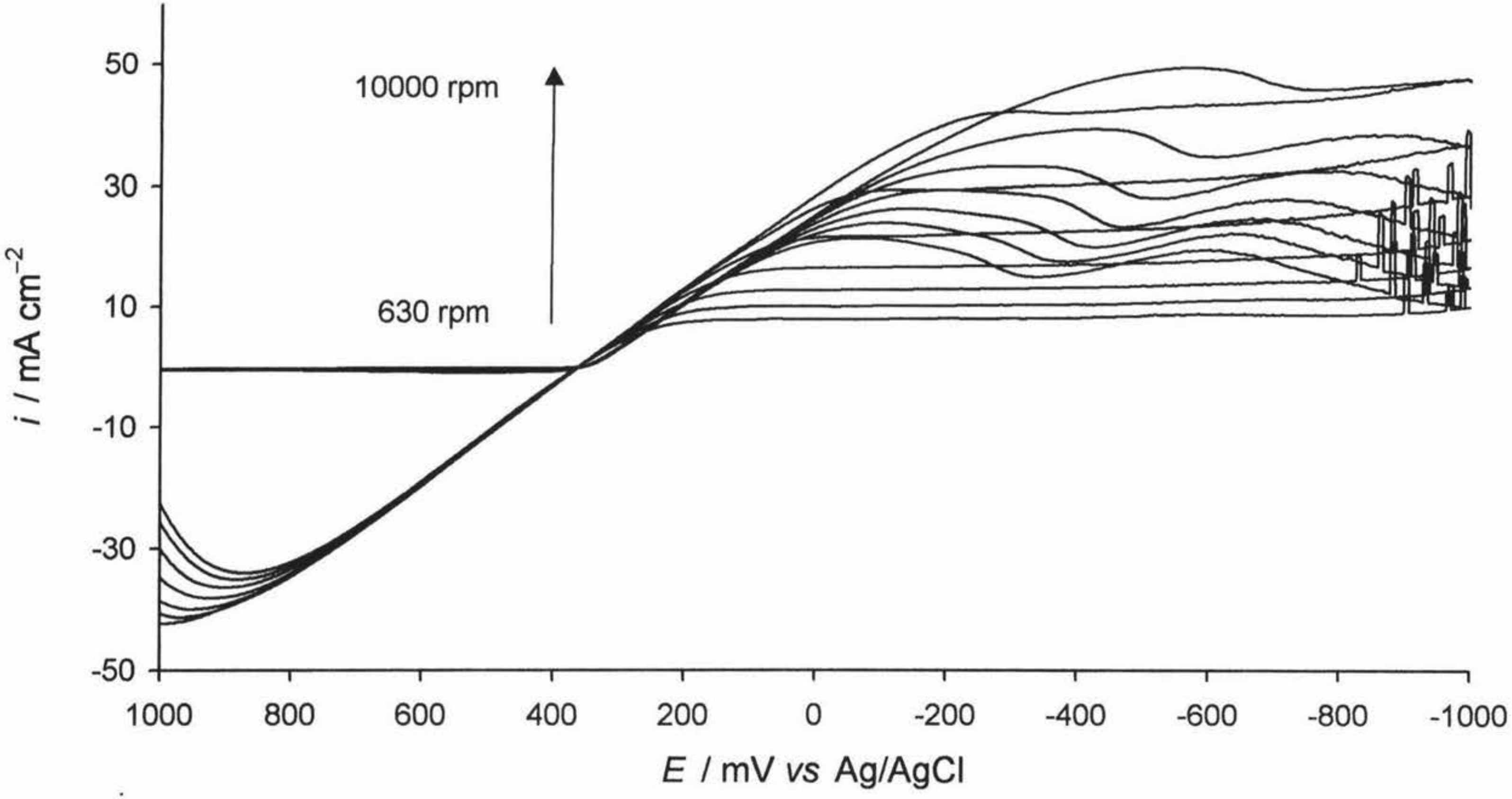

Fig 3.16 A series of voltammograms with varying rotation rates of 630, 1000, 1585, 2500, 4000, 6300, and 10000 rpm. [Hg^{2+}] = 10.0 mM, ν = 100 mV s^{-1}.

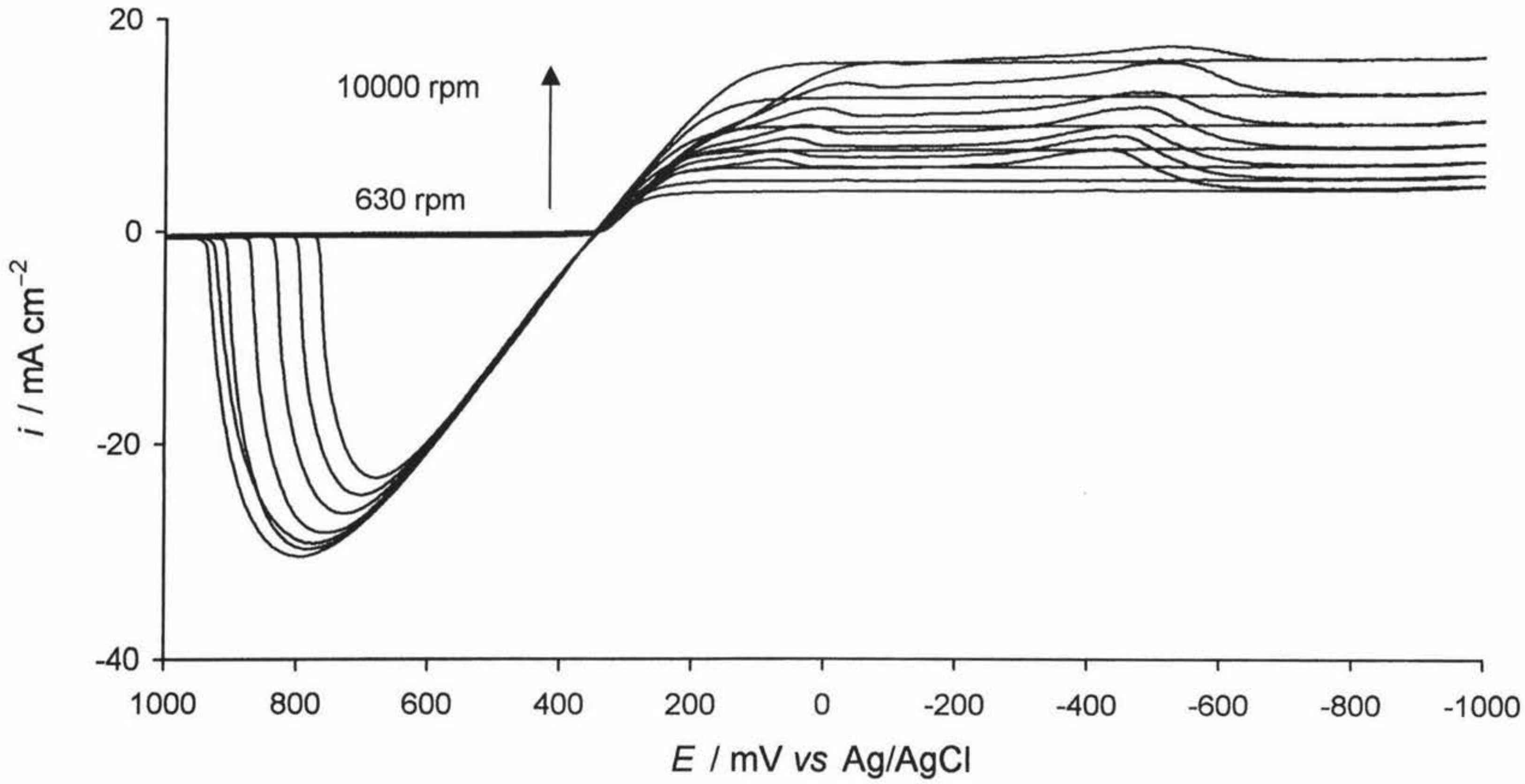

Fig 3.17 A series of voltammograms with varying rotation rates of 630, 1000, 1585, 2500, 4000, 6300, and 10000 rpm. $[Hg^{2+}] = 5.0$ mM, $\nu = 100$ mV s^{-1}.

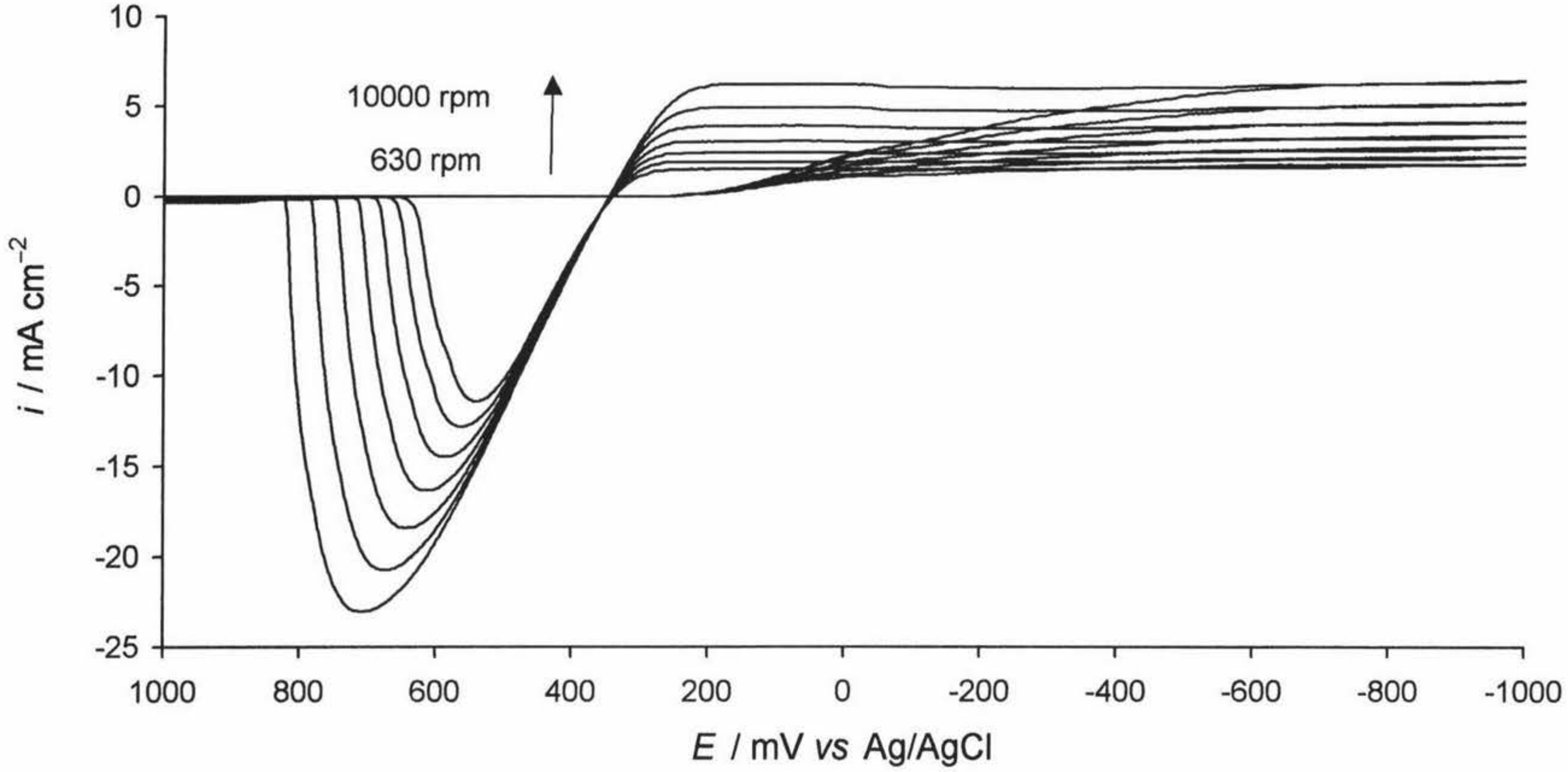

Fig 3.18 A series of voltammograms with varying rotation rates of 630, 1000, 1585, 2500, 4000, 6300, and 10000 rpm. [Hg^{2+}] = 2.0 mM, v = 100 mV s^{-1}.

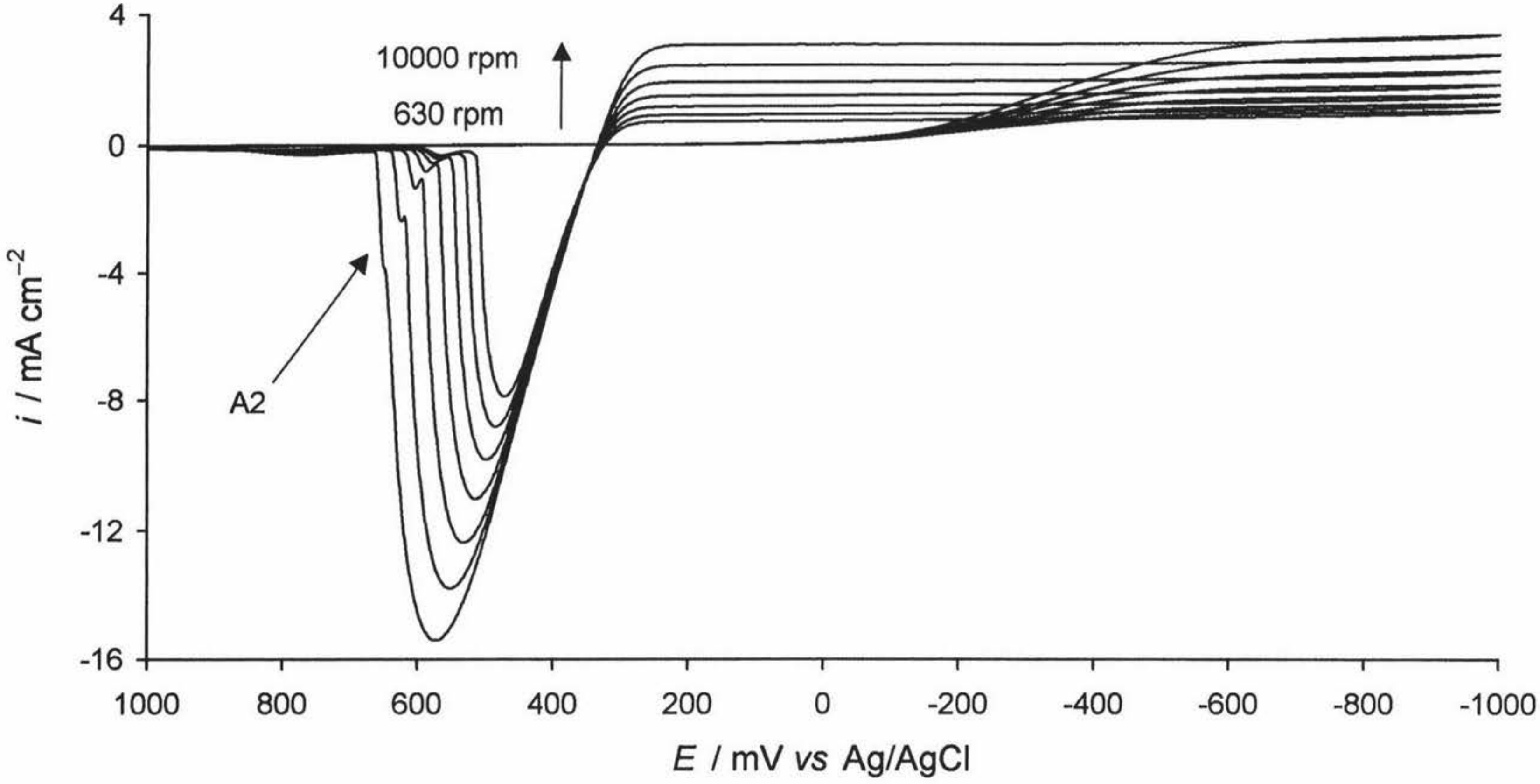

Fig 3.19 A series of voltammograms with varying rotation rates of 630, 1000, 1585, 2500, 4000, 6300, and 10000 rpm. $[Hg^{2+}] = 1.0$ mM, $\nu = 100$ mV s^{-1}.

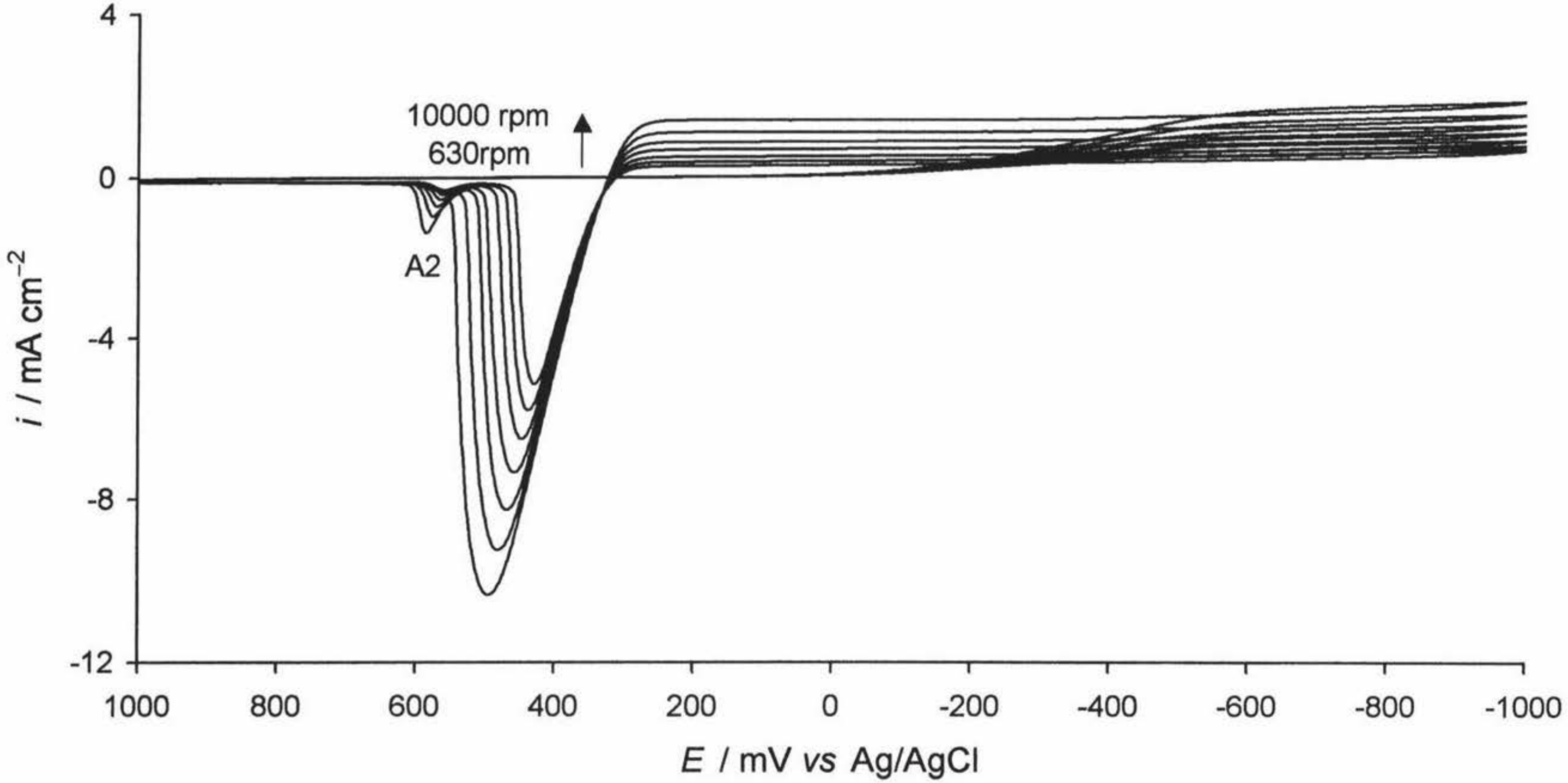

Fig 3.20 A series of voltammograms with varying rotation rates of 630, 1000, 1585, 2500, 4000, 6300, and 10000 rpm. [Hg^{2+}] = 0.5 mM, ν = 100 mV s^{-1}.

There are current spikes throughout each cycle, which occur randomly between the onset of reduction and to just before the start of oxidation. With increasing scan rate the amplitude and frequency of the cathodic current spikes increase, with the scan rate of 10000 mV s^{-1} having the most frequent and largest spikes. Here E_{red} does not vary significantly between successive cycles even though these were collected on a ME that had not been cleaned.

A new feature, which had not been observed when using the macro electrodes, is a dip and then the growth of a very small peak on the return sweep at around +200 mV. It can first be noticed at the scan rate of 500 mVs^{-1} very faintly, and gets more pronounced with increasing scan rate.

Another feature in this scan rate dependence on microelectrodes is what could be the first signs of the growth of the C1 peak. The rise in current, which may be the start of the formation of C1, can only be observed at the very high scan rates of 5000 and 10000 mV s^{-1}.

The last feature that can be observed from Fig 3.22 relates to the anodic peaks. The A1 peak is small in comparison with the peak at +600 mV. Each of these peaks is increasing with the increasing scan rate. However the second peak at a much higher rate then the A1 peak. This other peak may be A2, but on other electrodes it was never observed to increase to this extent and was never found to be larger than the A1 peak.

3.9 C1 and C2 after open circuit conditions

Figure 3.23 shows the voltammograms of a 10 mM Hg^{2+} solution in an acetate buffer which displays the effect of establishing the C1 and C2 peaks with a series of CV cycles and then leaving the electrode between cycles at open potential for increasing periods of time. In this figure the first cycle after mechanical cleaning does not have C1 or C2 present and it has a small A1 peak labeled (1). The electrode was cycled without cleaning until C1 and C2 were fully formed and not changing from cycle to cycle, this is the cycle with the highest current value for C1 and C2 in Fig 3.23 and identified as (2). The electrode was then left at open potential for 30 seconds and then cycled again. The first four cycles do not show a marked difference so the time left at open potential was increased successively in a logarithmic fashion. After 18.5 minutes at open circuit a large drop in C1 and C2 was noticed with a corresponding decrease in A1. With increasing open circuit period C1 and C2 were still

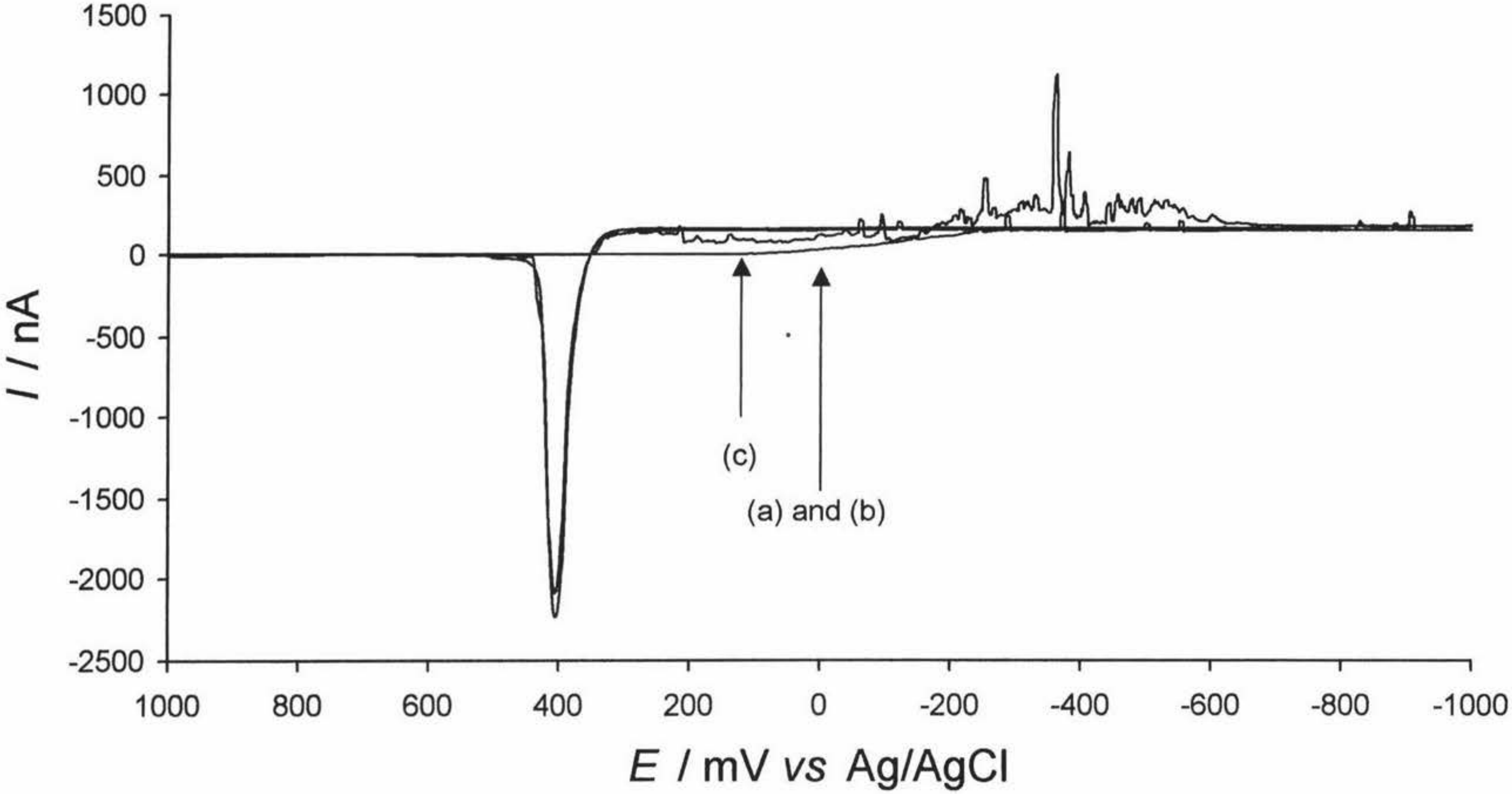

Fig 3.21 A series of three voltammograms using a ME, $[Hg^{2+}] = 5.0$ mM, $\nu = 100$ mV s^{-1}. (1) indicates the mechanically-cleaned cycle, (2) indicates the electrochemically-cleaned cycle, and (3) indicates the cycle where neither mechanical nor electrochemical-cleaning has been undertaken.

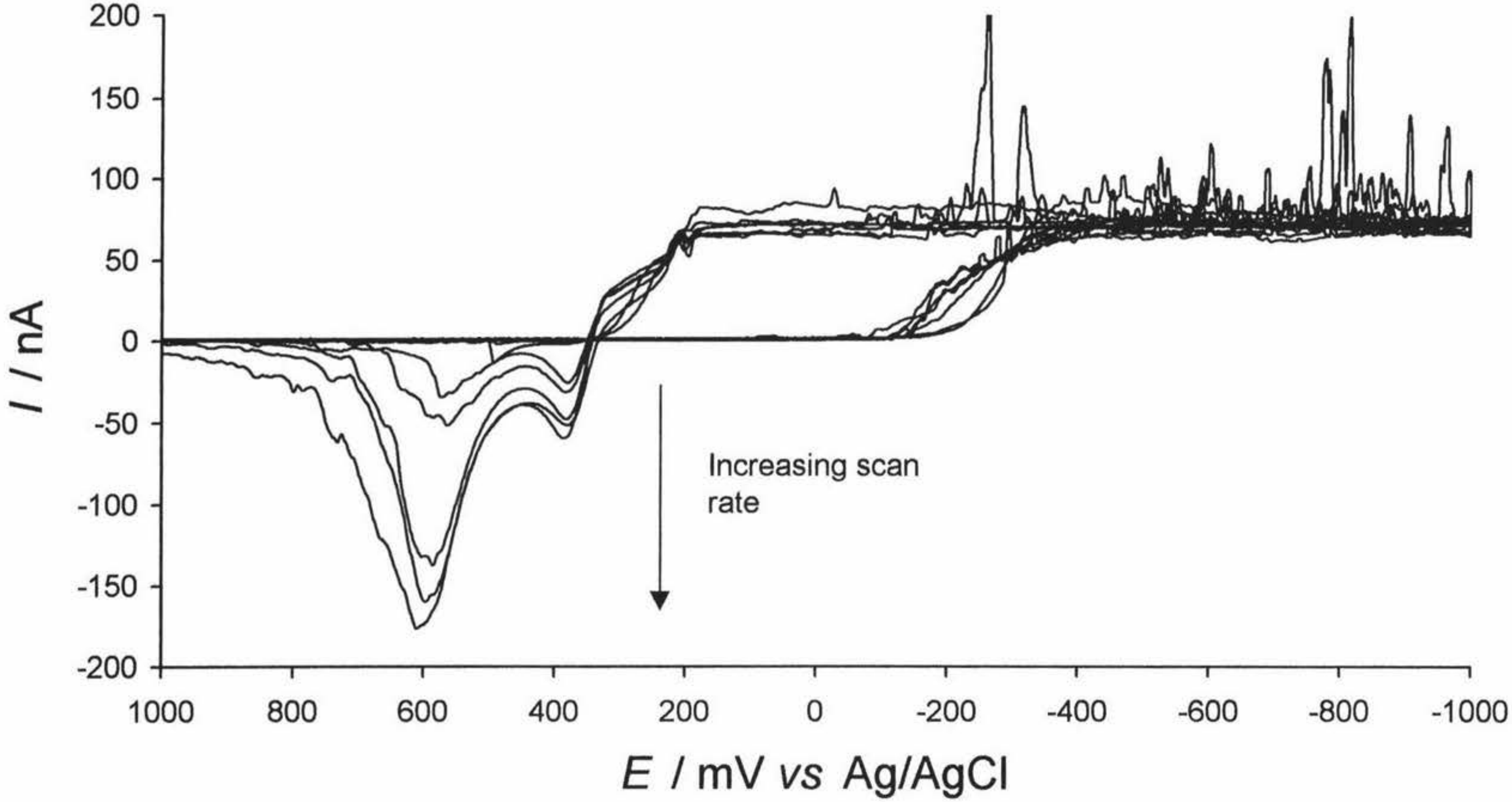

Fig 3.22 A series of voltammograms with varying ν of 100, 200, 500, 1000, 2000, 5000, and 10000 mV s^{-1} using a ME. $[Hg^{2+}]$ = 20.0mM.

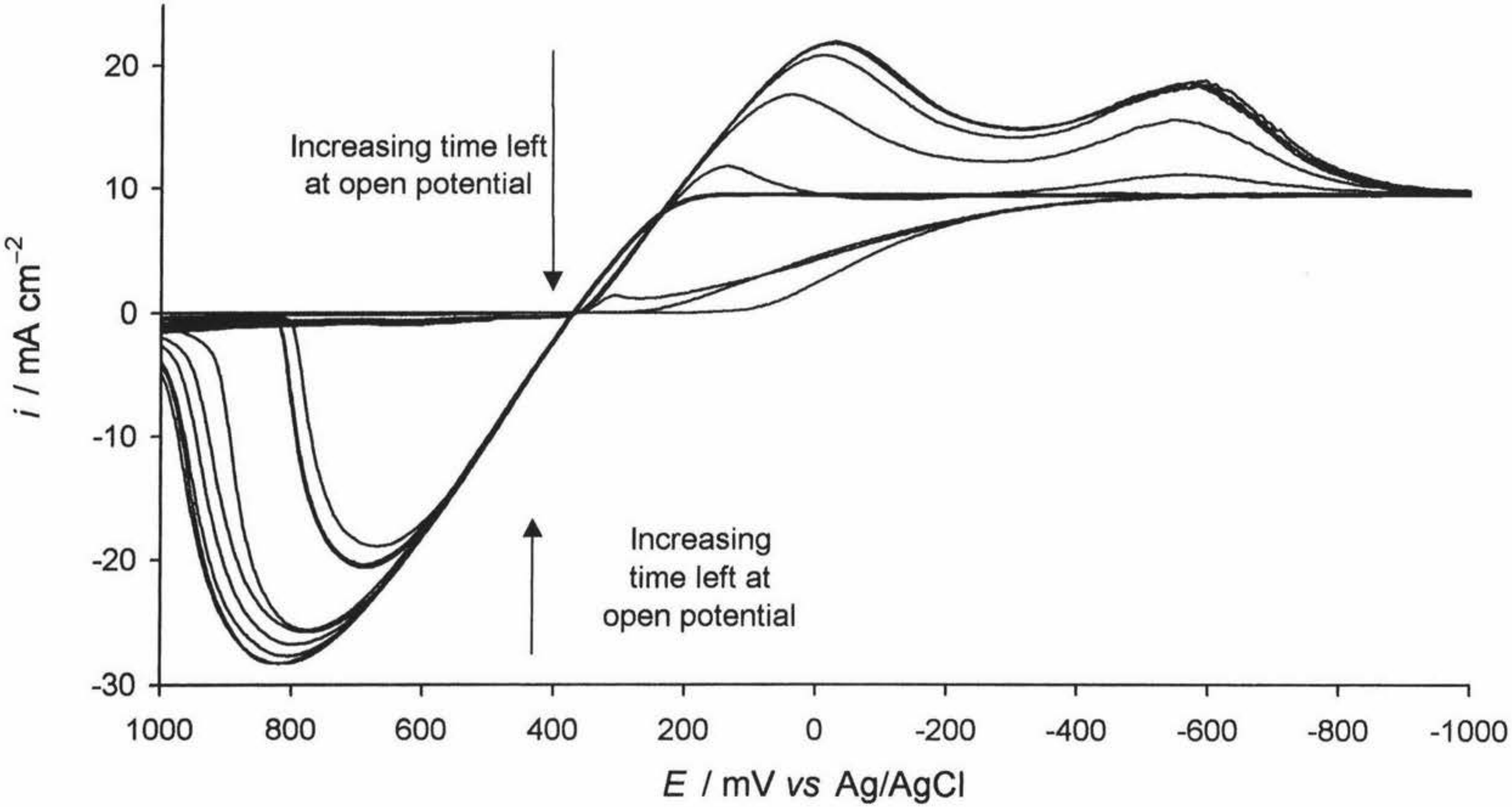

Fig 3.23 A series of voltammograms where the time between cycles at open potential was increased. [Hg^{2+}] = 10.0 mM, ω = 1000 rpm, and ν = 100 mV s^{-1}.

evident but only just reach above the steady state current. After 38.5 minutes a very small C1 peak arises then the current rises to the steady state level and stops increasing there, there are no signs C2 at all. On the last cycle shown, after having left the electrode at open potential for 145.5 minutes between cycles, there are no signs of C1 or C2. Reduction simply commences and the current rises to steady state in a similar manner to a freshly mechanically-cleaned electrode. The other feature of interest is the shift in the overpotential to negative potentials and approaches the E_{red} value of a mechanically cleaned electrode.

The same trends are seen for a concentration of 5.0 mM Hg^{2+}, but the disappearance of C1 and C2 occurs much more rapidly than in the 10.0 mM solution. The complete removal of C1 and C2 and the shift of E_{red} to a freshly mechanically-cleaned response requires only 48.5 minutes at open potential for 5.0 mM Hg^{2+} compared to 145.5 minutes at 10.0 mM Hg^{2+}.

3.10 Cleaning potentials/ Cleaning times.

Depending on the potential which is chosen in the undertaking of the electrochemical cleaning and the time chosen to leave the electrochemical cleaning procedure on for, has an effect on the electrode surface in the case of this work.

It can be seen in Table 3.2 that as concentration increases it takes increasing higher potential and longer times for the cleaning of the electrode to be close to the same profile as the cycle after mechanical-cleaning. For the 20 mM Hg^{2+} solution 1000 and 1100 mV cleaning potential were not examined due to the length of time which would be required to achieve a voltammogram which resembled that of a mechanically-cleaned electrode. In all three concentrations the time required at the cleaning potential decreases as the potential of the cleaning procedure be increased.

The other trend is presented in Table 3.3. Here the total cleaning times for a constant cleaning potential of 1300 mV for the concentration range shown. It can be seen that at higher concentrations it takes longer lengths of time to electrochemically clean the electrode than it does at lower concentrations. There are no results for 0.5 and 1.0 mM Hg^{2+} concentrations as they never formed C1 or C2 during their cycling therefore there was not anything to clean away from the electrode.

	Potential (mV)						
[Hg^{2+}] (mM)	1000	1100	1200	1300	1400	1500	1600
20	–	–	2115	583	435	315	75
10	–	1783	585	435	315	315	315
5	315	315	295	225	165	115	–

Table 3.2 Total cleaning times required at varying cleaning potential for varying concentrations of 20, 10, and 5 mM Hg^{2+}. (time in seconds)

[Hg^{2+}] (mM)	Total time (sec)
20.0	583
10.0	435
5.0	225
2.0	10
1.0	–
0.5	–

Table 3.3 Total time held at an electrochemical cleaning potential of 1300 mV for the Hg^{2+} concentration range of 0.5 to 20.0 mM.

3.11 Electrochemical cleaning

In the electrochemical cleaning experiments undertaken as part of the work in this thesis the following procedure was used. The electrode was firstly cleaned, mechanically, then cycled seven times until a constant response was achieved with C1 and C2 being established. Once C1 and C2 had been established and were not changing between cycles the electrode was then electrochemically cleaned at zero rotation rate. The experiments were all undertaken at fixed rotation of 1000 rpm and fixed scan rate of 100 mV s^{-1}, with the value of the electrochemical cleaning potential being increased in steps of 1000 mV from +1000 to +1600 mV. The electrochemical cleaning times were fixed at 30 seconds for each of these potentials. In Fig 3.24 the voltammograms of a mechanically-cleaned electrode and electrochemically-cleaned electrode are shown, with E_{red} being at 62 mV and the smallest A1 peak corresponds to the mechanically-cleaned cycle. The voltammogram after C1 and C2 had been established has the highest C1 peak. After mechanical cleaning E_{red} shifts to +350 mV. When the electrode was put through an electrochemical clean of 1000 mV for 30 seconds the next cycle produced a voltammogram with a diminished C1 but an increased C2. This trend of C1 decreasing and C2 increasing prevails until the cleaning potential was +1400 mV. Here, C1 still decreases but C2 also starts to decrease. At +1400 mV E_{red} also starts moving to more cathodic potentials and by +1600 mV there is no sign of C1 or C2, and the E_{red} returns to +62 mV. The voltammogram of the cycle after the +1600 mV electrochemical-clean is close to that of a mechanically-cleaned electrode.

3.12 Nitrate

The first current-potential waves after the glassy carbon electrode had been mechanically cleaned do not appear to be very different between mercuric nitrate and mercuric acetate solutions of the same concentration. One of the first differences that is observed is in the values for E_{red}, the values are +240 mV and +67 mV for nitrate and acetate solutions respectively. On the return sweep oxidation commences at +420 mV and +200 mV for nitrate and acetate solutions respectively. The first difference between nitrate and acetate voltammograms on a mechanically-cleaned electrode and following cycles recorded without either mechanical or electrochemical-cleaning, can be seen in Figs 3.25 and 3.26 respectively. Figure 3.25 shows the voltammograms for a 5 mM Hg^{2+} nitrate, one after

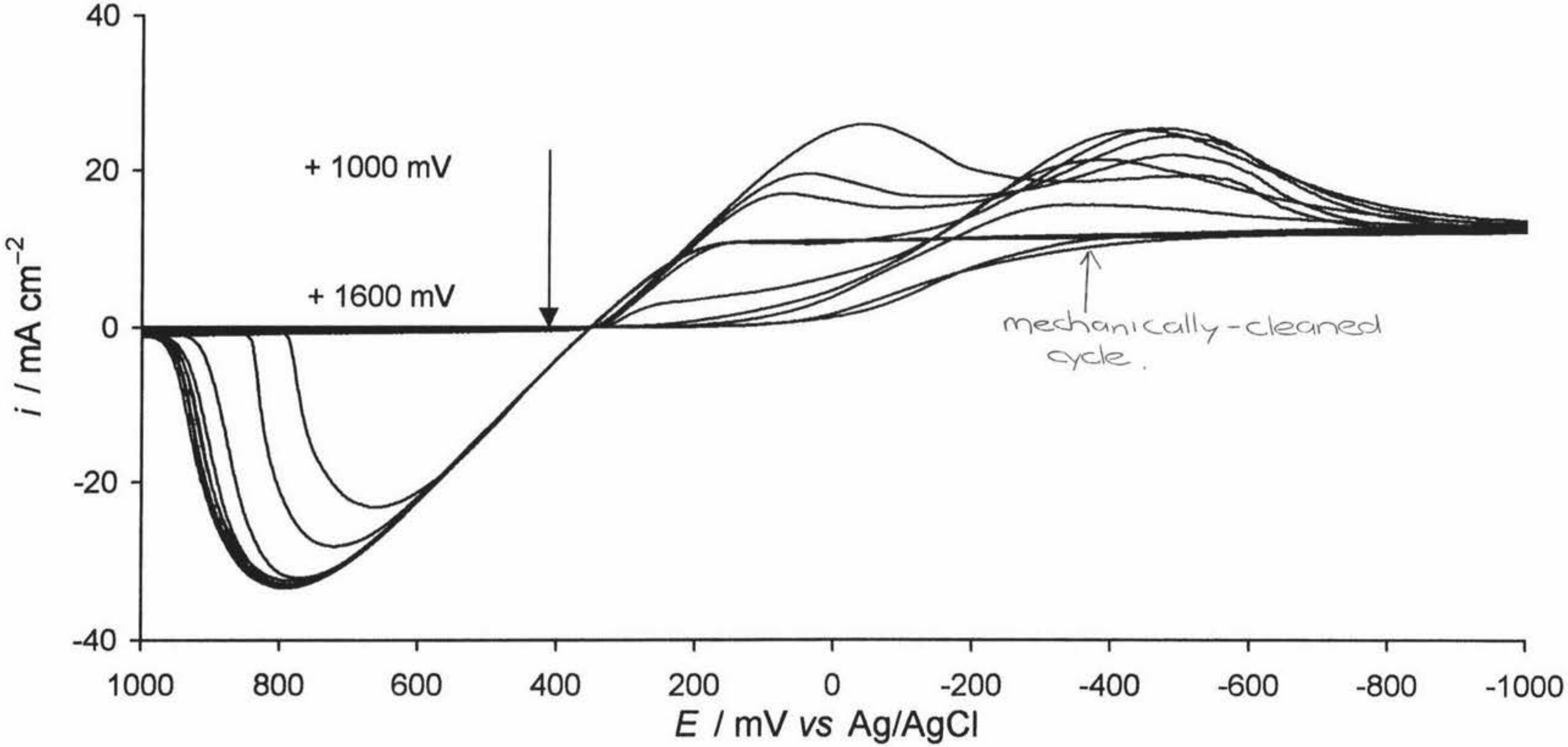

mechanically-cleaned cycle.

Fig 3.24 A series of voltammograms which have undergone electrochemical-cleaning. The varying electrochemical-cleaning potentials used were 1000, 1100, 1200, 1300, 1400, 1500, and 1600 mV. Cleaning time for all was 30 sec., $[Hg^{2+}] = 10.0$ mM, $\omega = 1000$ rpm, $\nu = 100$ mV s^{-1}.

mechanical-cleaning and the other after the seventh cycle proceeding mechanical-cleaning. It can be seen that there is no great difference between the first and seventh cycles in the nitrate solution and that a consistent response is achieved. In the acetate solution, as shown in Fig 3.26 however, the response has been shown to be greatly different in subsequent cycles after the first mechanically-cleaned cycle.

C1 and C2 do not form at any stage in the nitrate solutions no matter what the Hg^{2+} concentration, scan rate or what rotation rate is selected.

Figure 3.27 shows the scan rate dependence of a 5 mM Hg^{2+} solution in nitrate. This response is a significantly different from that seen in Fig 3.10 for acetate. There is no evidence for C1 or C2 peaks, all that is seen is an increase is the amplitude of A1 as the scan rate is increased which would be expected. The steady state current within each voltammogram is constant with no variation is the cathodic region of series of experiments.

Figure 3.28 shows the voltammograms for the rotation dependence of the same 5 mM Hg^{2+} solution in nitrate at fixed scan rate. Again when compared to Fig 3.17 for a comparable acetate solution the response in nitrate can be seen to be significantly different with the absence of C1 and C2. The steady state current increases with increasing rotation rate. For the first four rotation rates, 630, 1000, 1585, 2500 rpm, the size of A1 increases but above the rotation rate of 2500 rpm A1 decreases in size. This in contrast was not observed in the 5 mM rotation rate dependence of the acetate solutions. There is also a dip in the steady state current for every rotation rate and occurs around 100 mV for each cycle.

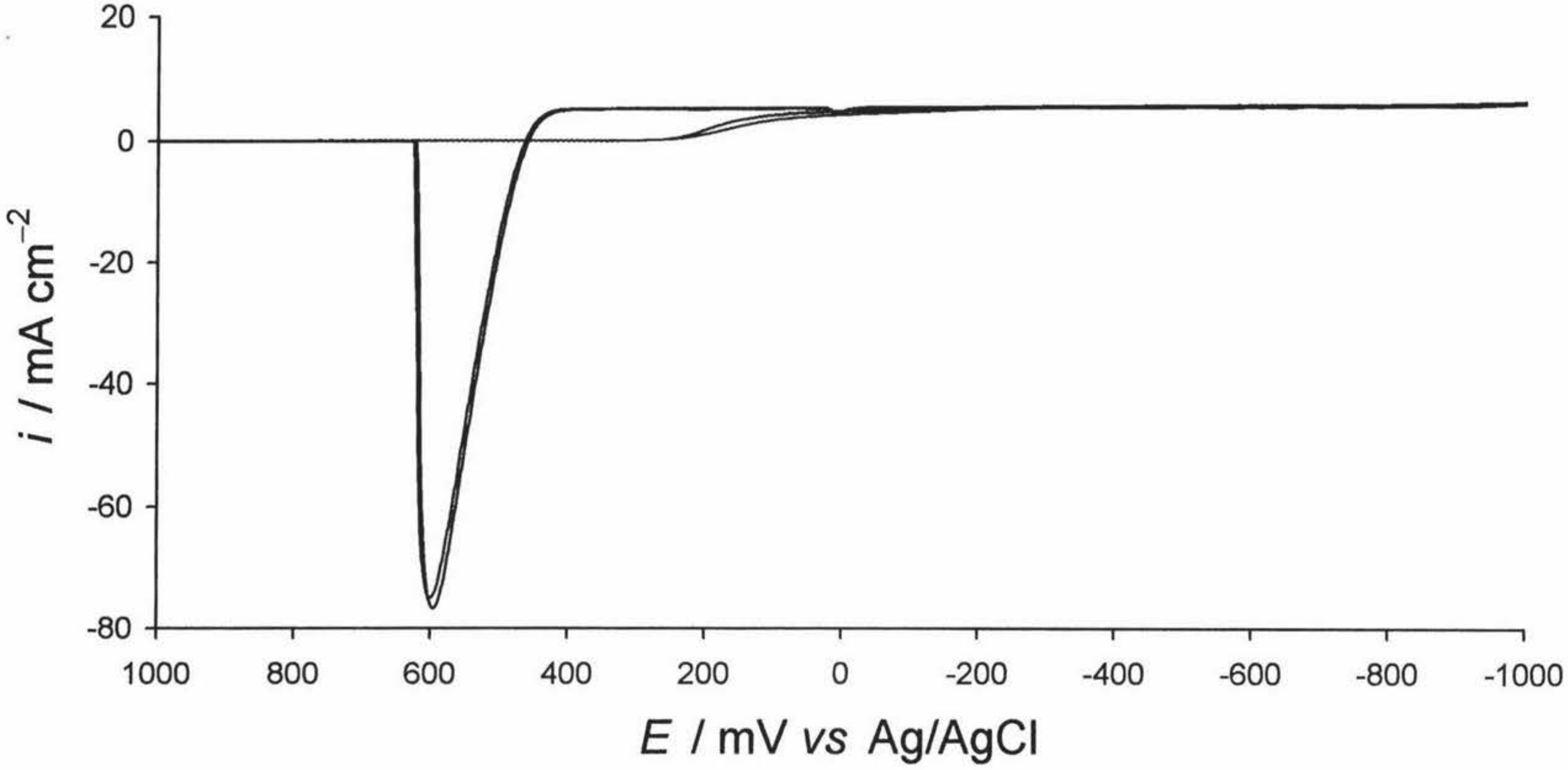

Fig 3.25 The first and second voltammograms recorded after mechanical-cleaning in a nitrate buffer. [Hg^{2+}] = 5.0 mM, ω = 1000 rpm, ν = 100 mV s^{-1}.

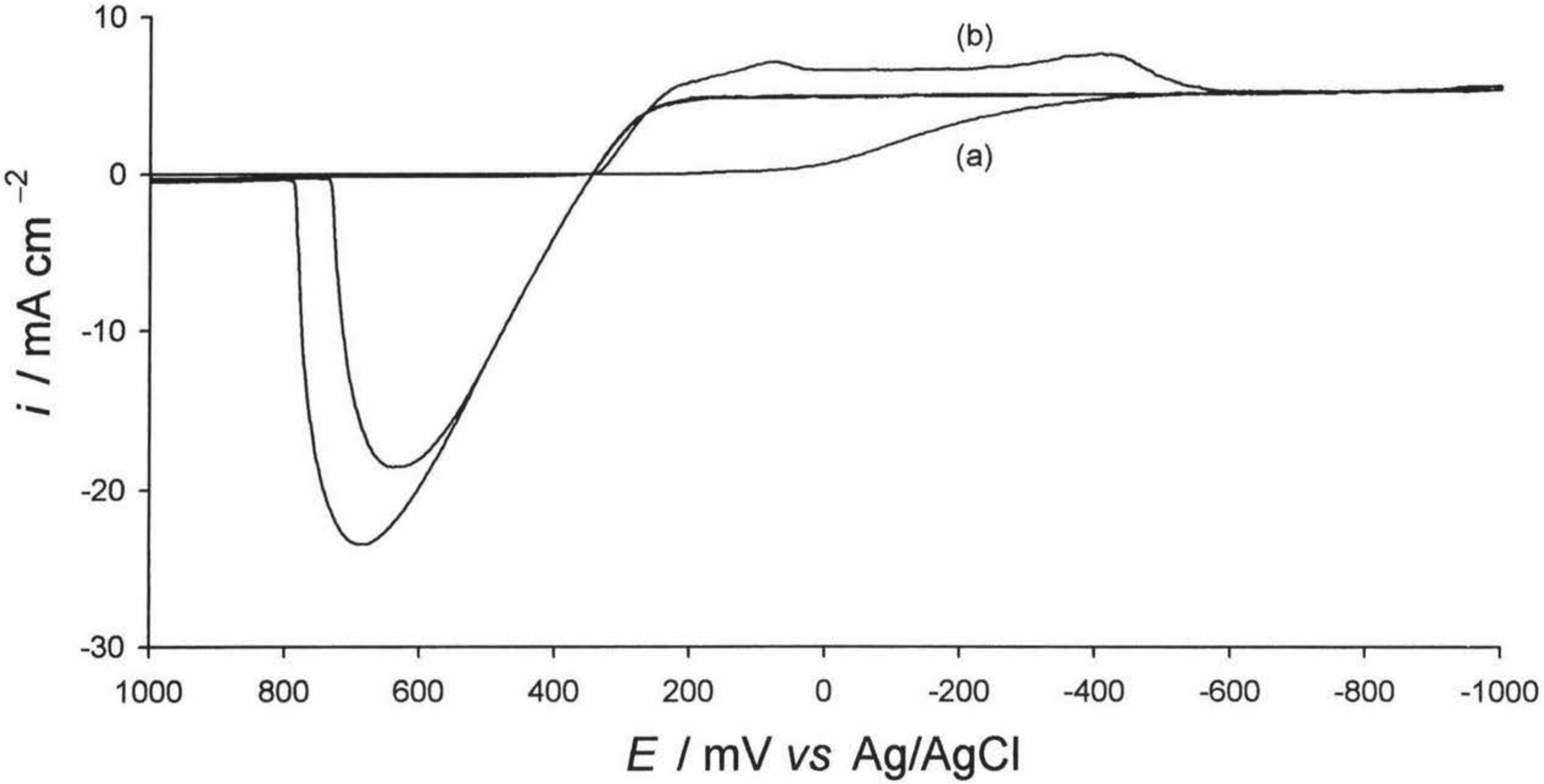

Fig 3.26 The first and second voltammograms recorded after mechanical-cleaning, (a) and (b) respectively, in an acetate buffer. $[Hg^{2+}]$ = 5.0 mM, ω = 1000 rpm, v = 100 mV s^{-1}.

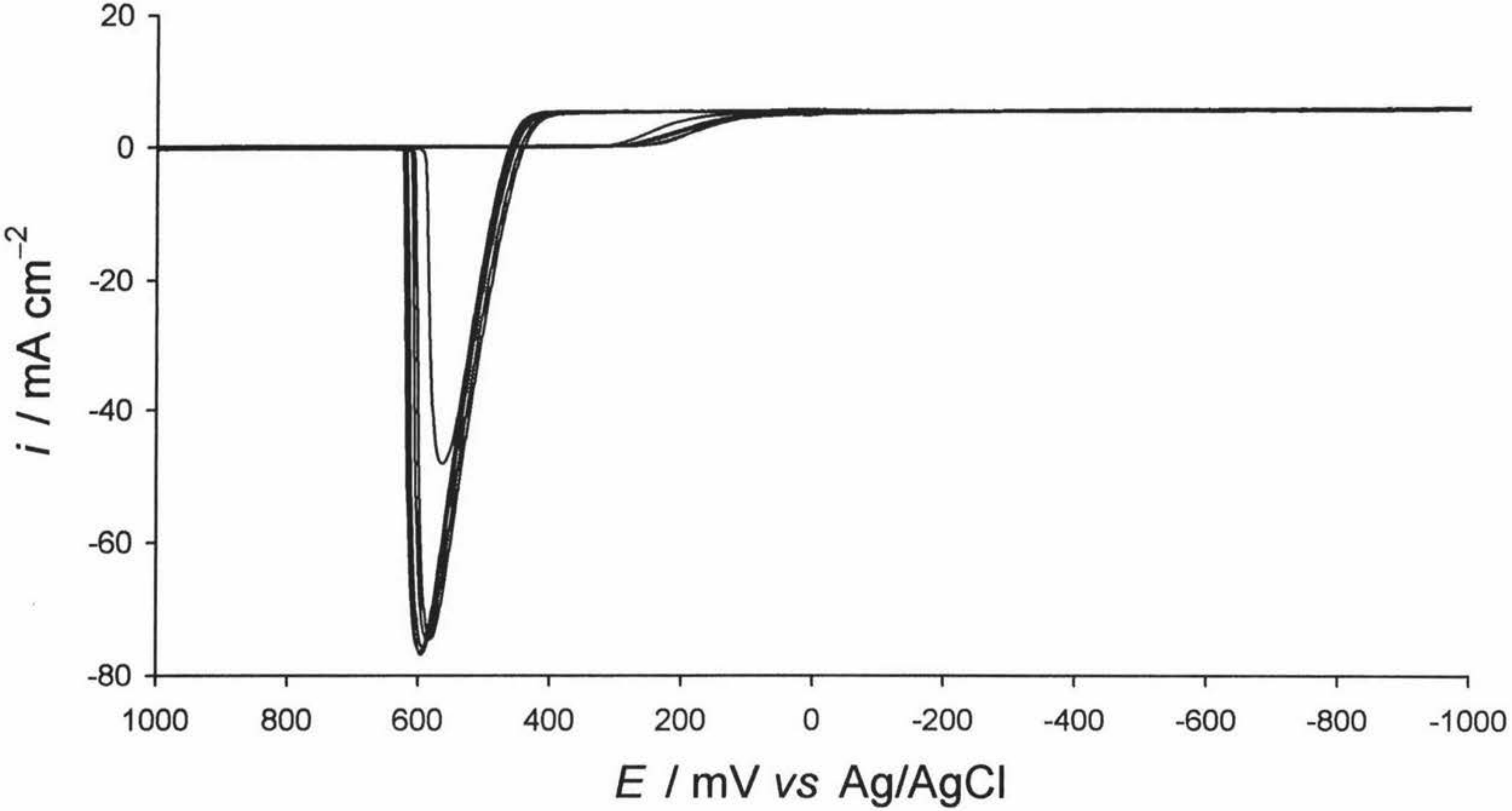

Fig 3.27 A series of voltammograms with varying ν of 20, 50, 100, 200, 500, and 1000 mV s^{-1}. [Hg^{2+}] = 5.0 mM, ω = 1000 rpm. In nitrate buffer.

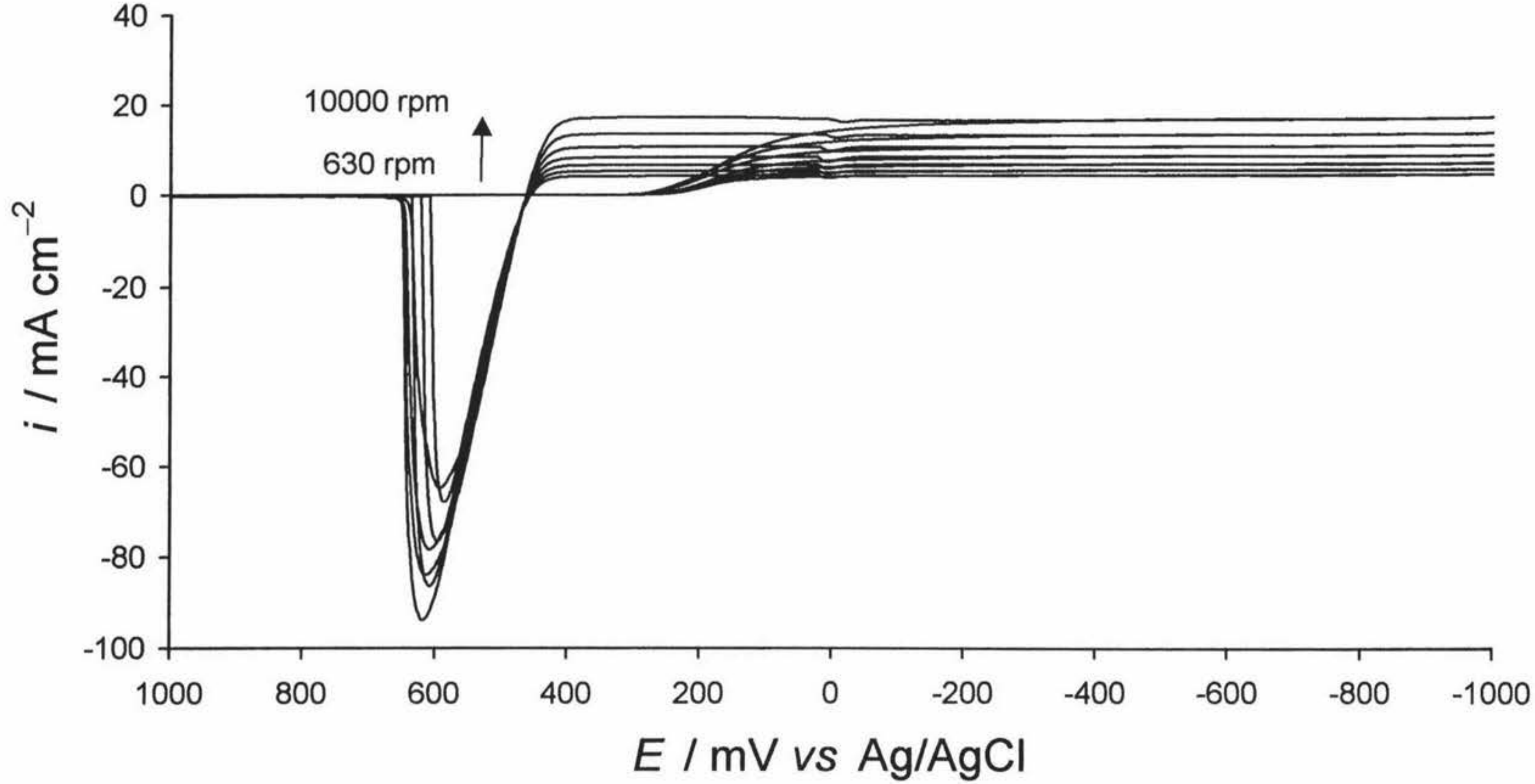

Fig 3.28 A series of voltammograms with varying ω of 630, 1000, 1585, 2500, 4000, 6300, and 10000 rpm. [Hg^{2+}] = 5.0 mM, ν = 100 mV s^{-1}. In nitrate buffer.

CHAPTER 4

Chronoamperometry studies

4.1 Introduction

The focus of this chapter is the experimental results and observations of the chronoamperometry section of this work. The effect of concentration, the step potential, and rotation rate on the GC RDE will be detailed. CA studies on a GC ME were also studied and the features within this set of experimental results are examined here. The interpretation of the detailed observations will be discussed in Chapter 5.

4.2 Chronoamperometry

In potential step experiments the potential of the WE is changed instantaneously, from one value to another [73]. Either the current-time response or the charge-time response is recorded. The variation of the current response with time under such potentiostatic control is called chronoamperometry. An experiment is usually performed by stepping the potential applied to a working electrode from a value where there is little or no electron reaction, E_1, to a potential, E_2, at which a current response, for in this case the reduction of mercury, may be recorded.

Fick's First Law for the rate of diffusion or flux, is directly proportional to the concentration gradient

$$j_{(x,t)} = \frac{-D\delta c_{(x,t)}}{\delta x} \tag{4.1}$$

where D is the diffusion coefficient of $[Hg^{2+}]$ in $m^2\ s^{-1}$, and $\delta c_{(x,\ t)}/\ \delta x$ is the concentration gradient at time t at distance x from the electrode. The flux, j, is the rate of mass transport at a fixed point and is defined as the number of molecules passing through a unit area of an imaginary plane perpendicular to the direction of moment per unit of time, and has the units mol $m^{-2}\ s^{-1}$.

The current is directly proportional to the flux, given by

$$i = -nFj \tag{4.2}$$

where n is the number of electrons transferred in the reaction and F is the faraday constant. The combination of equations 4.1 and 4.2 provides a general expression for the current that shows at any time the current is proportional to the concentration gradient of the electroactive species.

$$i = \frac{-nFD\delta c_{(x,t)}}{\delta x} \tag{4.3}$$

4.3 RDE experimental observations

4.3.1 *Concentration and potential dependence*

The Hg^{2+} concentrations selected to study the response achieved by the CA technique using the GC RDE were 2.0, 5.0, and 10.0 mM. For all CA runs, the E_1 was set to +550 mV, the reduction potentials, E_2, ranged from +350 to –500 mV in steps of 50 mV.

With increasing concentration, the overall currents achieved increased which is to be expected. The predominate features are generally similar for each of the three concentrations. Fig 4.1 is an example of a CA experiment under these set conditions to illustrate the main features that were found in this work.

At the highest E_2 value of +350 mV each concentration achieved a close to steady state current–time by the end of 32 sec. At 2 mM Hg^{2+} a steady state current was not reached until the E_2 value was decreased to –450 mV. The current achieved by each run moves closer to the steady state current. At 5 mM Hg^{2+} steady state current is reached by the end of 32 sec at the E_2 potential of –50 mV, but at potentials more positive than –50 mV the steady state is attained rapidly. At 10 mM Hg^{2+} a steady state current is not attained over the time limitation of 32 sec. The optimum concentration appears to be that of 5 mM Hg^{2+} for reaching steady state. Below this concentration the E_2 potential required to achieve features like the steady state current, are more negative.

Similar features observed for the 5 mM Hg^{2+} solutions are also evident for the other two concentrations that were selected for study. The initial drop in current, rising slowly to an

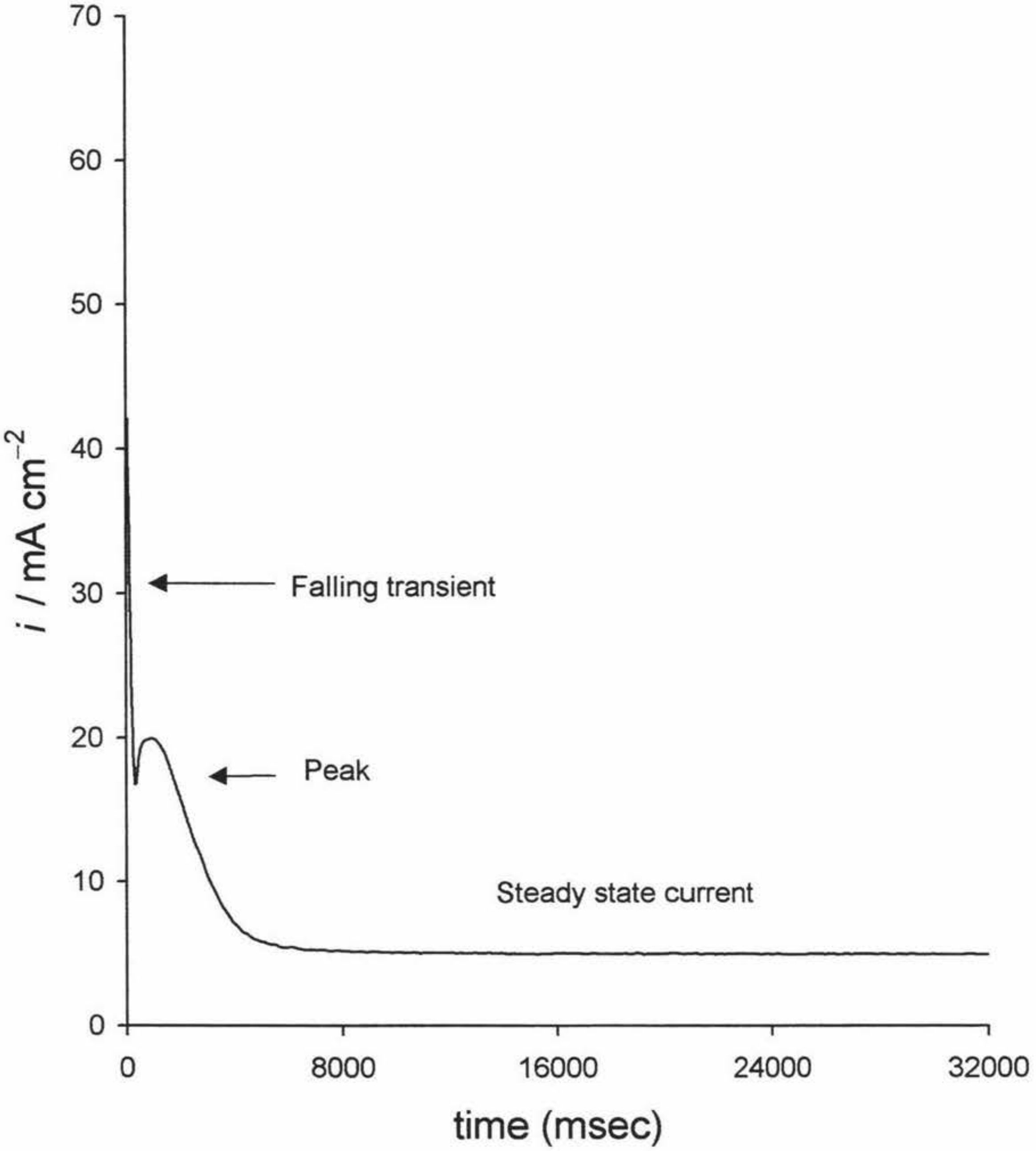

Fig 4.1 A general CA transient displaying the steady state current, the falling transient, and the peak which develops. [Hg^{2+}] = 5.0 mM, E_1 = 550 mV, ω = 1000 rpm.

apparent steady state, the growth of a peak before a decrease in current down to a steady state current. All of these features are observed but all are seen much clearer at the concentration of 5 mM Hg^{2+}. This concentration appears to be the optimum concentration for CA experiments.

The dependence of the value used for the E_2 potential is quite apparent when the results are looked at. With decreasing the E_2 potential making it more cathodic the initial current value increases whether or not it then starts to decrease or increase from that point or not. The potentials where the different features within the CA runs occur vary with both concentration and rotation rate. At more positive E_2 values of +350 to +150 mV not a lot occurs within a run, just the smooth gradual increase to what is presumed to be a steady state current. As the value for E_2 is decreased the closer the current reaches to achieving the steady state current value by the end of the 32 sec time restraint.

Figure 4.2 shows the multigraph of E_2 potential values of +200 to –500 mV, dropping in 100 mV steps, for a 2 mM Hg^{2+} concentration, at a rotation rate of 4000 rpm. Here it can be seen that with decreasing the potential new features that were mentioned above start to occur.

Figure 4.3 has four different E_2 potential values plotted for a 5 mM Hg^{2+} concentration. Again this is shown to point out the features which are occurring as the value of the E_2 potential is made to be more cathodic.

4.3.2 Rotation Dependence

When the concentration and value of E_2 are kept constant and the rotation rate is varied the results received are very different as well. The rotation dependence for the concentration of 5.0 and 10.0 mM were examined in this work. At the high value of 200 mV for E_2 at the 10.0 mM concentration the results have no real pattern to them. Figure 4.4 shows the plot of this. Very different features can be seen throughout this figure. It seems that at high E_2 values, high rotation rates are required to achieve common trends. As the value of E_2 is decreased more normal trends are observed. By this it is meant that as rotation rate is increased the current reached also increases, but the same features are seen throughout. The steady state currents increase with increasing rotation rate as well. Fig 4.5 shows the rotation rate dependence of a 10.0 mM solution at E_2 value of –50 mV. Here it can be seen that the initial current at the start of the run increases as rotation rate increases, and the steady state current is increasing with increasing rotation rate. The run which seems like it does not fit in is the run for 630 rpm and the only difference between this and the others is that it has taken a longer amount of time to complete the formation of the peak and the completion of the following falling transient.

At the lower concentration of 5 mM Hg^{2+} the rotation rate dependence has the same effect. At the high value for E_2 of +200 mV the results appear to show no trends, but by the time the value for E_2 has dropped to −50 mV and lower the same features are being seen at the different rotation rates. The currents being achieved are just increasing. Figure 4.6 shows the rotation dependence of a 5 mM Hg^{2+} solution at an E_2 value of −250 mV. The steady state current is increasing with rotation rate as is the peak height and the well in the initial dip.

4.4 Microelectrode work

4.4.1 *Mechanically-cleaned MEs*

A series of CA experiments were undertaken using a ME. The following experimental data was collected using a subset of the conditions for the RDE, a 20.0 mM Hg^{2+}, E_1= +550 mV, E_2= +100 mV, on mechanically cleaned electrode unless otherwise stated. Data was collected over a 32 sec time frame. During this series of experiments three distinct groups of observations were made.

The first group of observations fall into a category which relates to the randomness of the onset of reduction after which from that point the growth smooth curves develop. Examples of this type of growth can be seen in Fig 4.7 where a selection of these types of growth curves are shown. It can be seen that there is no pattern for the commencement of reduction. Sometimes the time delay is short and in the range of 2000-4000 msec, at other times longer delays of up to 16000 msec are evident. In all of these transients once reduction commences there is a steep increase in the current being achieved but then after 200-500 msec, the slopes of these curves decrease and there is a steady but slower increase in the rate of reduction.

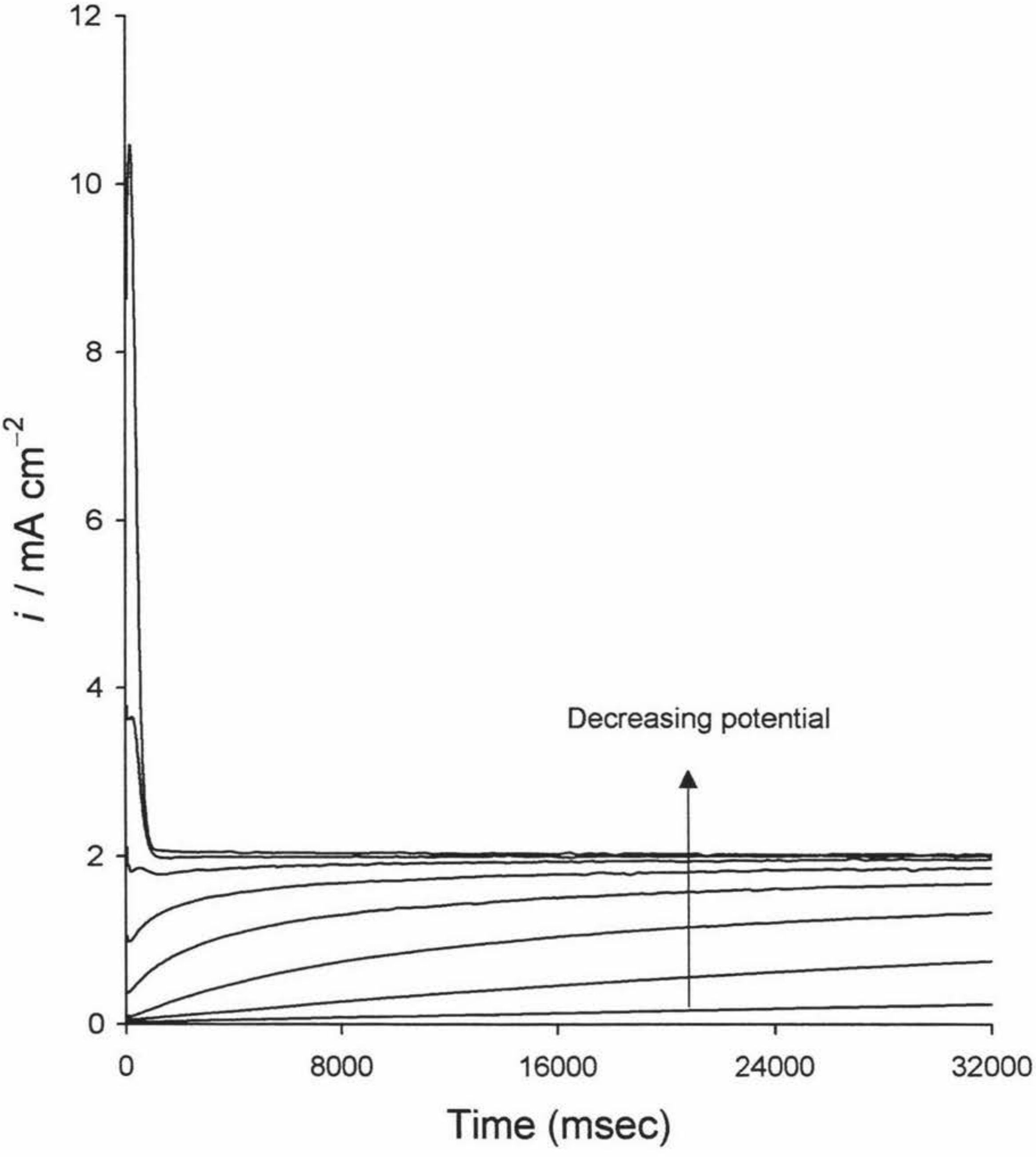

Fig 4.2 A series of transients with varying E_2 potentials of 200, 100, 0, –100, –200, –300, –400, and –500 mV. $[Hg^{2+}] = 2.0$ mM, $E_1 = 550$ mV, ω = 4000 rpm.

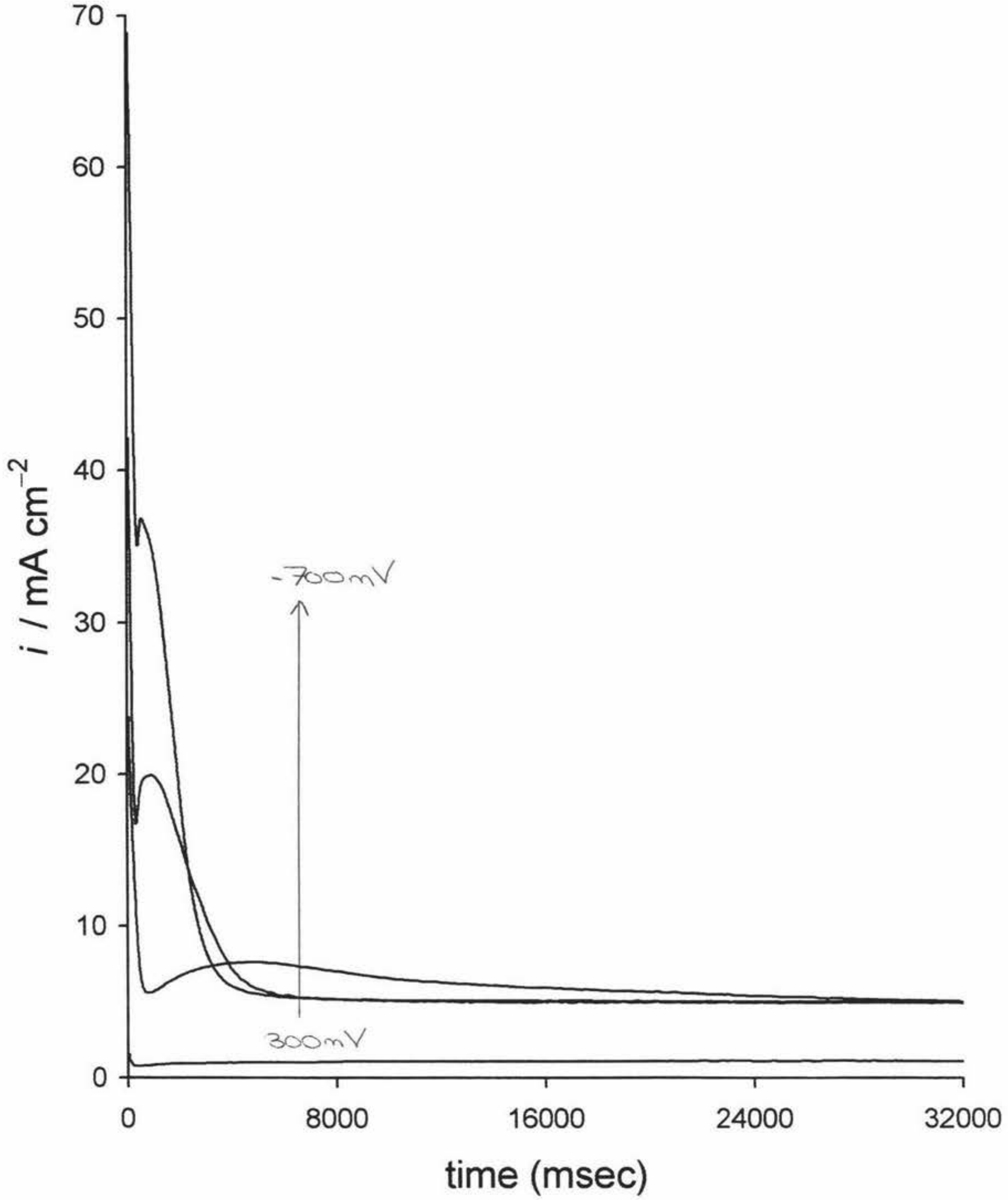

Fig 4.3 A series of transients with varying E_2 potentials of 300, –200, –450, and –700 mV. [Hg^{2+}] = 5.0 mM, E_1 = 550 mV, ω = 1000 rpm.

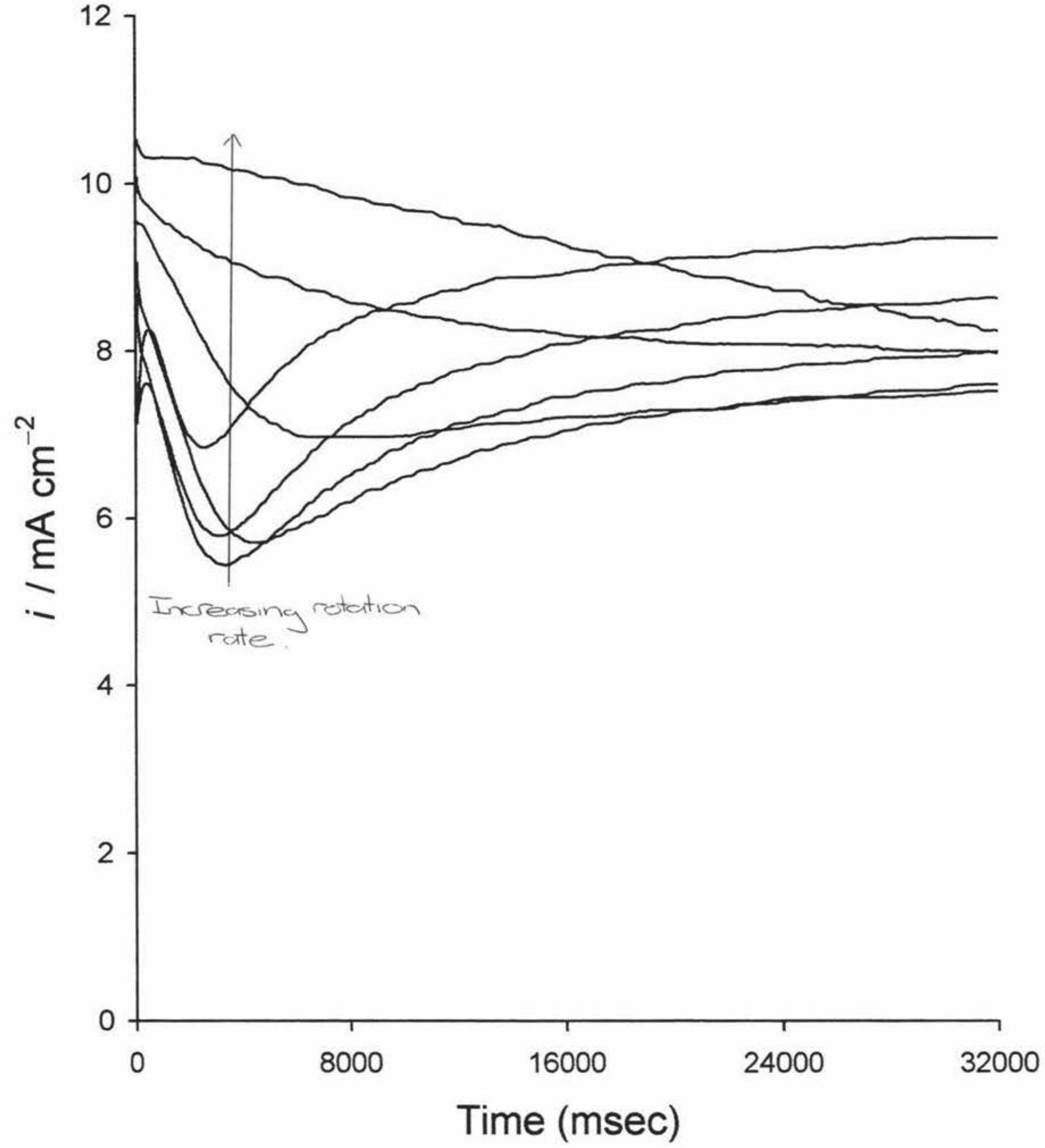

Fig 4.4 A series of transients for varying ω of 630, 1000, 1585, 2500, 4000, 6300, and 10000 rpm. [Hg^{2+}] = 10.0 mM, E_1 = +550 mV, E_2 = +200 mV.

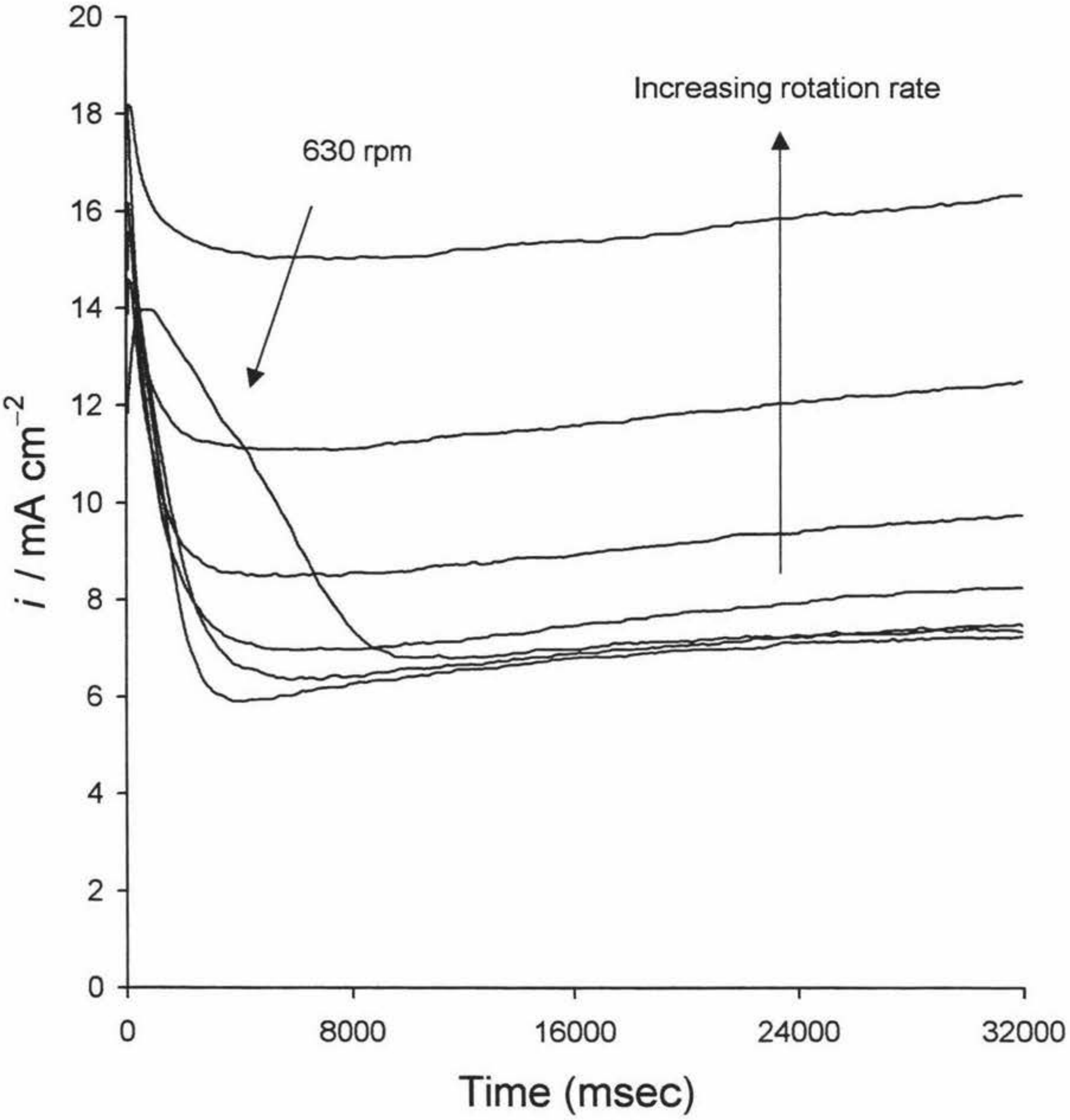

Fig 4.5 A series of transients for varying ω of 630, 1000, 1585, 2500, 4000, 6300, and 10000 rpm. [Hg^{2+}] = 10.0 mM, E_1 = +550 mV, E_2 = −50 mV.

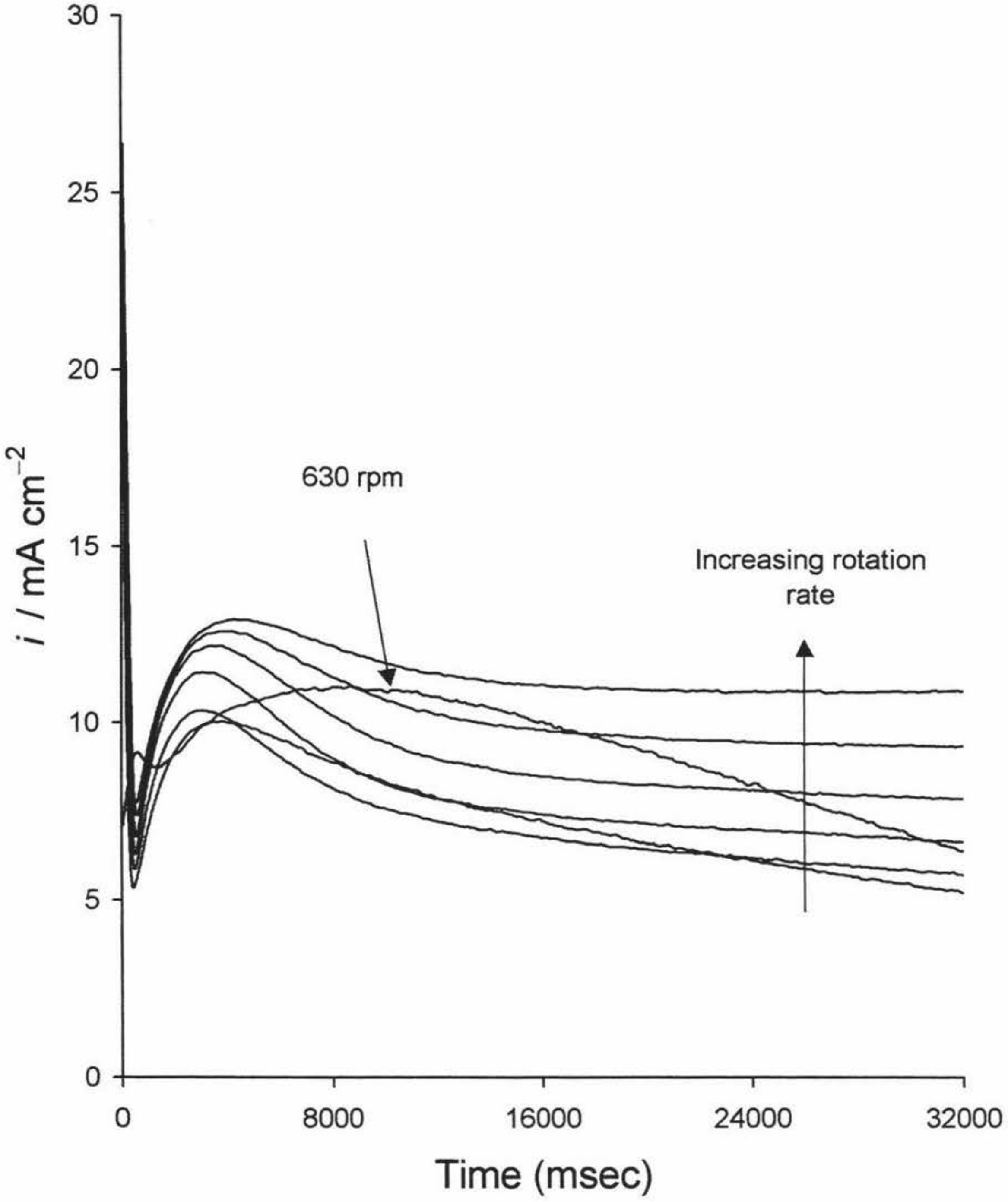

Fig 4.6 A series of transients for varying ω of 630, 1000, 1585, 2500, 4000, 6300, and 10000 rpm. [Hg^{2+}] = 5.0 mM, E_1 = +550 mV, E_2 = −250 mV.

The random time delays seen here are suggestive of random nucleation and growth of mercury deposits on the electrode, presumably as droplets. The absence of random delays on RDEs indicates that if this is the case, the distance between nuclei sites is likely to be of the same order as the distance of the microelectrode.

The second group of encountered events can be seen in Fig 4.8. Here, the random time delay for the onset of reduction are still evident, and the growth of smooth curves are still found. However, in these cases the smooth curves exhibit noticeable 'dislocation' increases in current. This is interpreted as being due to the overlap of two successive nuclei forming on the ME with different time delays. This group is distinct from those demonstrated in Fig 4.7 on the basis of the higher overall rate of reduction of deposited mercury on the electrode surface.

The third group of events occurring on the GC MEs that can be identified are the instances where time delays occur, as with the growth of the smooth current-time curves, but at some random point, sharp vertical drops in current take place. This may occur in one of three ways. The first is a drop in current all the way to zero and the second is that of smaller vertical drops in current with the continuance of the growth curve. The last is when the growth of a second nuclei starts but stops 1-2 seconds into its growth and the current drops to that of what appears to be the continuation of the first nuclei. Examples of these first two types of events can be seen in Fig 4.9, with third event seen in Fig 4.10.

The curve where there is a total drop in current back down to zero current could be due to a flipping event of the hemispherical mercury droplet to a spherical mercury droplet. When this event occurs then there could be a loss of contact between the droplet and the electrode surface, causing the complete loss of current. When this occurs there seems to always be another time delay before the growth of a new mercury droplet is seen.

The instances where there is a small or major drop in current but not all the way back to zero may also fit with the theory of droplet flipping, from hemispherical to spherical shape, but without the loss of the new droplet from the electrode surface. If volume is maintained the following equation applies

$$r_{\mathrm{s}} = \left(\frac{1}{2}\right)^{1/3} r_{\mathrm{h}} \tag{4.4}$$

where r_s and r_h are the radii of a sphere and hemisphere respectively.
The ratio of the area of a sphere to that of a hemisphere then gives

$$\frac{A_s}{A_h} = \frac{1}{0.5^{2/3}} \tag{4.5}$$

If the flipping of a hemisphere to a sphere occurs and is still attached to the electrode the current should decrease as the current is proportional to area, as the area of a sphere is smaller than that of a hemisphere. Another possibility which could explain the event where there is a drop in current but not all the way down to zero current, maybe the merging of two of more hemispherical droplets which started to grow at the same time, forming one larger hemispherical droplet. If this were the case then when the droplets formed one there would be a decrease in the surface area where reduction takes place. This would cause a decrease in current and the current-time curve would continue to increase as reduction is still occurring on the surface of a larger hemispherical droplet. As it can also be seen in Fig 4.9 these current drops are not only occurring once or twice in the 32 second time scale of one of the CA experiments, they sometimes occur more.

The last observation of these types of current decrease could be due to the merging of two droplets again but this time one of the droplets has started to form after the first is established. The smaller of the two could be consumed by that of the much larger, first droplet and therefore not effecting the volume of the larger one greatly.

4.4.2 *Potential dependence*

Figure 4.11 shows a selection of transients that have E_2 potentials more cathodic than 0 mV. The loss of any similarity to the transients seen before in this ME section in this Fig 4.11 would suggest that there is a potential dependence on whether or not these transient will develop or not.

4.4.3 *Electrochemically cleaned ME CA experiments*

Figure 4.12 shows a selection of transients for cases where the ME has first been mechanically cleaned then after the first run the ME was then electrochemically cleaned.

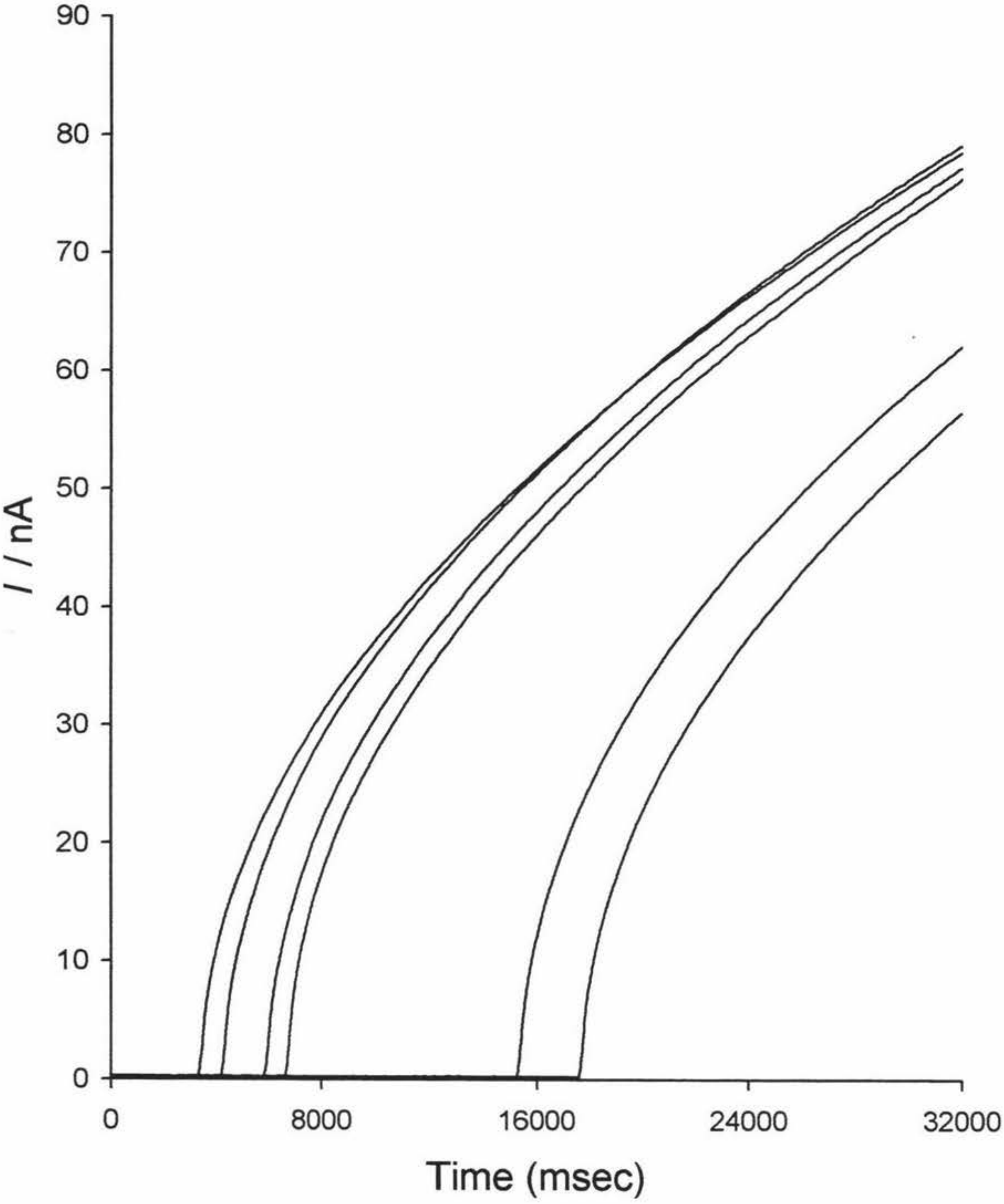

Fig 4.7 A series of single smooth growth transients on MEs. [Hg^{2+}] = 20.0 mM, E_1 = +550 mM, E_2 = +100 mM.

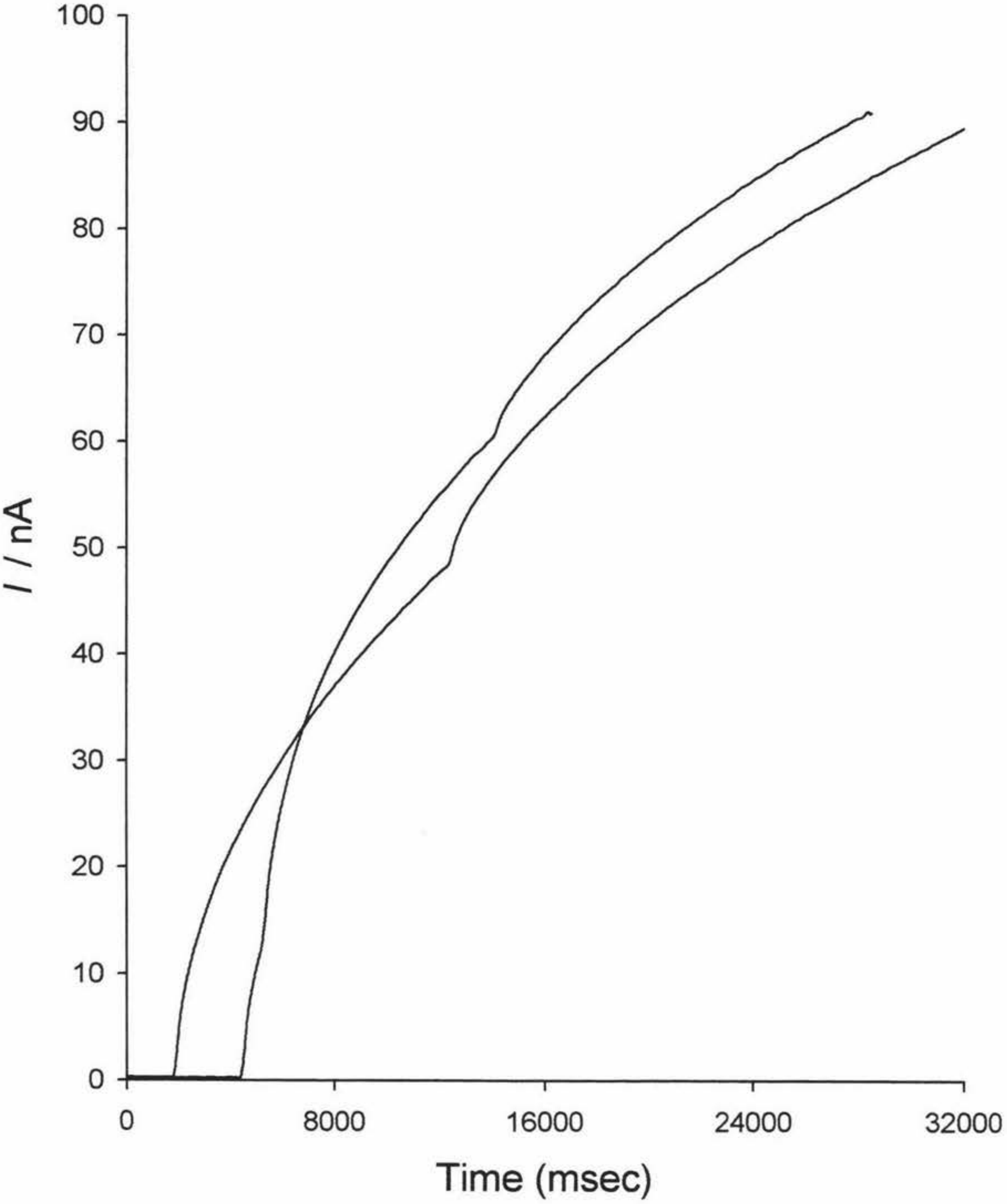

Fig 4.8 A selection of growth transients exhibiting more than one signal smooth growth pattern within a transient on MEs. $[Hg^{2+}]$ = 20.0 mM, E_1 = +550 mM, E_2 = +100 mM.

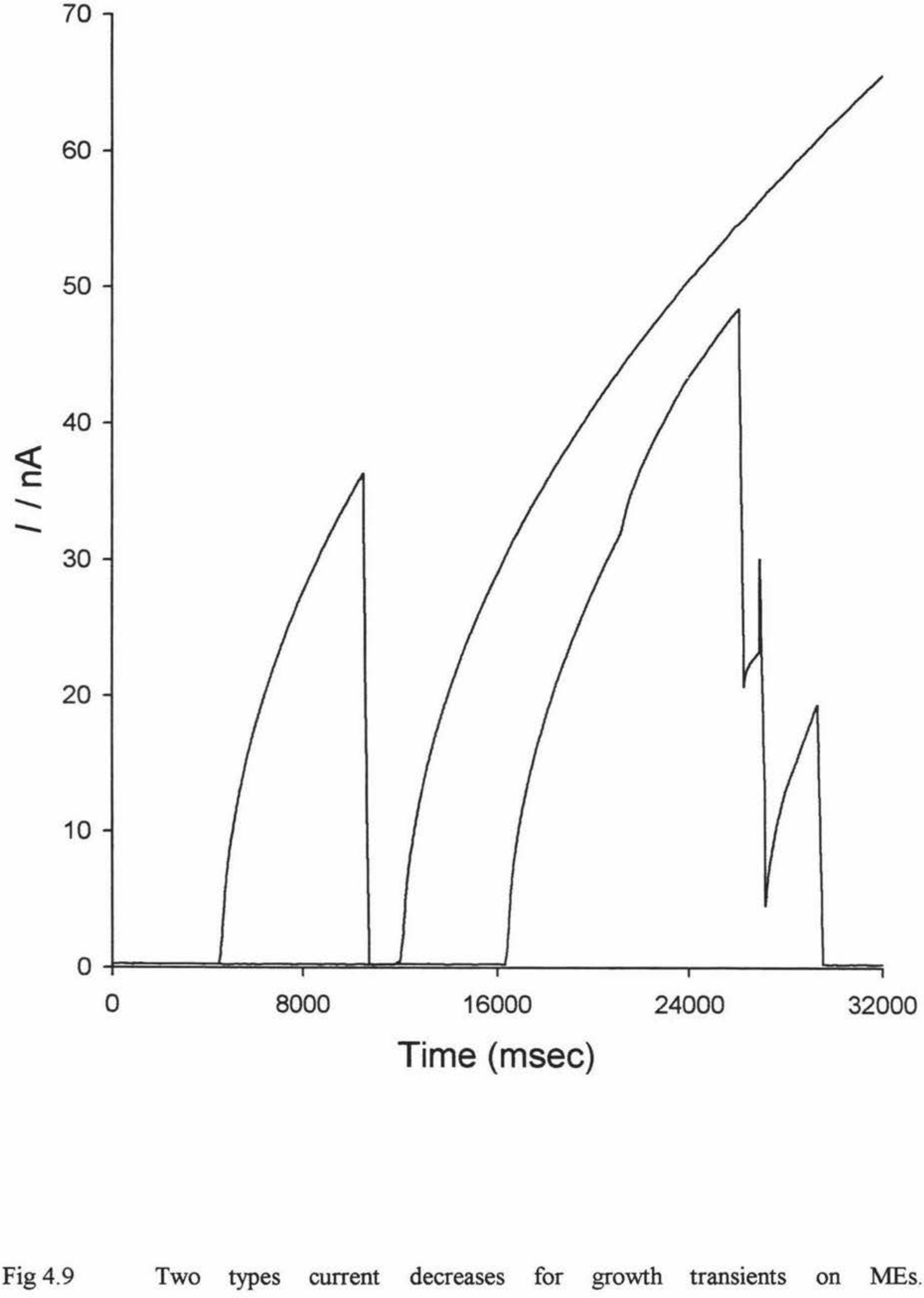

Fig 4.9 Two types current decreases for growth transients on MEs. $[Hg^{2+}]$ = 20.0 mM, E_1 = +550 mM, E_2 = +100 mM.

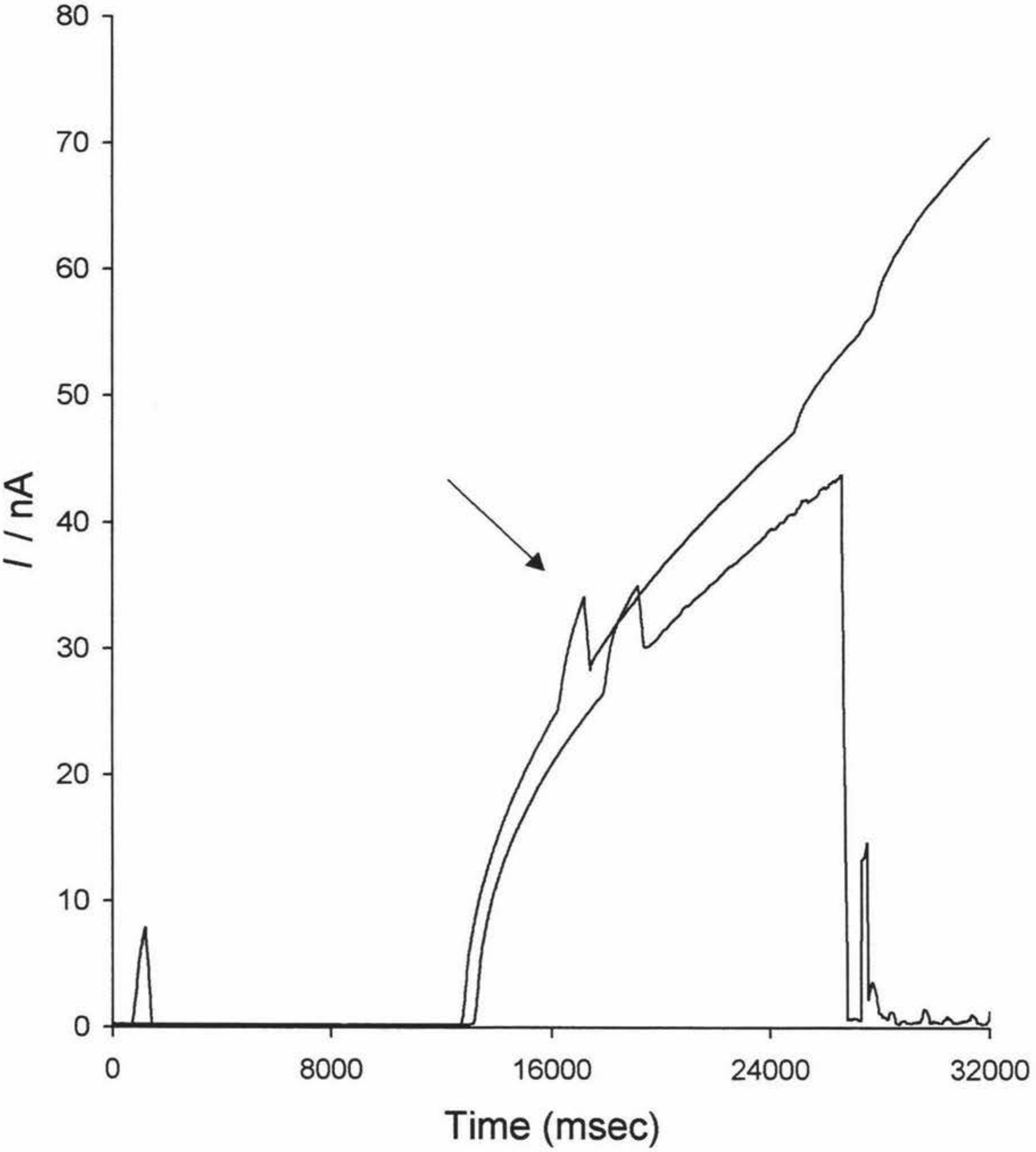

Fig 4.10 A third type of current decreases for transients on MEs. $[Hg^{2+}]$ = 20.0 mM, E_1 = +550 mM, E_2 = +100 mM.

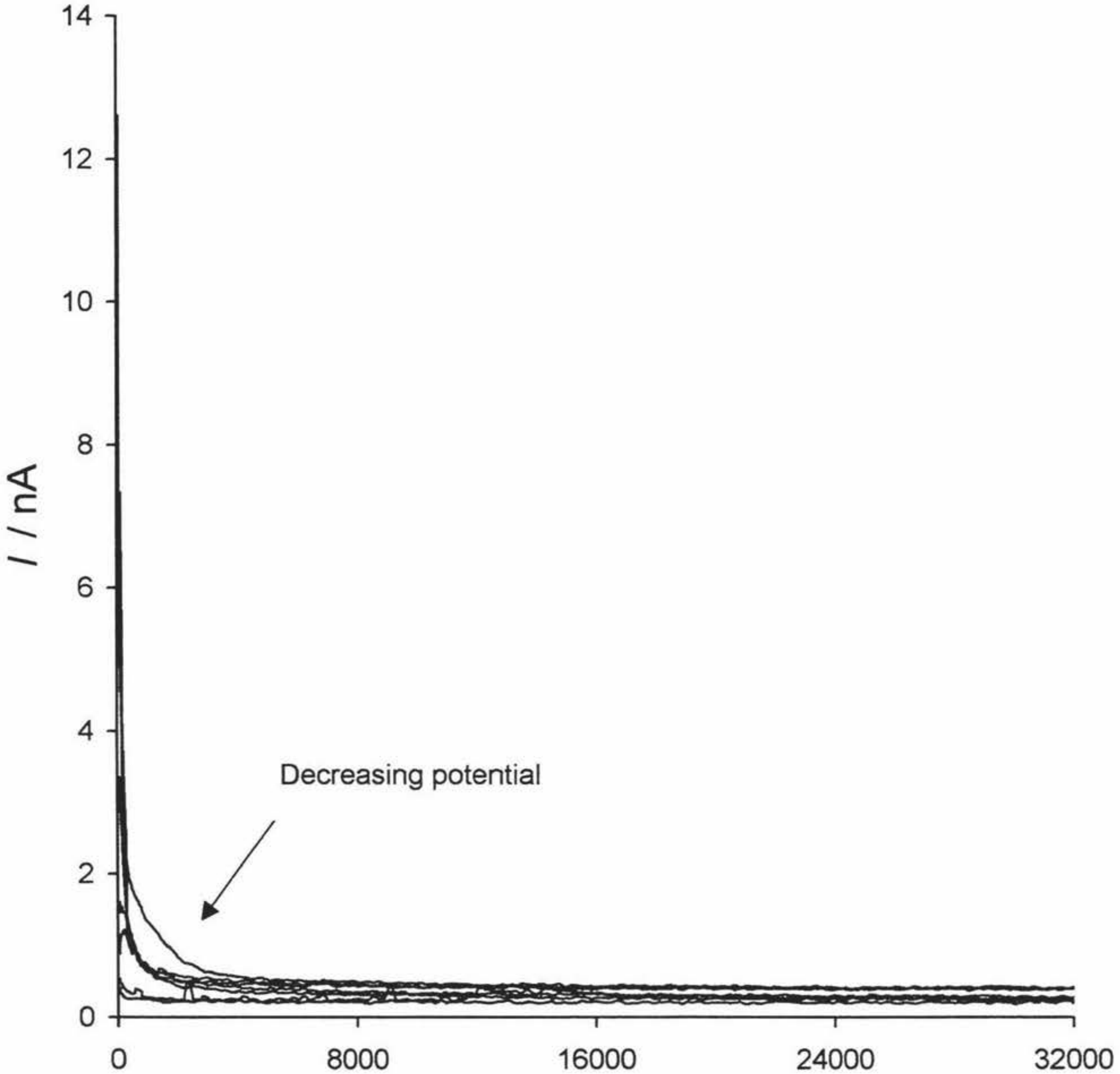

Fig 4.11 A selection of growth transients on MEs with varying E_2 potentials of 0, −200, −400, −600, −800, −1000, and −1200 mV. $[Hg^{2+}]$ = 20.0 mM, E_1 = +550 mM.

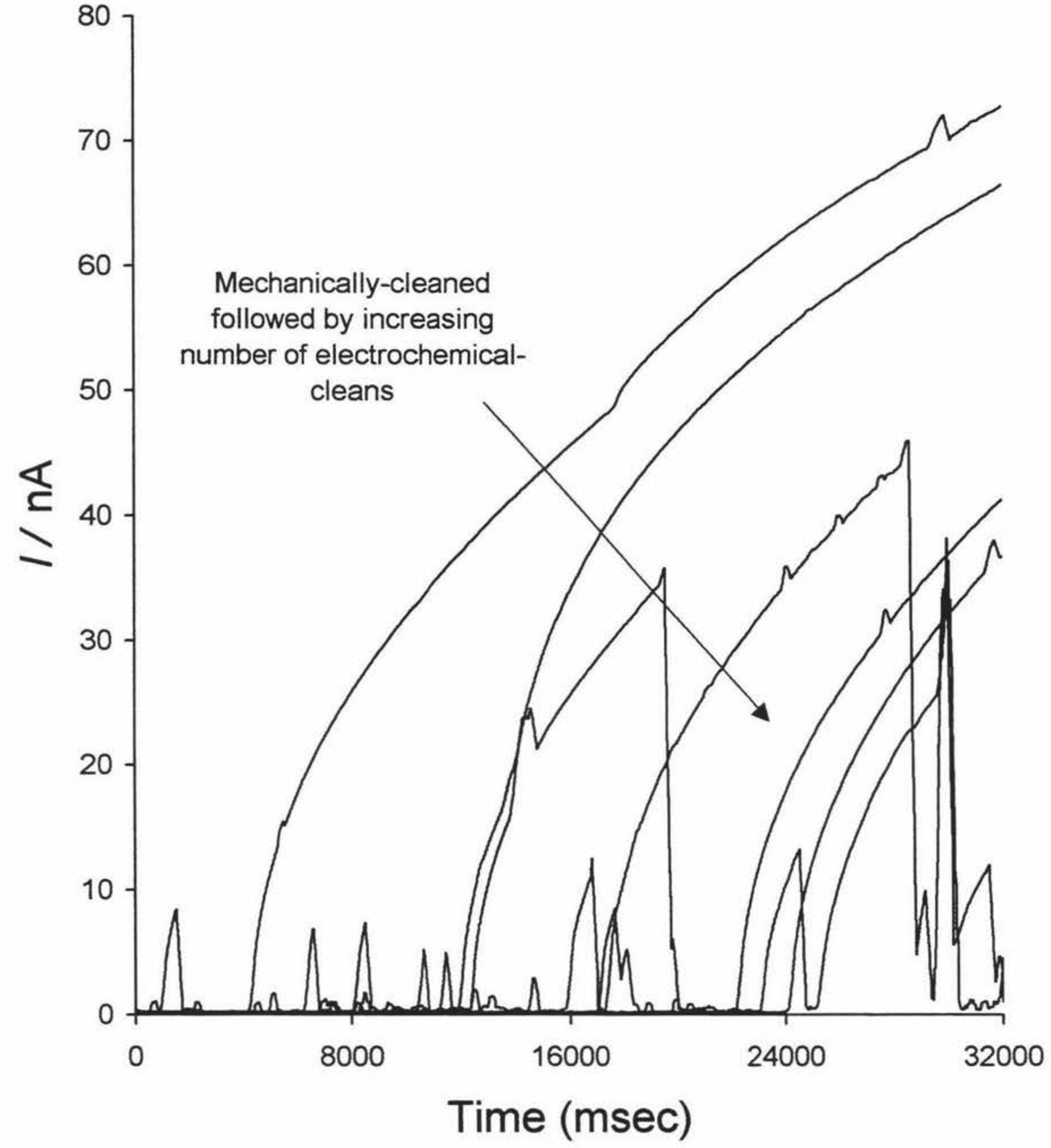

Fig 4.12 A selection of growth transients on MEs, first mechanically-cleaned then subsequently undergone electrochemical-cleaning of +1500 mV for 30 sec. $[Hg^{2+}] = 20.0$ mM, $E_1 = +550$ mM, $E_2 = +100$ mM.

The electrochemical cleaning was undertaken at the potentials of +1500 mV. All electrochemical cleaning cycles were carried out for 30 seconds unless stated. The response recorded when electrochemical cleaning had been undertaken between cycles, instead of mechanical cleaning, show a much different response from cycle to cycle. All the other parameters and conditions were kept constant, the only difference was that of mechanical cleaning against electrochemical cleaning.

When the electrode is electrochemically cleaned at 1500 mV for 30 seconds between experiments there is a progressive change in transient from experiment to experiment. The maximum current reached by each experiment decreases as the number of electrochemical-cleaning cycles increases. After 4 of 5 electrochemical-cleaning cycles the transients comprise of only a number of small peaks with rapid decreases in current to zero. These are quite distinct from the selection of mechanically-cleaned MEs seen in Fig 4.7. Here greater currents were reached after the mechanical-cleaned transient than any other transient shown. By the end of these six experiments the results was many small reduction peaks with the sharp drop down to zero current, varying time delays, and then more small reduction peaks.

4.5 CA experiments in nitrate compared to those in acetate

The nitrate experiments were mostly run over the time frame of 5000 msec due to the fact that the main features were completed by the end of this time frame, so most of the comparisons with acetate will be over that time scale for reasons of comparison.

Figure 4.13 shows the successive CA runs of a 5 mM Hg^{2+} solution in nitrate. The value of E_2 was slowly decreased in steps of 25 mV from 300 mV down to 100 mV. By the time the E_2 value was decreased to 250 mV a steady state current had been reached by the end of the 5000 msec time frame. At the E_2 potential of 175 mV the first signs of the formation of a peak can be seen. As the E_2 potential is reduced even further the size of the peak increases and its formation occurs at quicker times.

Figure 4.14 shows 4 CA runs, 3 of which are in an acetate buffer, and the other one is in a nitrate solution. The 3 runs in the acetate buffer cover the E_2 values of +100, −200, and −400 mV, and the nitrate run is at the E_2 potential of +100 mV. In Fig 4.14 the run which has the formation of a small peak within the first 500 msec is the run for the nitrate solution at the E_2 value of +100 mV. The run below that is that of the acetate buffer solution at an E_2 value of +100 mV as well. The response in nitrate compared to that of acetate is very different. By the time the E_2 value has decreased to +100 mV in nitrate solutions, a constant response has been achieved. The very fast, steep drop in current in the nitrate solutions before the formation of the small peak is probably due to capacitance charging. The nitrate solutions are quickly reaching a steady state current at much higher E_2 values and at much faster times, than the acetate solution do. In Fig 4.14 it can be seen that even when the value of E_2 is reduced down to –400 mV a steady state current has not been achieved by the end of the 5000 msec time frame.

Figures 4.15 and 4.16 compare the difference between nitrate and acetate again, but these two figures have the runs for both nitrate and acetate at +300 and +100 mV respectively. Fig 4.15, with the E_2 value of +300 mV, has a time scale that extents to 32 sec and here it can be seen that the acetate run is very slowly increasing towards, hopefully, a steady state current. The nitrate run in the same figure hasn't reached a steady state current by the end of the 32 sec run but it is not that far from reaching it. Fig 4.16 is again comparing the differences between nitrate and acetate, this time at the lower E_2 value of +100 mV. The acetate run hasn't achieved a steady state current here but the rate at which it is increasing is much faster than it was for the +300 mV run. The time frame here is also only 5000 msec. In the nitrate solution, by the end of 1000 msec it has reached a steady state current.

It appears from these results that the reactions that are occurring in the nitrate solutions are occurring much faster than the reaction that are occurring in acetate solution, but at the same time it appears that the reactions in acetate are more complex than those in nitrate solutions.

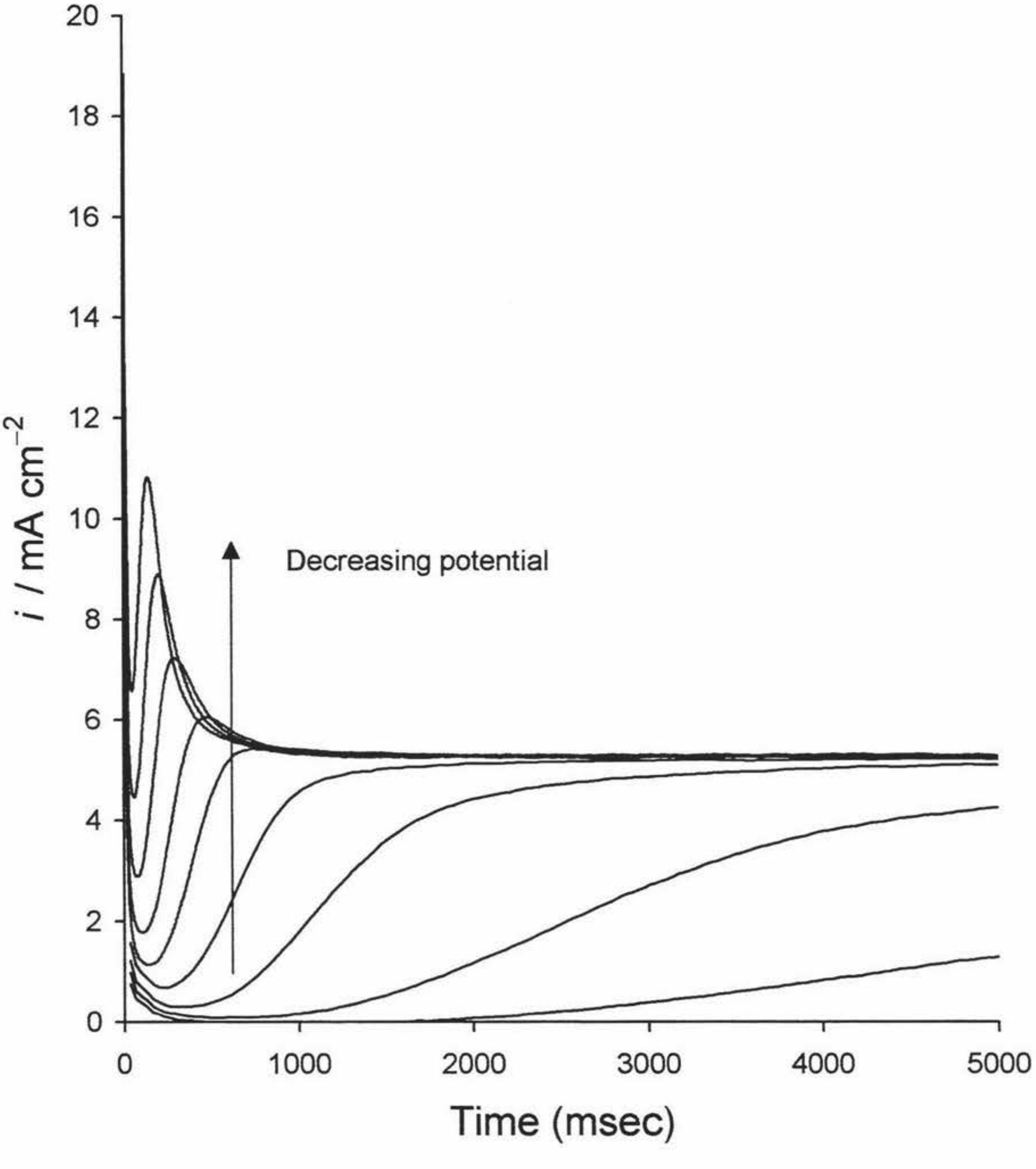

Fig 4.13 A series of transients with varying E_2 potentials of 300, 275, 250, 225, 200, 150, 125, and 100 mV. [Hg^{2+}] = 2.0 mM, E_1 = +550 mM, ω = 1000 rpm.

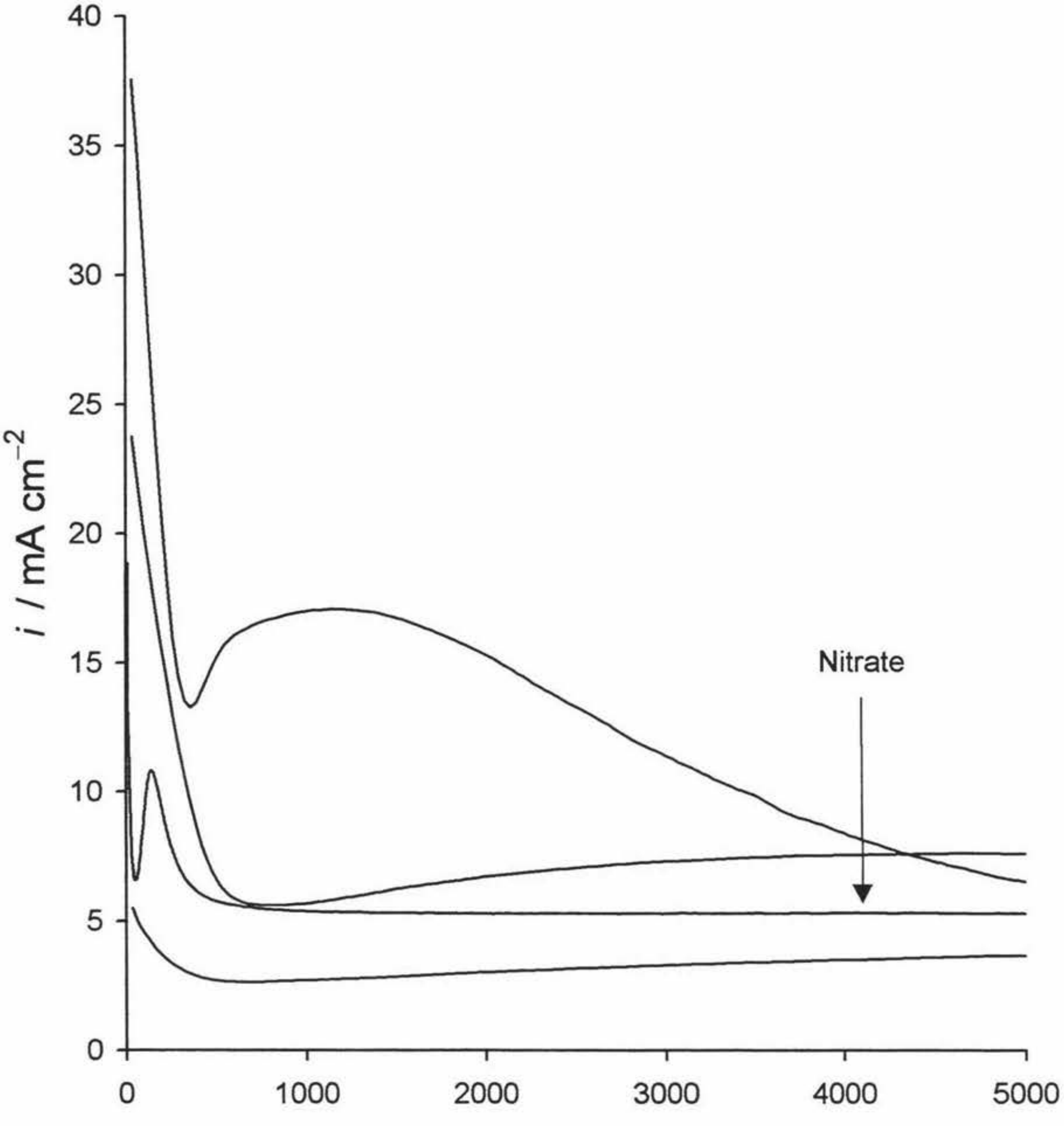

Fig 4.14 A series of four transients, three of which are in an acetate buffer and one in a nitrate buffer. E_2 potentials for acetate transients are +100, –200, and –400 mM, and E_2 = +100 mV in nitrate. [Hg^{2+}] = 5.0 mM, E_1 = +550 mM, ω = 1000 rpm.

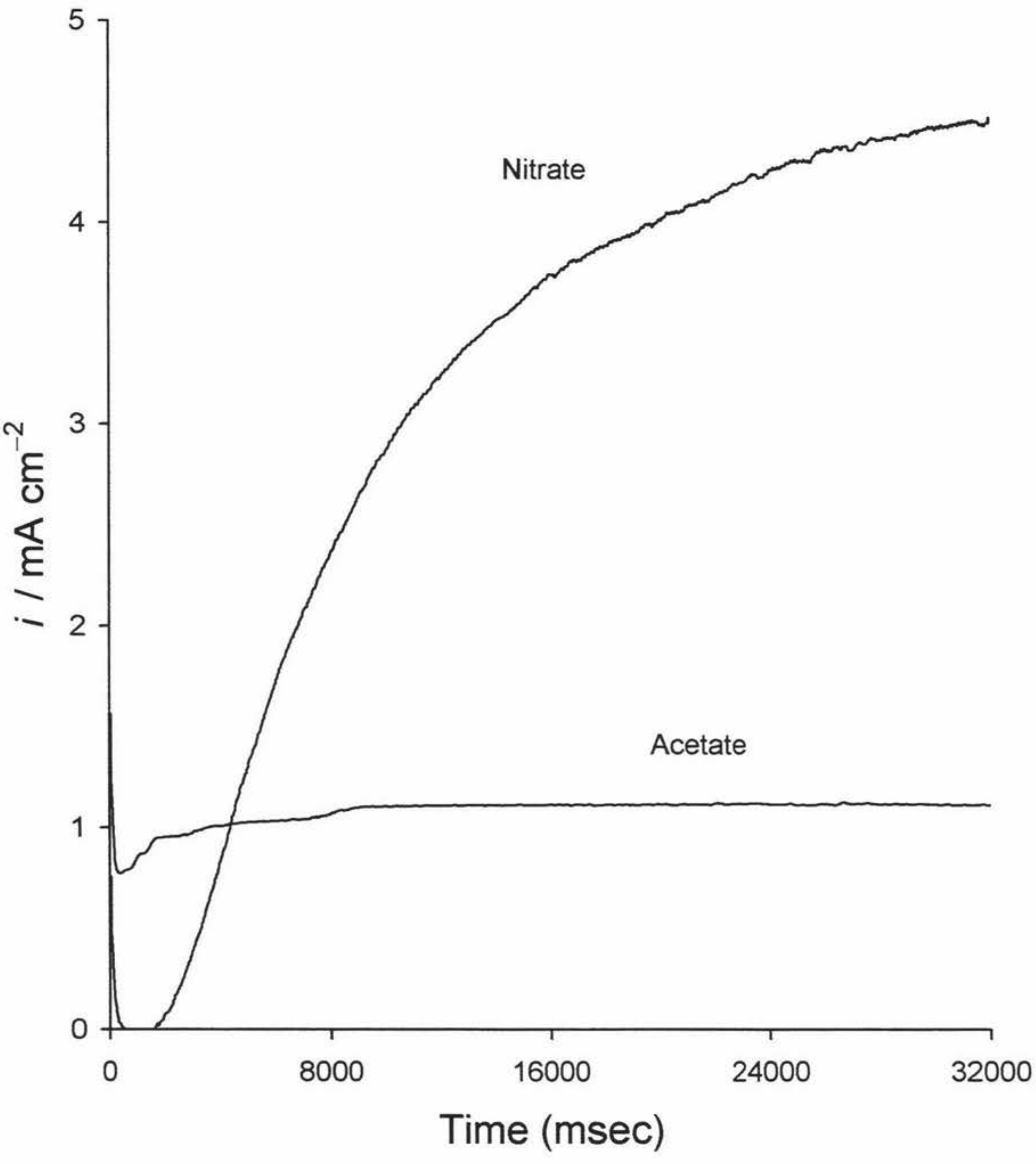

Fig 4.15 A comparison between transients in acetate and nitrate. [Hg^{2+}] = 5.0 mM, E_1 = +550 mM, E_2 = +300 mM, ω = 1000 rpm.

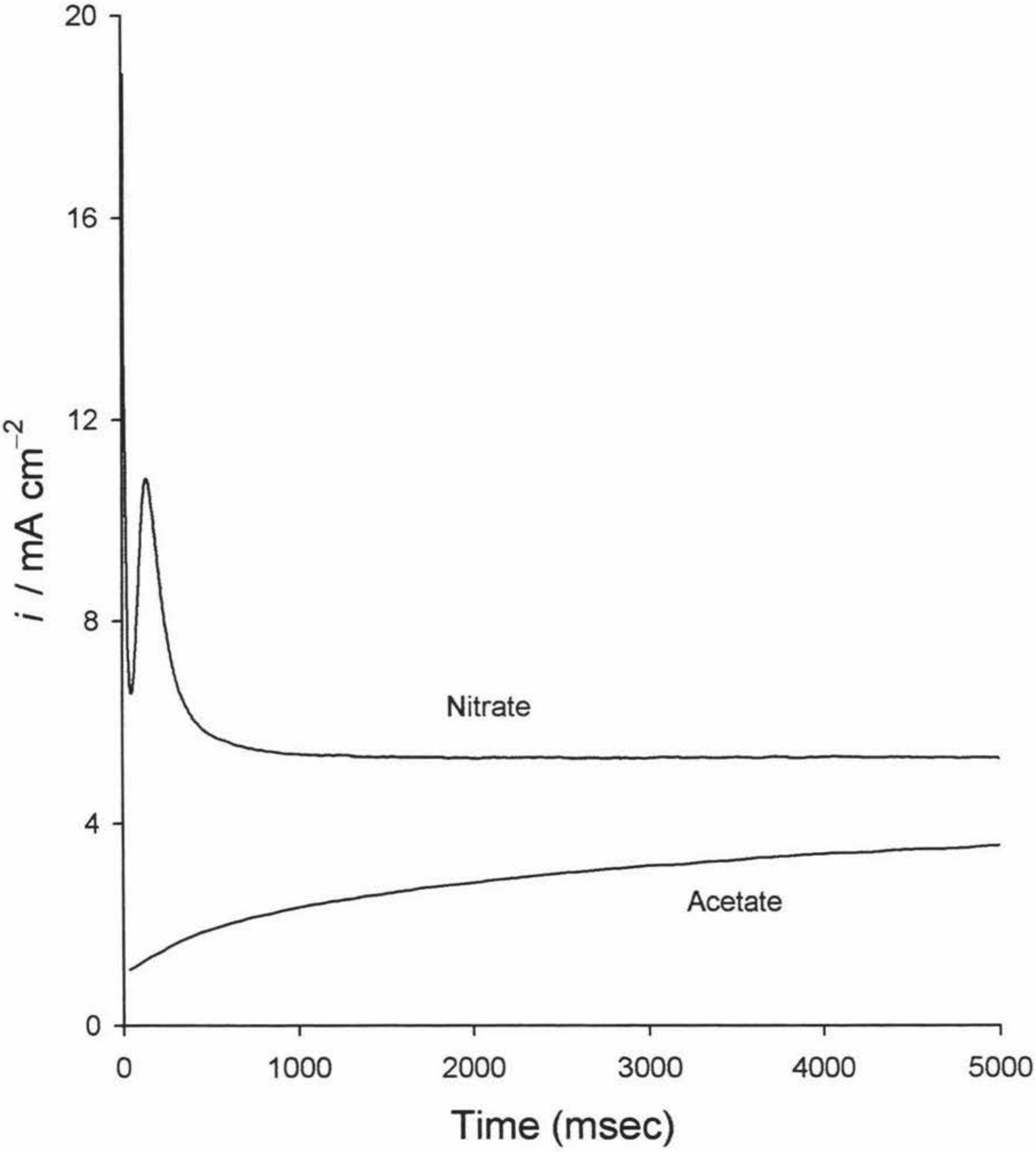

Fig 4.16 A comparison between transients in acetate and nitrate. [Hg^{2+}] = 5.0 mM, E_1 = +550 mM, E_2 = +100 mM, ω = 1000 rpm.

CHAPTER 5

Discussion

5.1 Introduction

The focus of this chapter is to analyse and discuss the features observed during CV and CA experiments which have been identified Chapters 3 and 4. Once all the observations have been accounted for a comprehensive all-encompassing mechanism will be proposed for the deposition of mercury on GC RDE.

5.2 Observations from cyclic voltammetry and chronoamperometry

In this section all the observations from Chapters 3 and 4 will be briefly reiterated. All observations predominately concern those experiments performed in acetate unless otherwise stated. Periodically comparisons are made with nitrate experiments.

5.2.1 *C1 and C2 peaks*

The features C1 and C2 both changed in response with differing experimental conditions. In the scan rate dependence experiments it was established that C1 and C2 only completed formation by the end of the cathodic sweep at the lowest scan rate of 20 mV s^{-1} for 10.0 and 5.0 mM Hg^{2+} (Figures 3.9 and 3.10 respectively). At these concentrations C1 and C2 completed formation at all electrode rotation rates (Figures 3.16 and 3.17).

With varying rotation rates there was no strong evidence for C1 or C2 forming at 2.0 mM Hg^{2+} (Figure 3.18). However at the highest scan rates, and the most cathodic limits there were indications of C1 forming (Figure 3.11).

Similar observations were made concerning C1 and C2 for 1.0 and 0.5 mM Hg^{2+} (Figures 3.12 and 3.19 and Figures 3.14 and 3.20 respectively).

The peaks C1 and C2 decreased with increasing time left at open potential between a series of CV experiments without intervening cleaning - either electrochemical or mechanical (Figure 3.23). The voltammograms return to profiles that resemble voltammograms produced after the electrode has undergone mechanical-cleaning. C1 and C2 decrease at a much more rapid rate with either increased potential for the electrochemical-cleaning and/or the length of time for which the cleaning process lasts.

The peaks C1 and C2 are never observed when working in nitrate electrolyte (Figures 3.25, 3.27, and 3.28).

5.2.2 *Current spikes*

The current spikes were another feature observed in this work, particularly at the higher Hg^{2+} concentrations. With 10.0 mM Hg^{2+} no current spikes were seen at the scan rates of 20 and 50 mV s^{-1}, were seen at 100 and 200 mV s^{-1}, and then above 200 mV s^{-1} where C2 had not formed, the current spikes where not seen (Figure 3.9). In rotation rate dependence experiments in 10.0 mM Hg^{2+}, current spikes were only observed at rotation rates of 2500 rpm and below (Figure 3.16).

Current spikes were observed at 200, 500, and 1000 mV s^{-1} with 5.0 mM Hg^{2+} and in all of these cases more than 50 % of C2 had formed by the end of the forward sweep (Figure 3.10).

No current spikes were ever observed in the scan rate dependence experiments of 2.0, 1.0, or 0.5 mM Hg^{2+} (Figures 3.11, 3.12 and 3.14 respectively).

Concentrations lower than 10.0 mM Hg^{2+} in the rotation rate dependence experiments showed no signs of producing current spikes.

No current spikes were observed in any of the work carried out in nitrate.

5.2.3 *Overpotential shift*

Major shifts in E_{red} are observed for both 10.0 and 5.0 mM Hg^{2+} in both the scan rate and rotation rate dependence experiments (Figures 3.9 and 3.16 and Figures 3.10 and 3.17 respectively).

A random occurrence for E_{red} occurs with scan rate for 2.0 mM Hg^{2+} (Figure 3.11) but is constant, although not as anodic, as E_{red} for 10.0 and 5.0 mM Hg^{2+} with rotation rate dependence (Figure 3.18).

No shift in E_{red} was observed for 1.0 and 0.5 mM Hg^{2+} either under scan rate, or rotation rate dependence (Figures 3.12 and 3.19 and Figures 3.14 and 3.20 respectively).

When the nitrate experiments were undertaken, no shift in E_{red} was ever observed

(Figures 3.26, 3.27 and 3.28).

5.2.4 *Peak A1*

The anodic peak A1 in 10.0 mM Hg^{2+}only completed by the end of the cycle for the scan rates 20 and 50 mV s^{-1} (Figure 3.9), compared to 20, 50, and 100 mV s^{-1} in 5.0 mM Hg^{2+} (Figure 3.10). A1 increases with increasing rotation rate for both 10.0 and 5.0 mM Hg^{2+} (Figures 3.16 and 3.17 respectively).

A1 was fully formed for all scan rates in 2.0 mM Hg^{2+} (Figure 3.11). A shoulder in A1 was observed and the peak was also found to decrease with increasing scan rate at this concentration. A1 was also found to decrease with increasing scan rate in the cases of 1.0 and 0.5 mM Hg^{2+} (Figures 3.12 and 3.14 respectively). All A1 peaks over these last three concentrations were fully formed by the end of the cycle.

Over the entire concentration range A1 was found to increase with increasing rotation rate in all cases (Figures 3.16 to 3.20)

With rotation rate dependence in nitrate it was found that A1 increased with rotation rate up until 2500 rpm, then above this rotation rate A1 was found to decrease as rotation increased so that at 10000 rpm A1 had a peak height 60 % of that at 2500 rpm (Figure 3.27).

5.2.5 *Peaks A2 and A3*

The A2 peak was not seen at concentrations of 10.0, 5.0, and 2.0 mM Hg^{2+} in scan rate or rotation rate dependence experiments. A2 was observed with 1.0 and 0.5 mM Hg^{2+}, decreases with increasing scan rate and was found to shift to more anodic potentials (Figures 3.12 and 3.14 respectively).

The peak A3 was only found once in all of the experiments undertaken in this work and was for the lowest concentration, 0.5 mM Hg^{2+}, and the lowest scan rate, 20 mV s^{-1} in the scan rate dependence experiments (Figure 3.15).

With rotation rate dependence, A2 was observed to increase with increasing rotation and similarly the scan rate dependence, shift to more anodic potentials with 1.0 and 0.5 mM Hg^{2+} (Figures 3.19 and 3.20 and Figures 3.13 and 3.15 respectively).

A2 and A3 were never observed when working in nitrate.

5.2.6 *Steady state*

The steady state current was attained for all scan rates except 500 and 1000 mV s^{-1} with 2.0 mM Hg^{2+} (Figure 3.11). With 1.0 mM Hg^{2+} a steady state current was attained over all scan rates as with 0.5 mM (Figures 3.12 and 3.14 respectively). A steady state current was attained over the entire rotation rate range for 10.0, 5.0, 2.0, and 1.0 mM Hg^{2+} (Figures 3.16 to 3.19). At 0.5 mM Hg^{2+} a steady state current was also attained over all rotation rates but on the reverse sweep (Figure 3.20).

In the case of nitrate a steady state current was obtained in all experiments but on the reverse sweep. There is also a reproducible and constant 'dip' in the steady state current on the reverse sweep in this nitrate work (Figures 3.27 and 3.28).

5.2.7 *CA observations*

The main features from the CA experiments arise from the ME work. The range of growth transients were found and investigated. These growth transients include those for single transients (Figure 4.7), those with more than one growth curve in one transient (Figure 4.8), and three different types of transients that involve rapid decreases in current (Figures 4.9 and 4.10). The dependence on the value of the E_2 potential and the effect of electrochemical-cleaning on the transients was also investigated (Figures 4.11 and 4.12 respectively).

5.3 Scan rate

The scan rate dependence experiments suggest some overall characteristics of the reaction. In a typical voltammogram, there will be several peaks, and by observing how these appear and/or disappear as the scan rate is varied, and by noting the differences between the first cycle and the subsequent cycles, it may be possible to determine how the processes represented by the peaks are related [74]. As well as that from the scan rate dependence of the peak amplitudes, the role of adsorption, diffusion, and coupled homogeneous chemical reactions may be identified. Unlike when the reactant and product species are in solution or where there is only one solid product formed it becomes unclear as to whether or not the reaction is totally reversible or irreversible with out taking into account the entire potential range, both anodic and cathodic. The relationship between the peak current and scan rate generally should relate to i_{A1} vs. $v^{1/2}$ being linear for reversible reactions.

Fig 5.1 shows the i_{A1} *vs* $v^{1/2}$ plot for the results of this acetate work. No simple explanation can be given for these results but it can be said that it is clear that the reaction mechanism going on is not solely reversible or solely irreversible and from qualitative analysis no definite conclusions can be drawn.

5.4 Levich Study

The Levich model is the simplest mode involving mass-transport [75]. For situations where the surface concentration of an electroactive species is zero due to mass-transport limitations, the relationship between the limiting current density and the rotation rate is given by the Levich equation as was shown in Chapter 2.

$$i_L = 0.620nFD^{2/3}\omega^{1/2}\nu^{-1/6}c_b \tag{2.4}$$

Equation 2.4 indicates that the limiting current density is proportional to the bulk concentration, c_b, and is entirely mass transport controlled. A plot of i_L *vs* $\omega^{1/2}$ should be linear and pass through the origin. The slope a plot of i_L *vs* $\omega^{1/2}$ may be used to estimate the diffusion coefficient of the electroactive species.

5.5 Koutecky–Levich Study

The Koutecky-Levich model is a modification to the Levich that allows the overall rate to be controlled by a combination of mass–transport and electron-transfer processes. The current density at any potential in the region of mixed control is given by both mass transport and electron transfer kinetics. The current density of electron transfer is given by

$$i = nFk_f c_s \tag{5.1}$$

where k_f is the heterogeneous electron transfer rate constant, and c_s is the surface concentration. The incorporation of bulk concentration, c_b, and the Nernst diffusion layer layer, δ, yields

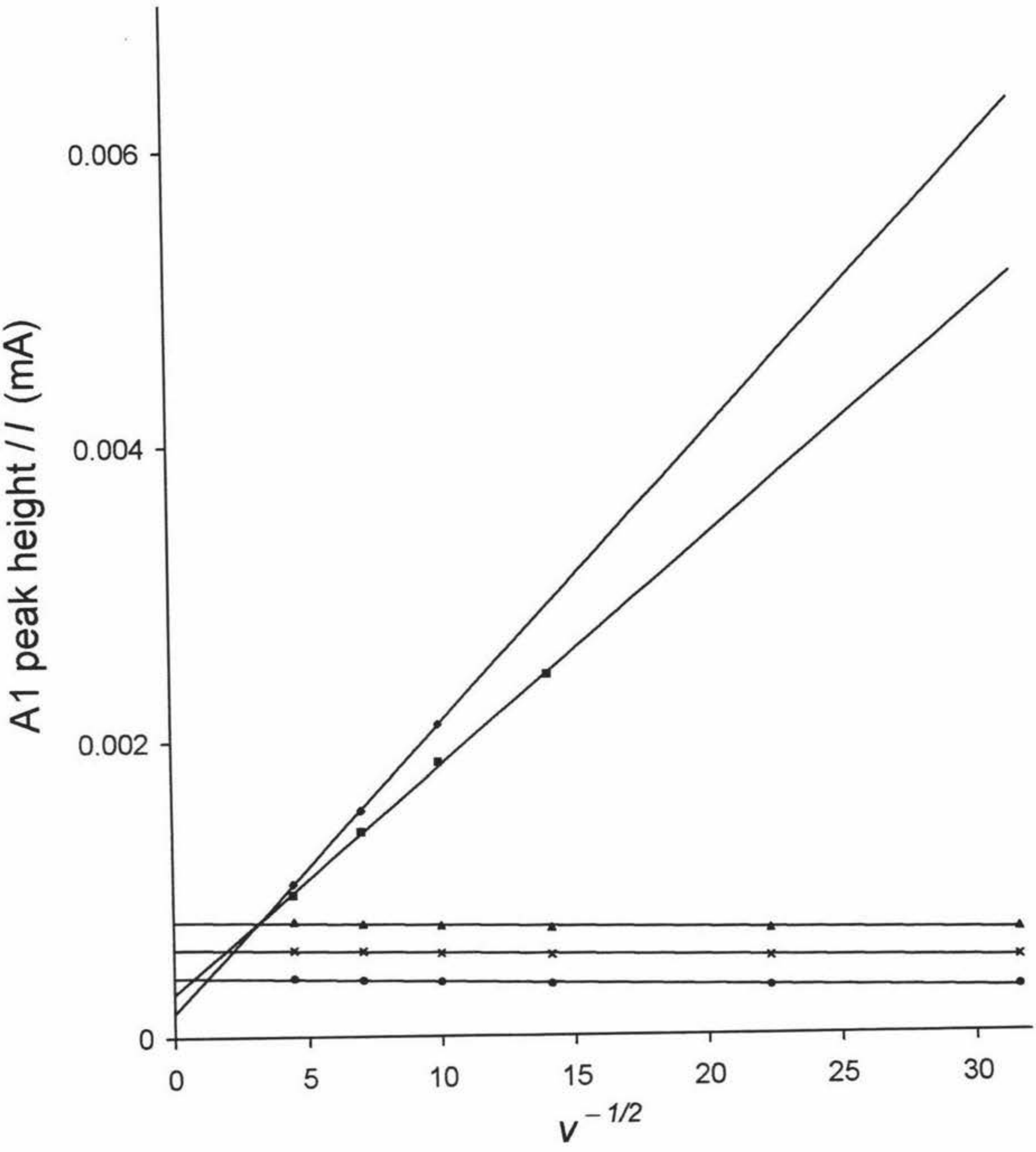

Fig 5.1 A1 peak heights plotted as a function of $\nu^{1/2}$. ◆ 10.0 mM, ■ 5.0 mM, ▲ 2.0 mM, × 1.0 mM, ● 0.5 mM.

$$i = \frac{nFD(c_{\mathrm{b}} - c_{\mathrm{s}})}{\delta} \tag{2.1}$$

Equating Eq. 5.1 and 2.1 and rearranging for c_s yields

$$c_{\mathrm{s}} = Dc_{\mathrm{b}} / k_{\mathrm{f}}\delta + D \tag{5.2}$$

Substituting Eq. 5.2 into 5.1 and inverting gives

$$\frac{1}{i} = \frac{\delta}{nFDc_{\mathrm{b}}} + \frac{1}{nFk_{\mathrm{f}}c_{\mathrm{b}}} \tag{5.3}$$

The diffusion layer thickness variation with rotation rate is given by Eq. 2.3

$$\delta = 1.61D^{1/3}\omega^{-1/2}\nu^{-1/6} \tag{2.3}$$

and substitution into 5.3 gives the Koutecky-Levich equation.

$$\frac{1}{i} = \frac{1}{nFk_{\mathrm{f}}c_{\mathrm{b}}} + \frac{1}{0.620nFD^{2/3}\nu^{-1/6}c_{\mathrm{b}}} \quad \frac{1}{\omega^{1/2}} \tag{5.4}$$

This permits a graphical means for separating the contributions from kinetic and mass transport control. The general relationship for such a process can be written by the following form

$$\frac{1}{i} = \frac{1}{i_{\mathrm{k}}} + \frac{1}{i_{\mathrm{d}}} \tag{5.5}$$

For the present experimental conditions, the kinetic current, i_k, would be given by

$$i_{\mathrm{k}} = nFk_{\mathrm{f}}[\mathrm{Hg}^{2+}]_{\mathrm{bulk}} \tag{5.6}$$

where $[Hg^{2+}]_{bulk}$ is the bulk concentration in mol m^{-3}. The diffusion current, i_d, would be given by

$$i_d = 0.620nF[Hg^{2+}]_{bulk}D_{Hg}^{2/3}\nu^{-1/6}\omega^{1/2} \qquad (5.7)$$

where ν is the kinematic viscosity (taken to be 1.00 x 10^{-6} m^2 s^{-1}) [76] and ω is the angular velocity in rad s^{-1}.

Thus, for kinetic and mass transfer controlled reactions a Koutecky-Levich plot of $1/i$ *vs* $1/\omega^{1/2}$ for each concentration should result in linear relationships with intercepts equivalent to the heterogeneous electron transfer rate constant and diffusion coefficient may be evaluated.

5.6 Koutecky-Levich study results

The values used in the Koutecky-Levich analyse were obtained from the steady state current values from the rotation rate dependence experiments seen in Chapter 3. The linear regression analyse for Koutecky-Levich intercepts and slopes together with the error involved in each of these parameters are given in Table 5.1 as a function of the entire range of $[Hg^{2+}]$. Table 5.2 lists the resulting coefficients for Hg^{2+} evaluated using Eq. 5.7. The diffusion coefficient should be invariant with concentration at constant temperature.

Inspection of the plot D_{Hg} as a function of $[Hg^{2+}]$ is shown in Fig 5.2. This plot shows that the variation between the D_{Hg} values are not that significant and therefore the average of the five values can be take to give a single optimal value for D_{Hg} value which was found to be 6.79×10^{-10} m^2 s^{-1} with a standard deviation of 3.6×10^{-11} m^2 s^{-1}.

The Koutecky-Levich analysis was carried out on nitrate data also. The results of this analysis are displayed in Table 5.3. The resulting D_{Hg} value for nitrate was calculated as above in the case of acetate. The 5 values which were obtained for D_{Hg} in nitrate were not significantly different therefore the average of these values was obtained and the result was found to be 9.35×10^{-10} m^2 s^{-1} with a standard deviation of 5.46×10^{-11} m^2 s^{-1}.

The small and negative intercepts together with relatively large errors in the intercept do not permit determination of the heterogeneous rate constant k_f. It is likely that this parameter a high or some infinite value on this scale. Consequently, Levich plots may be

$[Hg^{2+}]_{bulk}$ / mM	slope / $A^{-1}\ m^{-1}\ s$	error in slope / $10^{-1}\ m^{-1}\ s$	intercept / $10^{-3}\ A^{-1}\ m^{2}$	error in intercept / $10^{-4}\ A^{-1}\ m^{2}$
0.5	2.250	26.01	–0.51	19.52
1.0	1.085	11.43	–0.46	8.57
2.0	0.530	8.04	–0.69	6.03
5.0	0.207	0.80	–0.13	0.60
10.0	0.111	3.56	–1.03	2.67

Table 5.1 Analysis of the Koutecky-Levich plot listing the slope and the error in the slope, together with the intercept and the error in the intercept, as a function of $[Hg^{2+}]_{bulk}$.

$\frac{[\mathrm{Hg}^{2+}]_{\mathrm{bulk}}}{\mathrm{mM}}$	$\frac{D_{\mathrm{Hg}}}{10^{-1}\ \mathrm{m}^2\ \mathrm{s}^{-1}}$	$\frac{(+)\ \mathrm{error\ in}\ D_{\mathrm{Hg}}}{10^{-1}\ \mathrm{m}^2\ \mathrm{s}^{-1}}$	$\frac{(-)\ \mathrm{error\ in}\ D_{\mathrm{Hg}}}{10^{-1}\ \mathrm{m}^2\ \mathrm{s}^{-1}}$
0.5	6.40	6.29	6.51
1.0	6.76	6.66	6.89
2.0	7.00	6.84	7.16
5.0	7.27	7.23	7.31
10.0	5.50	6.20	6.82

Table 5.2 Calculated values of D_{Hg} and the positive and negative errors in D_{Hg}, (+) error and (–) error, respectively, as a function of $[\mathrm{Hg}^{2+}]_{\mathrm{bulk}}$.

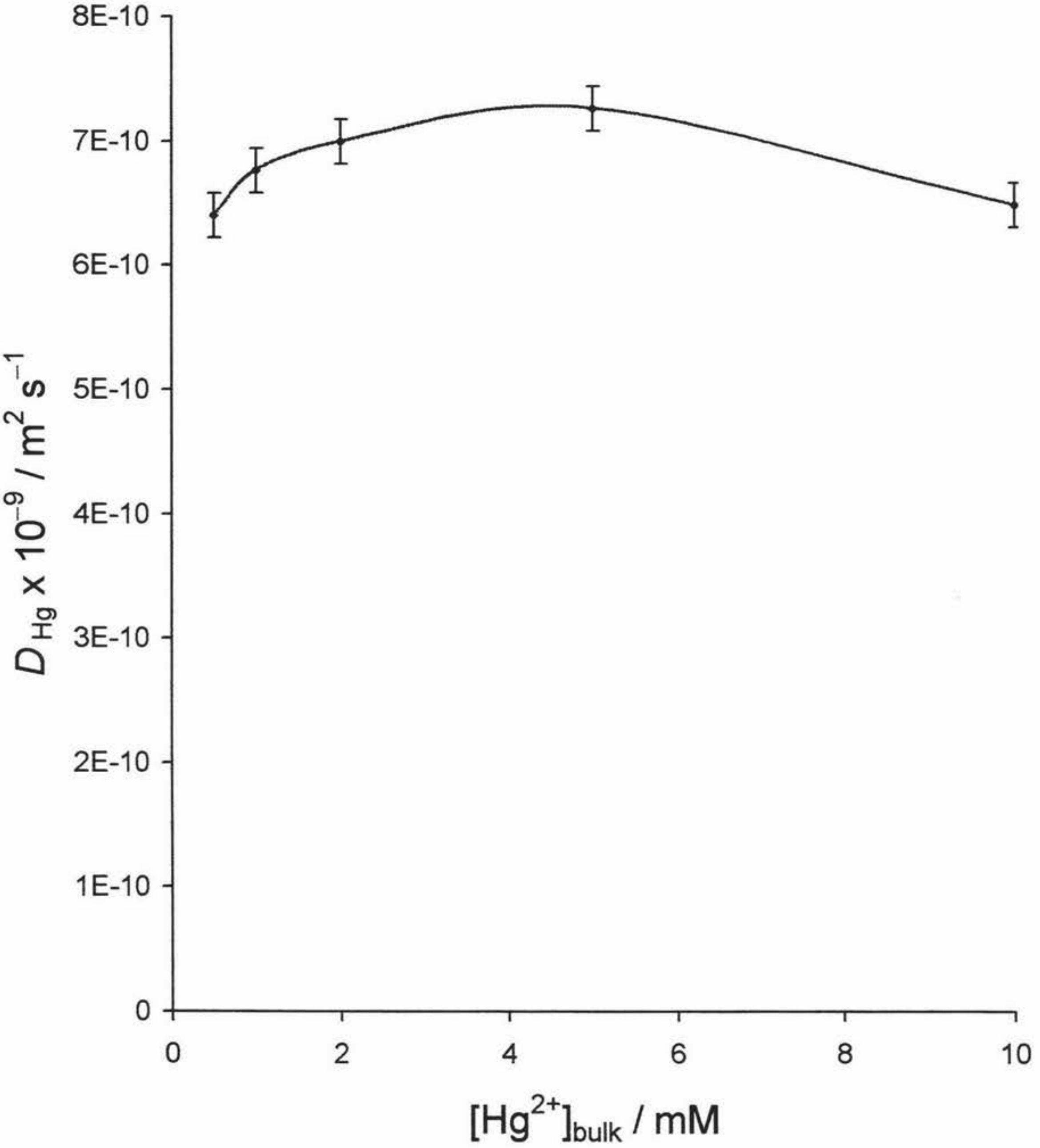

Fig 5.2 Diffusion coefficients for Hg as a function of bulk concentration calculated using Eq. 5.7.

$[Hg^{2+}]_{bulk}$ / mM	slope / $A^{-1}\ m^{-1}\ s$	error in slope / $10^{-3}\ A^{-1}\ m^{-1}\ s$	D_{Hg} / $10^{-10}\ m^2\ s^{-1}$	(+) error in D_{Hg} / $10^{-10}\ m^2\ s^{-1}$	(−) error in D_{Hg} / $10^{-10}\ m^2\ s^{-1}$
0.5	2.189	17.93	6.67	6.61	6.74
1.0	1.079	4.40	6.82	6.78	6.86
2.0	0.539	3.38	6.84	6.77	6.90
5.0	0.205	0.42	7.35	7.33	7.38
10.0	0.099	2.67	7.79	7.47	8.10

Table 5.3 Analysis of Koutecky-Levich plot in nitrate listing the slope, the error in the slope, D_{Hg}, and the positive and negative errors associated with D_{Hg}.

more appropriate for describing this reaction.

Figures 5.3 and 5.4 show the current density for the standard range of bulk Hg^{2+} concentration, $[Hg^{2+}]_{bulk}$, as a function of the square root of angular velocity, $\omega^{1/2}$ for acetate and nitrate respectively. The current increases linearly with $\omega^{1/2}$ for each concentration but the line of best fit does not pass through the origin in either case.

The linearity of the data suggests that the kinetic limitation of the electrode reaction is predominately that of mass transport and that the rate of electron transfer. The fact the data presented in both Fig 5.3 and Fig 5.4 do not all extrapolate through the origin exactly, it may be inappropriate to evaluate the diffusion coefficient of Hg^{2+} using this method.

5.7 Levich Study

If it is inappropriate to evaluate D_{Hg} using the Koutecky-Levich method the Levich may be more appropriate. The Levich analysis was carried out and the diffusion coefficient was not significantly different to that obtain in the Koutecky-Levich analysis. Figure 5.5 shows the Levich plot for the acetate data, which was the same as that used in the Koutecky-Levich study. The results for the Levich analysis confirm that it is correct to use this model and not the Koutecky-Levich model.

From the results of both the Koutecky-Levich and the Levich analysis it is assumed that the steady state current being reached throughout this work is due to the mass transport control of Hg^{2+} undergoing a 2 electron reduction to Hg^0.

This assumption is not inconsistent with the fact that under the scan rate dependence experiments the steady state current does not change with increasing or decreasing scan rate. If the steady state wasn't only due to the mass transport factor then a change in scan rate should give a change in the value of the observed steady state current, and this is not observed.

5.8 Coulometry

The section of this work using coulometry identified that the amount of mercury deposited in CVs was not all recoverable by oxidation off the GC RDE surface. The ratio Q_A/Q_C expressed as a percentage was calculated directly for both scan rate dependence and rotation rate dependence using 5.0, 2.0, 1.0, and 0.5 mM Hg^{2+}. Some of the ratios were

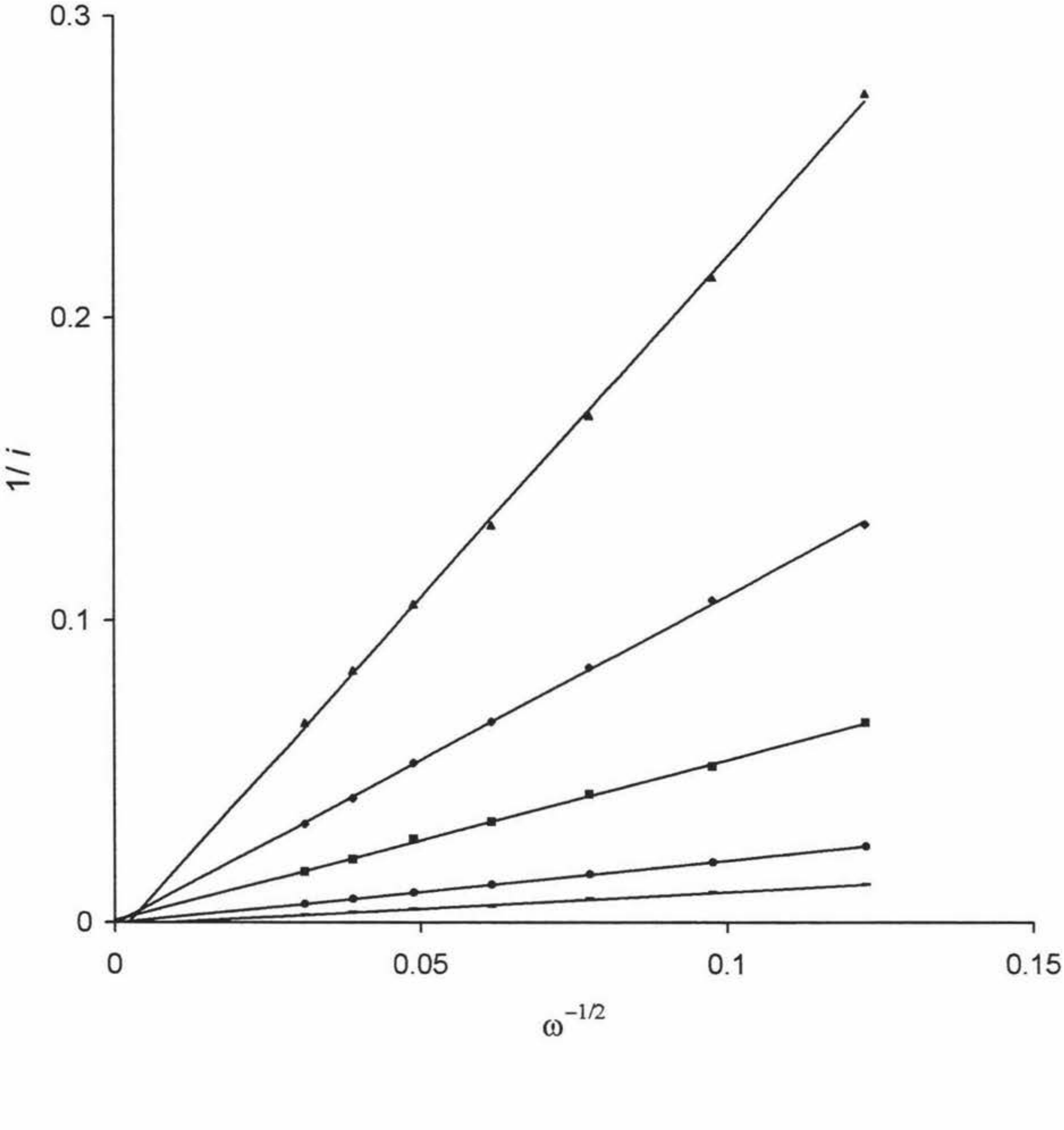

Fig 5.3 Koutecky-Levich plots for the range of bulk mercury concentrations in acetate buffer. ▲ 0.5 mM, ◆ 1.0 mM, ■ 2.0 mM, ● 5.0 mM, – 10.0 mM.

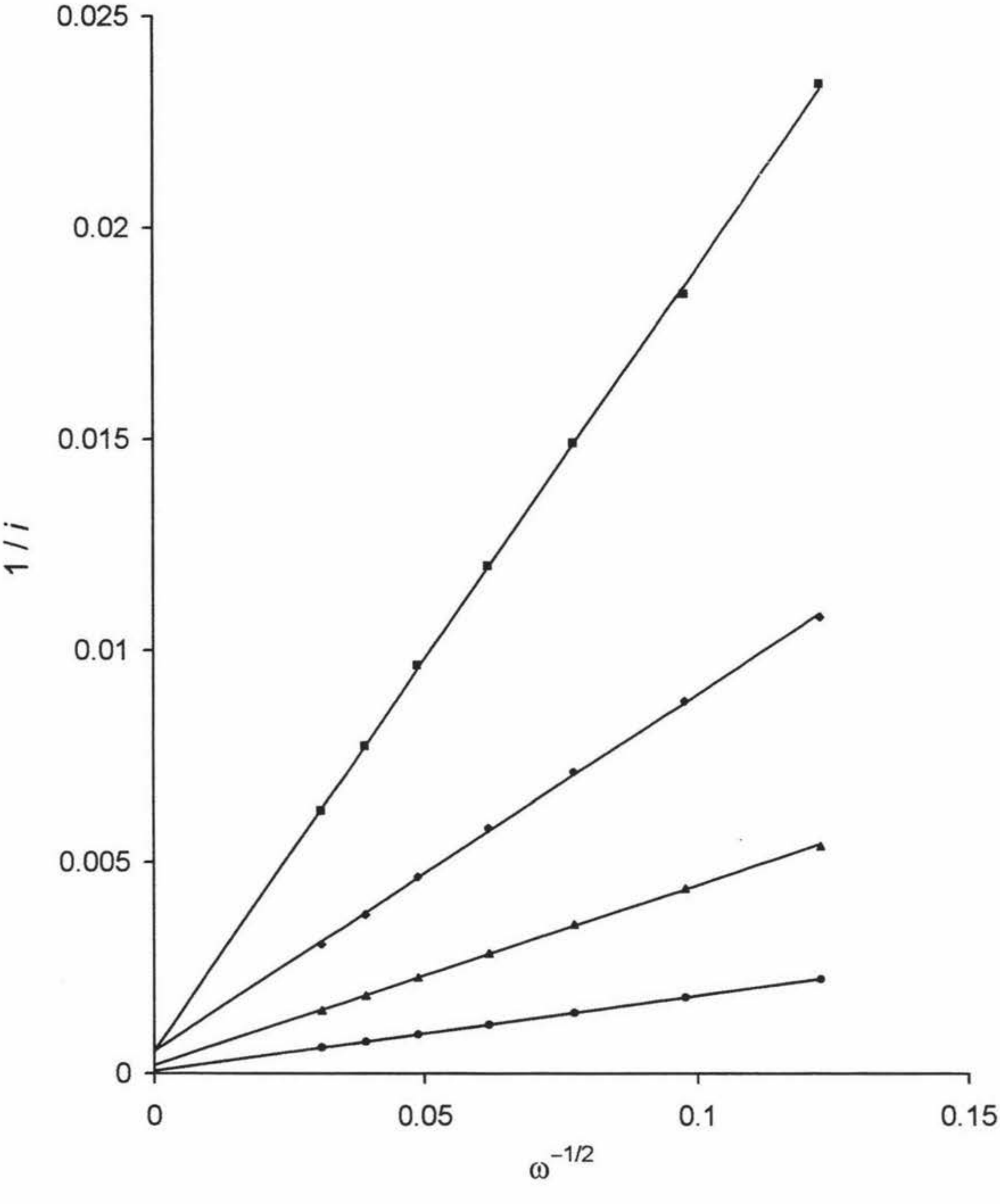

Fig 5.4 Koutecky-Levich plots for a selection of bulk mercury concentrations in a nitrate buffer. ■ 5.0 mM, ◆ 10.0 mM, ▲ 20.0 mM, ● 50.0 mM.

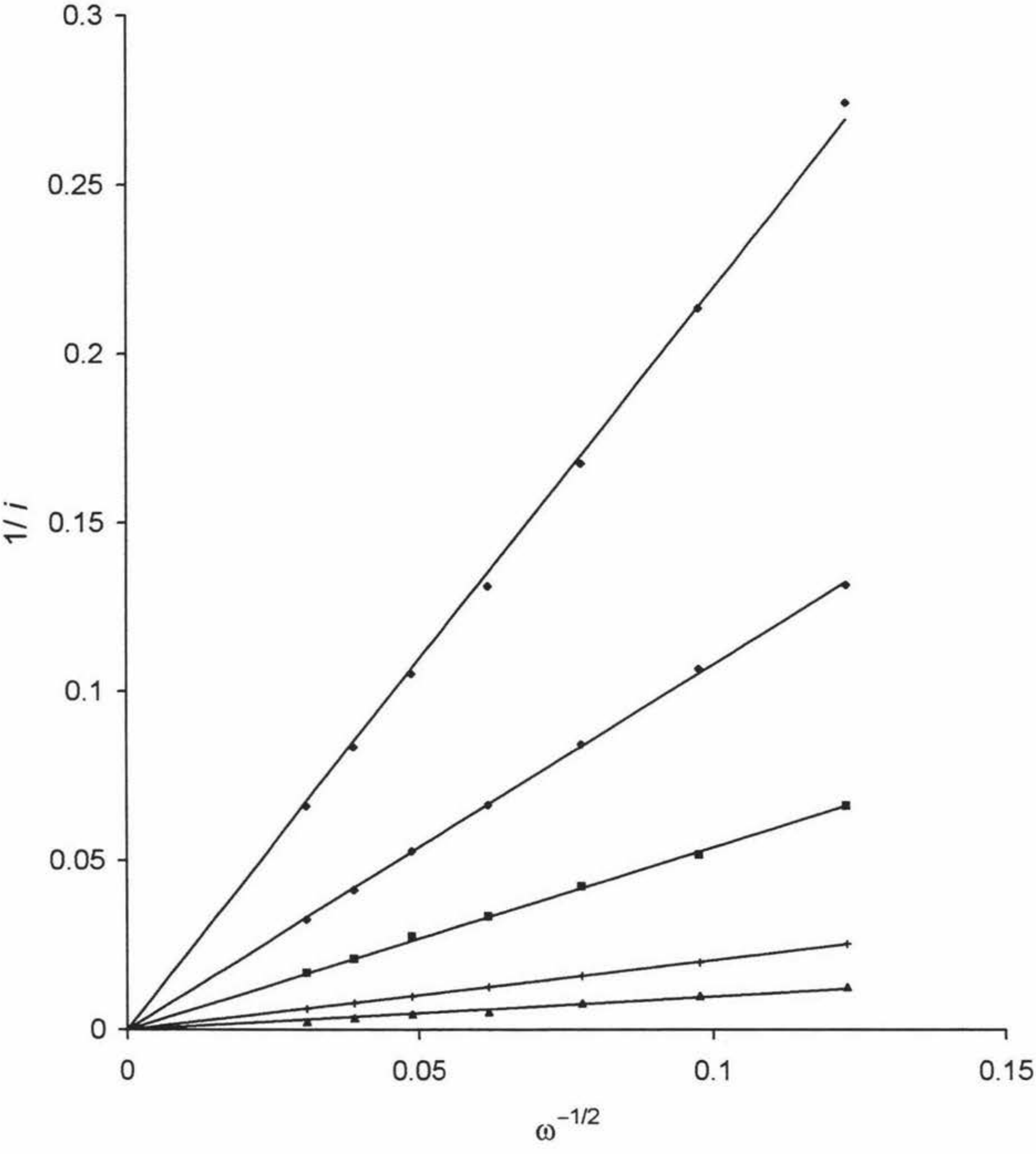

Fig 5.5 Levich plots for the range of bulk mercury concentrations in acetate buffer.

◆ 0.5 mM, ● 1.0 mM, ■ 2.0 mM, + 5.0 mM, ▲ 10.0 mM.

estimated due to incomplete peak formation, these will be indicated below.

As the rotation rate was increased from 630 to 10000 rpm the value of Q_A/Q_C for 5.0 mM Hg^{2+} decreased significantly from 42.4 % to 23.2 %. With increasing rotation rate Q_A/Q_C remained relatively constant for 2.0, 1.0, and 0.5 mM Hg^{2+}, at an average of 51.7 %, 48.4 %, and 46.4 % respectively. The values of Q_A/Q_C for 10.0 mM Hg^{2+} could not be directly calculated due to incomplete formation of the A1 peak. Estimated values for Q_A/Q_C were calculated by extrapolation of A1. The Q_A/Q_C values under rotation rate dependence can be seen in Table 5.4. The estimated values of Q_A/Q_C for 10.0 mM Hg^{2+} show that like for 5.0 mM Hg^{2+}, the Q_A/Q_C significantly decreases 36.5 % to 9.0 % with increasing rotation rate.

Similar determinations for Q_A/Q_C over the scan rate range, except that for 10.0 mM Hg^{2+} for which Q_A/Q_C could not be estimated, can be seen in Table 5.5. The Q_A/Q_C values for 200, 500, and 1000 mV s^{-1} were also not obtainable.

The results obtained from the scan rate dependence contrast with those of the rotation rate dependence. It might have been expected based upon A1 peak heights that Q_A/Q_C should increase with scan rate and rotation rate. Although only 3 values for 5.0 mM Hg^{2+} could be obtained it appears from these values that with increasing scan rate the values for Q_A/Q_C increases also, unlike with increasing rotation where Q_A/Q_C decreased.

For 2.0 mM Hg^{2+} there appears to be an optimum scan rate of 100 mV s^{-1} for oxidation of Hg^0 from the electrode as Q_A/Q_C increases to 100 mV s^{-1} and then decreases at scan rates above this.

Both 1.0 and 0.5 mM Hg^{2+} have Q_A/Q_C values, which decrease with increasing scan rate. The decrease for 0.5 mM Hg^{2+} is more pronounced than the decrease for 1.0 mM Hg^{2+}. This is also much different than in the rotation rate dependence where the values are mostly constant. This decrease 0.5, 1.0, and 2.0 mM Hg^{2+} is constant with the observation of A1 decreasing with increasing scan rate in these concentrations.

The Q_A/Q_C values were also calculated from voltammograms for 10.0 mM Hg^{2+} in nitrate media. Table 5.6 displays the results obtained from this for rotation rate dependence compared to the 10.0 mM Hg^{2+} in acetate under the same conditions. The same trend as for the 10.0 mM Hg^{2+} in acetate buffer is found with Q_A/Q_C decreasing with increasing rotation

	Q_A/Q_C / (%)				
$\frac{\omega}{\text{rpm}}$	10.0 mM	5.0 mM	2.0 mM	1.0 mM	0.5 mM
630	36.52*	42.42	51.12	47.94	46.25
1000	29.72*	40.93	51.81	48.74	46.11
1585	25.97*	39.21	51.75	8.58	46.43
2500	22.45*	37.44	52.12	48.55	46.13
4000	17.61*	34.67	52.24	48.59	46.18
6300	12.92*	30.41	51.70	48.25	46.50
10000	9.05*	23.26	51.13	48.25	46.85

Table 5.4 The Q_A/Q_C values for 10.0, 5.0, 2.0, 1.0, and 0.5 mM Hg^{2+} listed as a function of rotation rate. The values with * are estimated values.

	Q_A/Q_C / (%)			
scan rate / mV s^{-1}	5.0 mM	2.0 mM	1.0 mM	0.5 mM
20	20.26	51.55	52.19	52.54
50	33.78	52.19	51.72	49.54
100	50.04	52.55	50.51	47.69
200	–	50.72	48.09	44.16
500	–	48.02	45.31	38.92
1000	–	42.85	41.83	33.74

Table 5.5 The Q_A/Q_C values for 5.0, 2.0, 1.0, and 0.5 mM Hg^{2+} listed as a function of scan rate. (–) means that the values could not be obtained for these scan rates.

	Q_A/Q_C / (%)	
$\frac{\omega}{\text{rpm}}$	nitrate buffer	acetate buffer
630	45.68	36.52*
1000	44.82	29.72*
1585	37.89	25.97*
2500	22.92	22.45*
4000	14.11	19.61*
6300	8.57	12.92*
10000	5.56	9.05*

Table 5.6 The Q_A/Q_C values for 10.0 mM Hg^{2+} in both nitrate and acetate media for comparison listed as a function of rotation rate. The values with * are estimated values.

rate. The noticeable feature though is that the decrease is much more pronounced in nitrate. Disproportionation of Hg^{2+} with Hg^0 to form Hg^+ species is known to occur. Due to the Hg-Hg bond, for stability, the disproportionation product is that of the Hg_2^{2+} cation [77]. This disproportionation reaction may offer an explanation for these observations. If this is the case, then it appears that Hg_2^{2+} is not easily oxidised to reform Hg^{2+} in the anodic scan of the CVs. The disproportionation of mercury has been studied in the thiocyanate system [78,79] and other systems [80,81], of which a study of the disproportionation reaction within bromide and chloride solutions appeared to discuss the reaction the most [82].

5.9 Mercury (I) formation

On the basis of the proposed fact disproportination was taking place and the formation of the dimercusous ion, Hg_2^{2+}, could occur, an additional experiment was performed.

If Hg^+ does form by disproportanation of Hg^0 in acetate buffers, it was thought that if Hg^0 was added to a solution of Hg^{2+} ions, Hg^+ should form over time, with the visible sign of whether or not Hg^+ was forming, would be the amount of Hg^0 remaining.

	Hg^{2+}	+	Hg^0	→	$2\ Hg^+$
t=o	10.0 mM		3.30 mM		0.00 mM
t=∞	6.60 mM		0.00 mM		6.60 mM

where 3.30 mM of $Hg_{(l)}$ is equivalent to 0.0662 g $Hg_{(l)}$ per litre.

It was worked out that in a 10.0 mM Hg^{2+} solution 3.30 mM Hg^0 was required to end with equal amounts of Hg^{2+} and Hg_2^{2+} and no Hg^0. Solutions of 10.0 mM Hg^{2+} were made, both in acetate and nitrate media. Both solutions were purged for an hour with N_2 to ensure absence of O_2 as a redox species. The solutions were also maintained under a N_2 atmosphere throughout the experiment. 3.30 mM Hg^0 was then added to each, they were shaken and then placed in a sonacator for 30 minutes and then left for 48 hours

After 48 hours the nitrate sample had no sign of any liquid metallic Hg^0 remaining in the volumetric flask. Consequently it was assumed that Hg_2^{2+} had formed from a disproportination reaction. The fact that the solution was colourless and clear, it is assumed that Hg_2^{2+} nitrate complex is soluble.

The acetate sample on the other hand differed markedly. There was solid material remaining in this volumetric flask but not in the same presentation as at the beginning of the experiment. There was a new gray-black material on the bottom of the flask, and seemingly coated small beads of Hg^0. It appeared from this that Hg_2^{2+} had also formed here but that the resulting Hg_2^{2+}-acetate salt was insoluble and provides a semi-passivating layer on Hg^0 preventing completion of the disproportionation reaction. Ultrasonication of this grey material eventually resulted in a uniform white precipitate with no remaining Hg^0. It was presumed that ultrasonication effectively disrupted the passive layer of $Hg_2(OAc)_2$.

With this new information in mind, the differences between observations for acetate and nitrate were examined in new light. It is possible C1 and C2 had something to do with the formation of this new Hg_2^{2+} material or that the Hg_2^{2+} at least plays a role in the formation of C1 and C2, since they do not form in nitrate.

If A1 is associated with the oxidation of Hg^0 this would explain the result from the last section. At low rotation rates Hg^0 forms, disproportionation occurs, some Hg_2^{2+} can reform Hg^0 or, Hg^{2+} which then can form Hg^0. Then at higher rotation rates where the values for Q_A/Q_C finally decrease to below 10 %, the Hg_2^{2+} that forms is dispersed into the bulk before it has time to reform Hg^0 or Hg^{2+} at the electrode surface.

In the other situation where a seemingly insoluble $Hg_2(OAc)_2$ forms, it can not disperse into the bulk as the $Hg_2(NO_3)_2$ complex can. At higher rotation rates more Hg^0 is formed so more disproportionation to Hg_2^{2+} should occur. Although if this insoluble Hg_2^{2+} complex is not able to very easily reform Hg^0 the decrease seen in Q_A/Q_C would be expected, but not to the same extent as the nitrate situation. This may be due to the fact that even if in is slow the $Hg_2(OAc)_2$ complex is present at the electrode surface to reform Hg^0.

5.10 Microelectrodes

By using GC ME the studies are being carried out on a highly inert microelectrode substrate [83]. Highly inert implies that the rates of any side reactions are very low compared to those of the phase growth processes, and it is therefore possible to observe these in the initial stages. The work of adhesion between the substrate and the new phase is sufficiently small that nucleation is sufficiently retarded on a microelectrode. The microelectrode has sufficiently small dimensions so that a single supercritical nucleus may be formed during the period of measurement of the growth of the 3-D centre or if several supercritical nuclei are formed. The rate of nucleation is nevertheless sufficiently slow that the growth of the first centre from the overall current-time transient can be discerned.

An example of the electrocrystallisation of α-PbO_2 is a slow reaction, and the growth follows the kinetically controlled law [83].

$$i = \frac{-4\pi F k^3}{\rho^2}\,(t-t_0) \tag{5.8}$$

where ρ (g cm^{-3}) the density, k (mol cm^{-2} s^{-1}) is the rate constant of the crystal growth at the particular overpotential and t_0 (s) is the time at which the nucleus is first formed. Equation 5.8 has been written assuming that the growth is that of a hemispherical growth centre. It is also assumed that the growth of a Hg^0 nucleus will follow the same kinetically controlled law.

In the simplest case it is assumed that after the potential step occurs then nuclei form at discrete centers and grow laterally across the surface to form discs.. It is also assumed in this case that the rate of growth (current) is proportional to the area (A) onto which deposition occurs, and that the growth area can be modified due to overlap with an adjacent nucleus. From these assumptions to current may be written as

$$i = nFkA \tag{5.9}$$

where k is the rate constant (mol m^{-2} s^{-1}). The current is also equal to the rate change of the accumulated charge with time on the surface. Therefore application of Faradays law gives

$$i = nF\rho(\mathrm{d}V/\mathrm{d}t)/M \tag{5.10}$$

where ρ and V are the density and volume of the deposited phase, and M is the molecular weight. The derivative dV/dt can be expanded with respect to the radius, r. Equating equations 5.9 and 5.10 gives

$$\mathrm{d}r/\mathrm{d}t = \frac{MkA}{\rho(\mathrm{d}V/\mathrm{d}r)} \tag{5.11}$$

Substitution for A and V for a disk of height h

$$A = 2\pi rh \tag{5.12}$$

$$V = \pi r^2 h \tag{5.13}$$

$$\mathrm{d}r/\mathrm{d}t = Mk/\rho \tag{5.14}$$

If equation 5.8 is then integrated with respect to time to give the time dependence of the radius of a single nucleus the result is

$$r = Mkt/\rho \tag{5.15}$$

It is assumed that in this work this simplest case is not the type of growth being achieved. This is based on liquid mercury forming but with sufficiently high surface tension to enforce spherical or hemispherical growth. Hemispherical growth is considered and if these growth centers occur then equations 5.12 and 5.13 become

$$A = 2\pi r^2 \tag{5.16}$$

$$V = 2\pi r^3/3 \tag{5.17}$$

Substitution of Equations 5.16 and 5.17 into equation 5.11 gives the Equation 5.14 and hence Equation 5.15. As in the simplest model the current due to growth of a single nucleus is obtained by substitution of Equations 5.15 and 5.16 into Equation 5.9 giving

$$i = 2\pi nFk(Mk/\rho)^2t^2 \tag{5.18}$$

The growth of Hg^0 nuclei is assumed to be progressive and not instantaneous nucleation and growth so with this in mind the growth of the transients from the CA experiments should therefore be proportional to t^2 according to Equation 5.18. This assumption is aided by the observation in the CA experiments using a ME that the onset for reduction is delayed and random in nature as shown in Fig 4.7.

The transients in Fig 4.1 do not follow this t^2 dependence.

To establish the time dependence all of the transients in Fig 4.1 they were deconvoluted by fitting Equation 5.19 to the original data.

$$I = k_{\mathrm{red,nuc}}\, exp(t-t_o)^x \tag{5.19}$$

where $k_{\mathrm{red,nuc}}$ is the rate constant for the growth of the nucleus, x is some power function, and t_o is the time at which the nuclei is first formed. The results of the optimisation of $k_{\mathrm{red,nuc}}$ and x are listed in Table 5.7 for a series of replicate experiments. It appears from these results that the first nucleus that forms on the electrode follows a $t^{1/2}$ function.

Figure 5.6 shows the multi-plot of the calculated curves made to fit those of Fig 4.1. There is an excellent fit of the calculated transients to those of the real data with no significant differences between observed and fitted data.

The origin of this $t^{1/2}$ dependence may be accounted for by correlating with the calculated radius as a function of time for a growing hemisphere. This may be achieved by integration of each experimental transient in Fig 5.6 to give Q_c as a function of time and converting to radius assuming a hemispherical droplet.

Figure 5.7 shows a plot of current *vs* calculated radius for one of the transients from Fig 4.1. An explanation for the linear relationship between current and radius is that the current is proportional to the perimeter length of the growing droplet. With perimeter growth it might indicate that unlike growth onto a hemispherical droplet with a Hg^0/ Hg^{2+} interface, you need a 3-way interface between GC/ Hg^0/ Hg^{2+}. Colyer said that 'sooner or later every surviving mercury droplet will reach the junction between the disc and the

transient number	order x	rate constant $10^{-1}\ k_{\mathrm{red,nuc}}$
1	0.50987	1.4206
2	0.50088	1.5099
3	0.50279	1.4846
4	0.499979	1.5261
5	0.50235	1.4910
6	0.50209	1.5044
Average	0.50299	1.4894

Table 5.7 The optimisation results and averages for $k_{\mathrm{red,nuc}}$ and x listed for a series of ME CA transients.

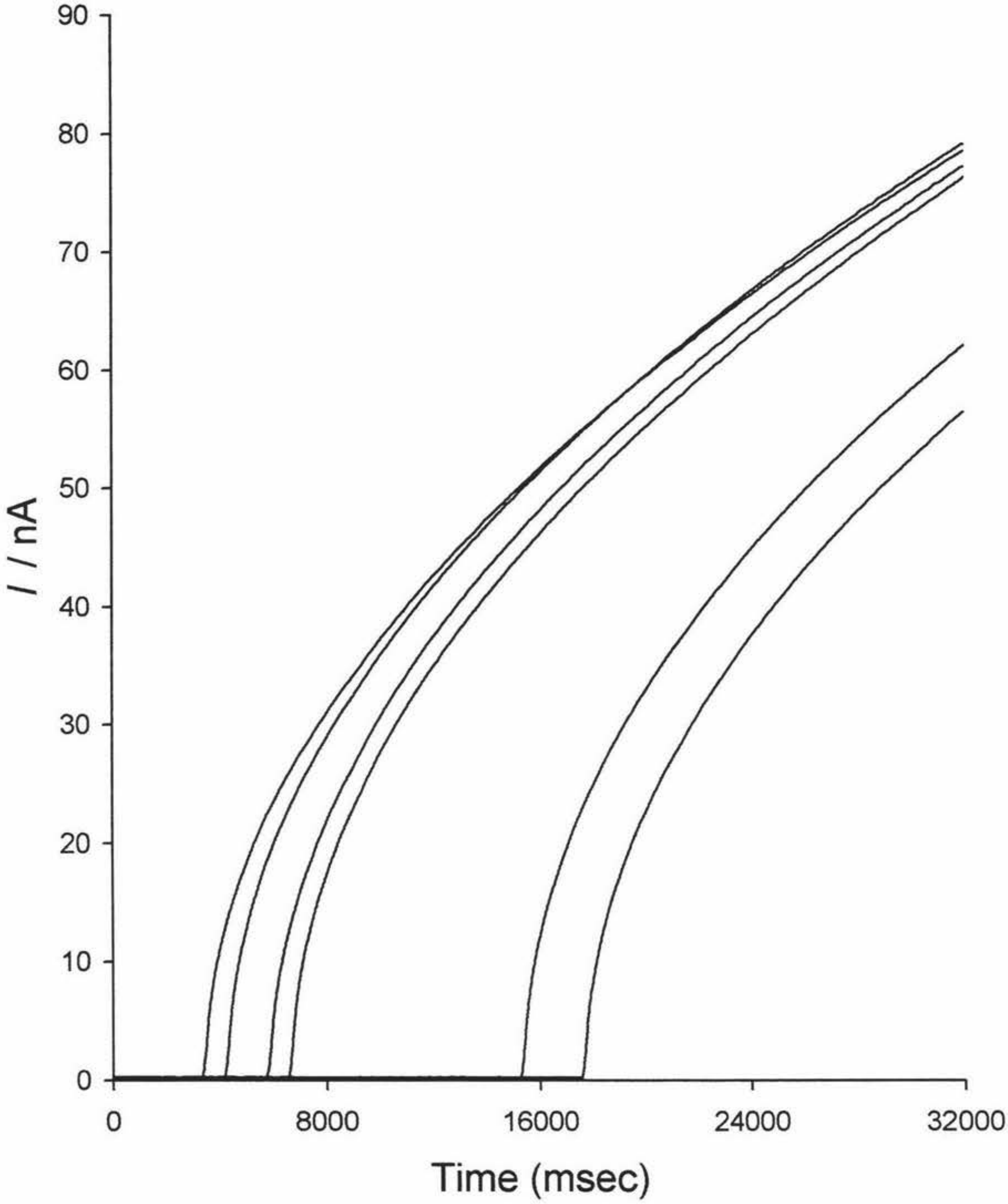

Fig 5.6 Calculated ME growth transients that fit exactly those in Fig 4.7.

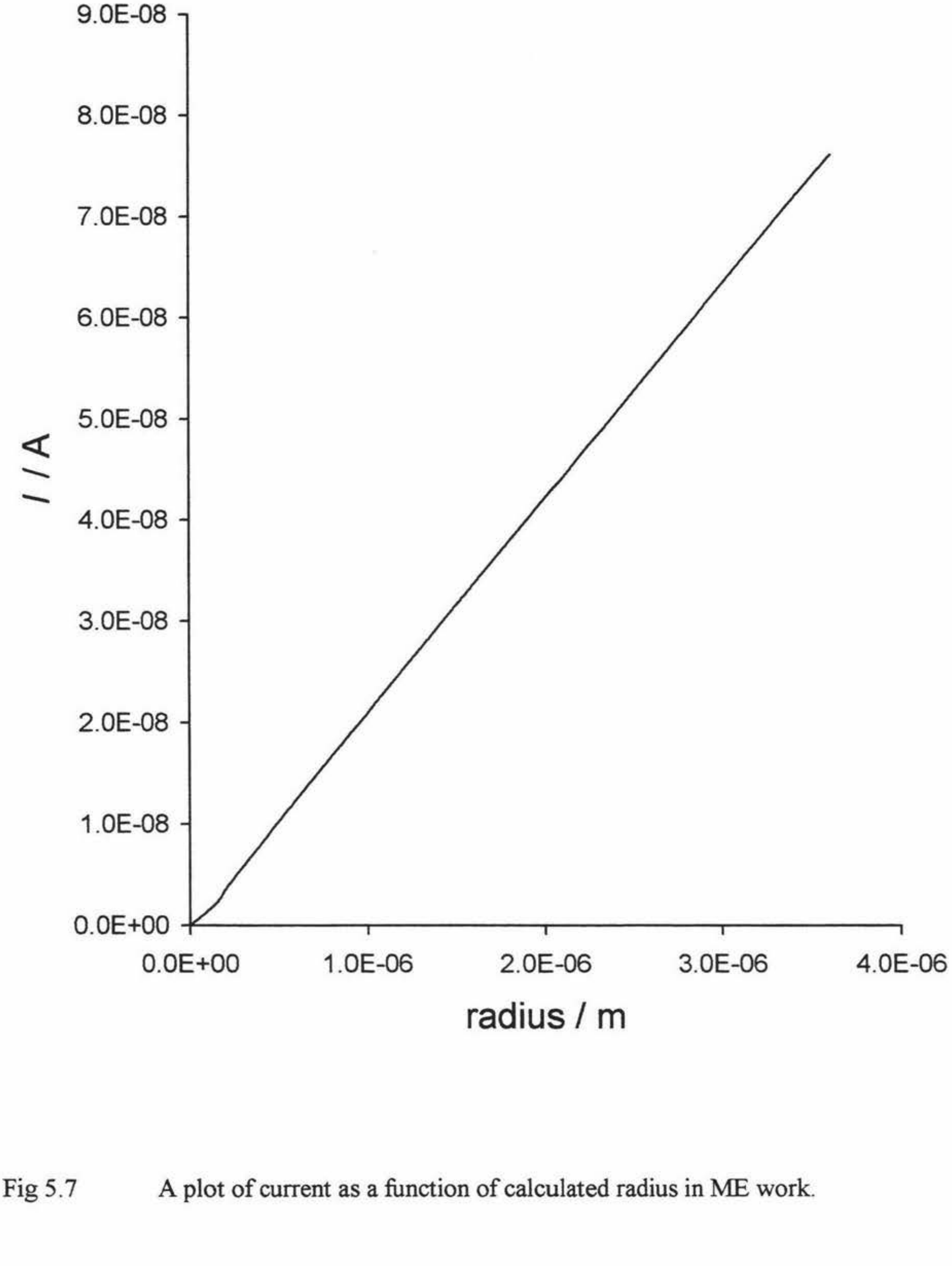

Fig 5.7 A plot of current as a function of calculated radius in ME work.

insulator that surrounds it' [17]. This must be considered in the present case since the hemispherical radius is approximately 80 % of the ME radius at the end of the transient in Fig 5.7. Colyer goes on to say that when the droplet reaches the edge of the disc it will either continue to grow within the confines of the disc or it will move off the disc onto the insulator [17]. These two situations could be occurring on the surface of the ME in this work along with at least one other possibility not mentioned by Colyer where the mercury droplet continues to grow from the GC and onto the insulating glass, thereby covering both substrates. Fig 5.8 shows the three growth possibilities pointed out here.
The hypothesis adopted here for perimeter growth instead of the expected area dependence is that most of the hemisphere is covered with a Hg_2^{2+} film and the only clean, Hg_2^{2+}-free Hg^0 is that which is being continuously exposed at the base of the growing hemisphere. The height of this band of electrochemical activity must be sufficiently small so that the area is directly proportional to the perimeter.

Figure 5.9 shows the early stages of nuclei formation with a plot of the current *vs* time. From this point with several calculations the radius as a function of time can be found. Having Q_c interpreted for r it appears that at the start of the growth transient follows

$$I \alpha r^2 \tag{5.20}$$

This, as shown in Fig 5.10, indicates that in the early stages before significant $Hg_2(OAc)_2$ film formation it is surface area dependent, and follows the expected order. After the radius reaches 2.6 μm (or after 180 ms) the rate of growth changes. It now appears to follow

$$I \alpha r \tag{5.21}$$

which is now established to be perimeter growth control. It would appear to take 180 ms or a 2.6 μm radius before sufficient mercury has deposited before growth of the hemispherical droplet can only take place at the perimeter.

Fig 4.11 showed that a selection of transients for E_2 more cathodic than 0 mV. This showed transients unlike those in Fig 4.9 that followed $t^{1/2}$, now interpreted in terms of multiple nuclei forming. However, at these lower E_2 values more rapid passivation by $Hg_2(OAc)_2$

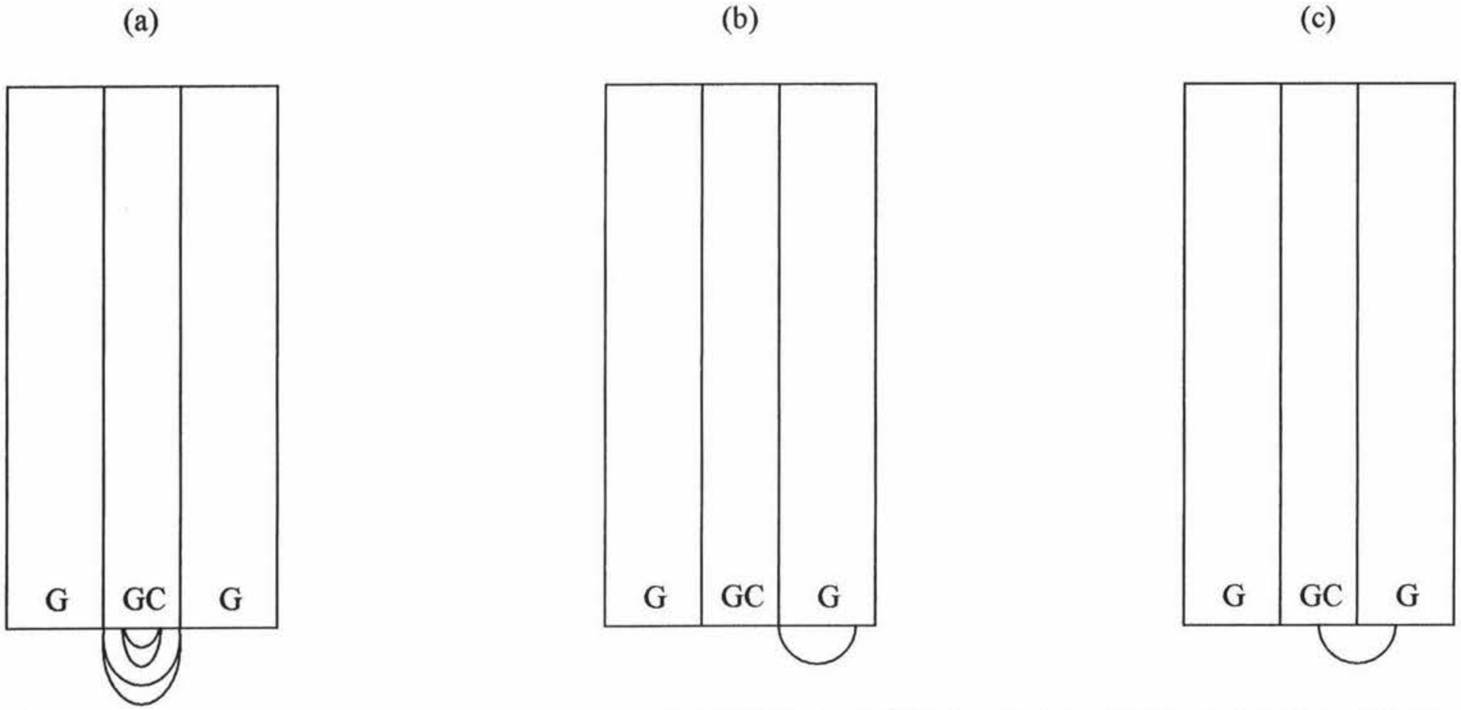

Fig 5.8 Three different possibilities of how mercury droplets could grow on a ME. (a) growth only on GC, (b) growth only on G but touching the edge of the GC, or (c) growth on both GC and G.

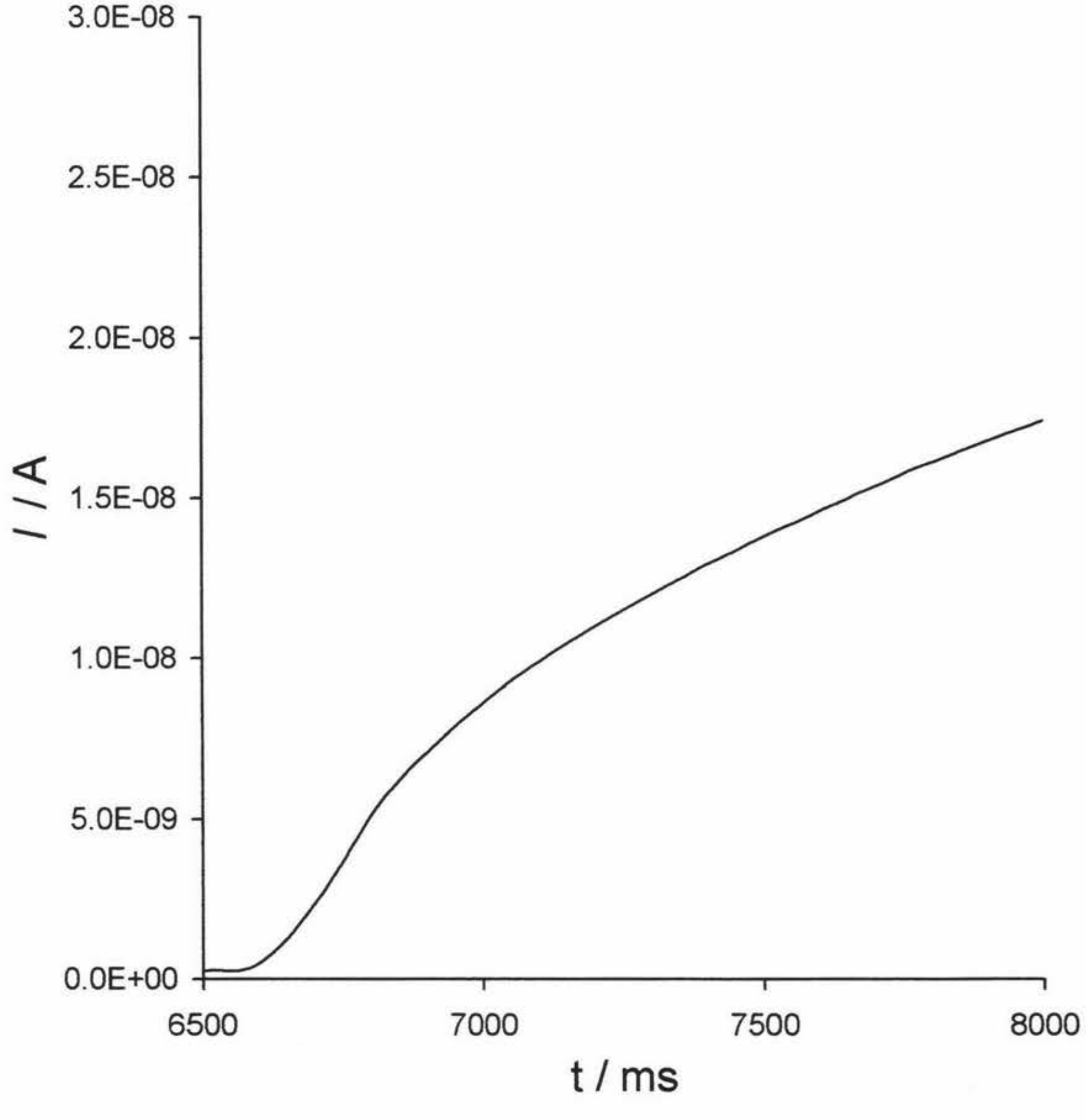

Fig 5.9 A plot of current as a function of time in ME work.

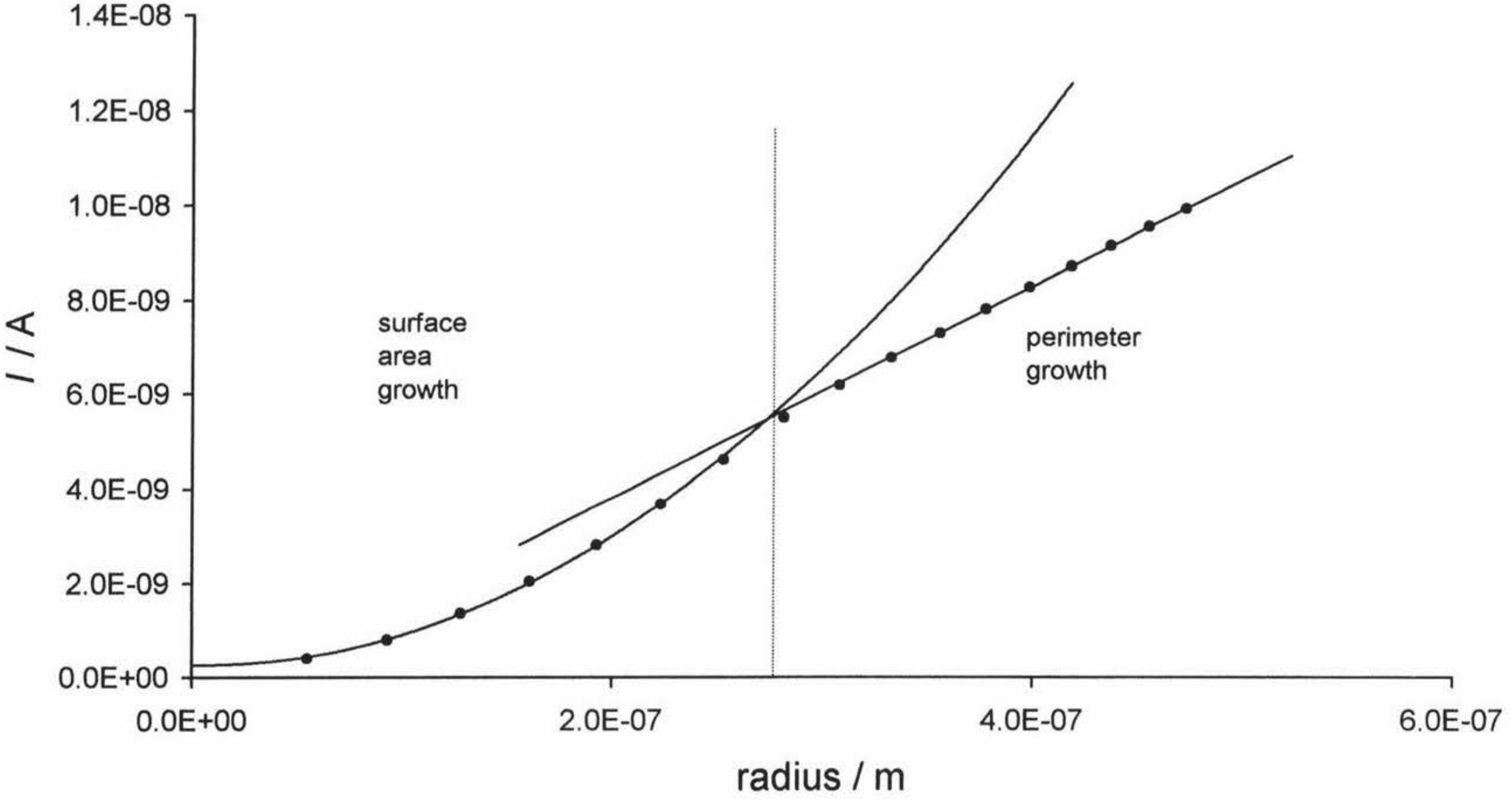

Fig 5.10 The early stages of current as a function of radius showing the point where surface are dependence growth changes to perimeter dependence growth.

film is assumed to be occurring. This can not be diffusion current since it is less than 1 % of the highest current recorded for growth transients. It is not unlikely that this small current represents limited conduction through a coherent $Hg_2(OAc)_2$ passivating film on small and rapidly produced Hg^0 droplets on hemisphere.

The transient presented in Fig 4.8 displays a different series of events. Here there is at least one other increase in current above the $t^{1/2}$ response. This additional current is interpreted in terms of growth of at least one other nucleus on the GC surface. These extra growths could not be fitted to the same level of confidence for $t^{1/2}$. However it is clear that the second transient had time dependence less than $t^{1/2}$ and there were strong indications that it was close to $t^{1/4}$. This lower than expected *t*-dependence for a second growing nuclei may arise from close proximity to the, by then, relatively large first formed droplet. This may result in the second droplet growing at a more reduced rate due to impeded diffusion of Hg^{2+} to the growing perimeter. The influence of the growth of the second droplet on the first droplet would be small given the size difference.

Figure 4.10 displays yet another different feature occurring on these MEs. It seems to be the case here that a second nucleus is starting to develop, as seen in Fig 4.8, but not long after it begins to grow it ceases presumably due to loss of electrical contact to the electrode, or merging of the smaller droplet with the larger original droplet. There is a drop in current down to the current that would have been achieved if the first single nucleus were left to grow, both before and after the growth of the second nucleus the power function of the transient is $t^{1/2}$.

There is a case in [17] where it is discussed that 2 thin films of mercury wet the disc apart from a small area and this changes to a situation where 1 film wets the disc completely as this second situation with complete wetting would be more favourable. Figure 5.11 shows one interpretation of these responses. When the second nucleus starts to grow it is in close proximity to nucleus 1. After some time they start to touch. The drop in current is assumed to occur when nucleus 2 is consumed by nucleus 1. The volume of nucleus 2 is not very large compared to nucleus 1, so when the two combine to form one nucleus the change in radius for nucleus 1 is not significant so the transient appears to continue along the expected path for growth of a single hemisphere.

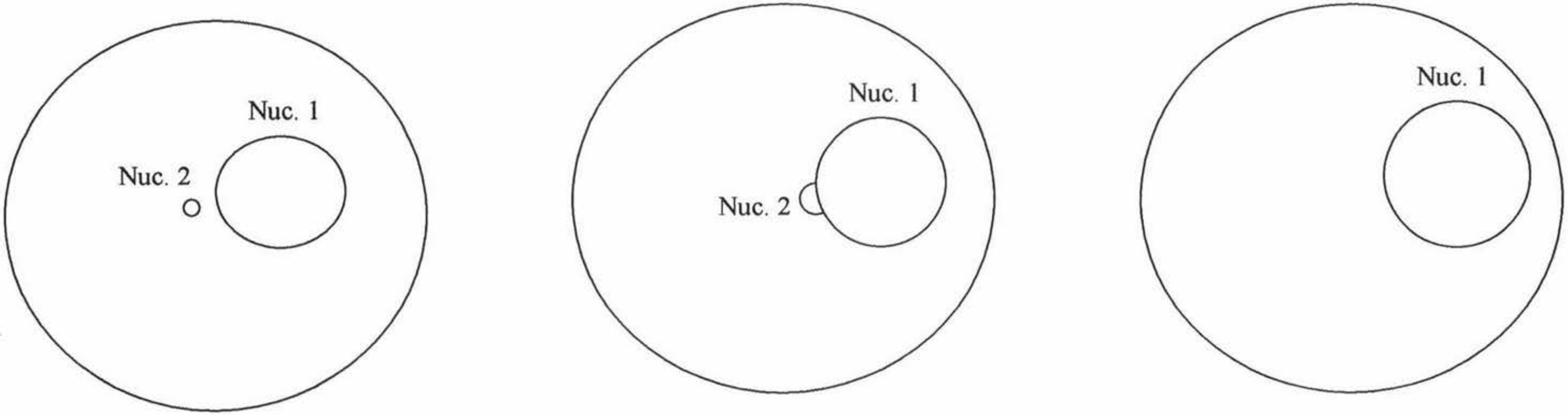

$t = 1$ $t = 2$ $t = 3$

Fig 5.11 Schematic diagram of a smaller second nucleus jointing a well established, larger, other nucleus.

In the case where the ME is not mechanically-cleaned between experiments and electrochemical-cleaning is undertaken there is a decrease in the maximum current the growth transients can achieve. This may be due to a build up of $Hg_2(OAc)_2$ film on the electrode surface inhibiting the ability for droplet growth to occur. With all of the transients occurring throughout this microelectrode study except when there are multiple nuclei growing, the first nucleus always has a power function of $t^{1/2}$. Even when the transients do not last a very long before being lost, they all still appear to follow $t^{1/2}$ dependence.

5.11 Electrochemical cleaning/ Overpotential shift

The concept that a $Hg_2(OAc)_2$ film could be covering part of the surface of the GC electrode was briefly introduced towards the end of the previous section. This is thought to be responsible for a number of features observed in the RDE work.

The possibility of Hg_2^{2+} forming through the disproportionation reaction was also proposed earlier in this chapter. It is most likely that any film that is achieved would be in the form of a $Hg_2(OAc)_2$ film. It is assumed that this film is semi-passivating. If it were completely passivating then the current would drop to zero in the cyclic voltammograms and potential step experiments. Consequently, it is proposed that reduction of Hg^{2+} to Hg^0 may still take place through the $Hg_2(OAc)_2$ film. It stands to reason that if reduction can occur through this $Hg_2(OAc)_2$ film then so might oxidation, and this also appears to be the case. This suggests that on GC RDE all of the Hg^0 under $Hg_2(OAc)_2$ films may be oxidised leaving only the $Hg_2(OAc)_2$ film on the GC surface. A key observation seen throughout this work has been the shift in the potential at which reduction commences, E_{red}, with cycling after cleaning, either mechanical or electrochemical. This may now be interpreted in terms of this $Hg_2(OAc)_2$ film. The $Hg_2(OAc)_2$ film remaining on the electrode acts as a catalyst or as a site which more readily permits the reduction of mercury than it does on a mechanically-cleaned GC surface free of this film.

Electrochemical-cleaning under anodic conditions might also remove this $Hg_2(OAc)_2$ film if it were either slow to oxidise or removed only by mechanical action of O_2 gas bubble production. Indeed, electrochemical-cleaning did return E_{red} to similar value for fresh mechanically polished electrode. A shift in E_{red} is also seen as the system is left at open potential, and this is explained by the fact that it is assumed that the $Hg_2(OAc)_2$ film does not adhere strongly to the surface of GC. The longer the system is left at open potential the more $Hg_2(OAc)_2$ film sloughs off during electrode rotation.

The peaks C1 and C2 also decrease with increasing the cleaning potential and/or the cleaning time and with increased time left at open potential, so it is assumed that C1 and C2 are strongly linked to the presence of this $Hg_2(OAc)_2$ film. This feature will be accounted for in the mechanism proposed in the following section.

5.12 Mechanisms

5.12.1 *Model I*

As a first model it was proposed that Hg^{2+} reduced to Hg^0 as a hemispherical droplet. As the deposition of Hg^0 occurred the disproportionation reaction also occurred, coating the hemispherical droplet with a $Hg_2(OAc)_2$ film occurs. Under subsequent oxidation conditions Hg^0 oxidises through the film but oxidation of the $Hg_2(OAc)_2$ film was incomplete, leaving this material on the surface of the GC RDE. This $Hg_2(OAc)_2$ film then acting as catalyst for the one electron reduction of Hg^{2+} to Hg_2^{2+}, accounting for the shift in E_{red} and the growth of C1. C2 is then proposed to be due to the two-electron reduction of Hg_2^{2+} to Hg^0, again occurring through this $Hg_2(OAc)_2$ film. Hemispherical droplets of Hg^0 forming under the $Hg_2(OAc)_2$ film was thought to then occur. These relatively unstable hemispherical Hg^0 droplets then 'flip' to a spherical droplet leaving bare GC where reduction of Hg^{2+} to Hg^0 may occur. This rapid Hg^{2+} reduction to Hg^0 on clean GC surface accounting for the current spikes. Further disproportionation occurs to reform the $Hg_2(OAc)_2$ film leaving a spherical Hg^0 droplet covered in a $Hg_2(OAc)_2$ film. Fig 5.12 shows a schematic diagram of the steps in Model I. However, whilst adequately describing C1, C2, and E_{red} a number of features may not be accounted for using this model. These include the disappearance of C1 and C2 with electrochemical-cleaning and time left at open potential.

5.12.2 *Model II*

This model retained several features of Model I including the idea of growth of mercury

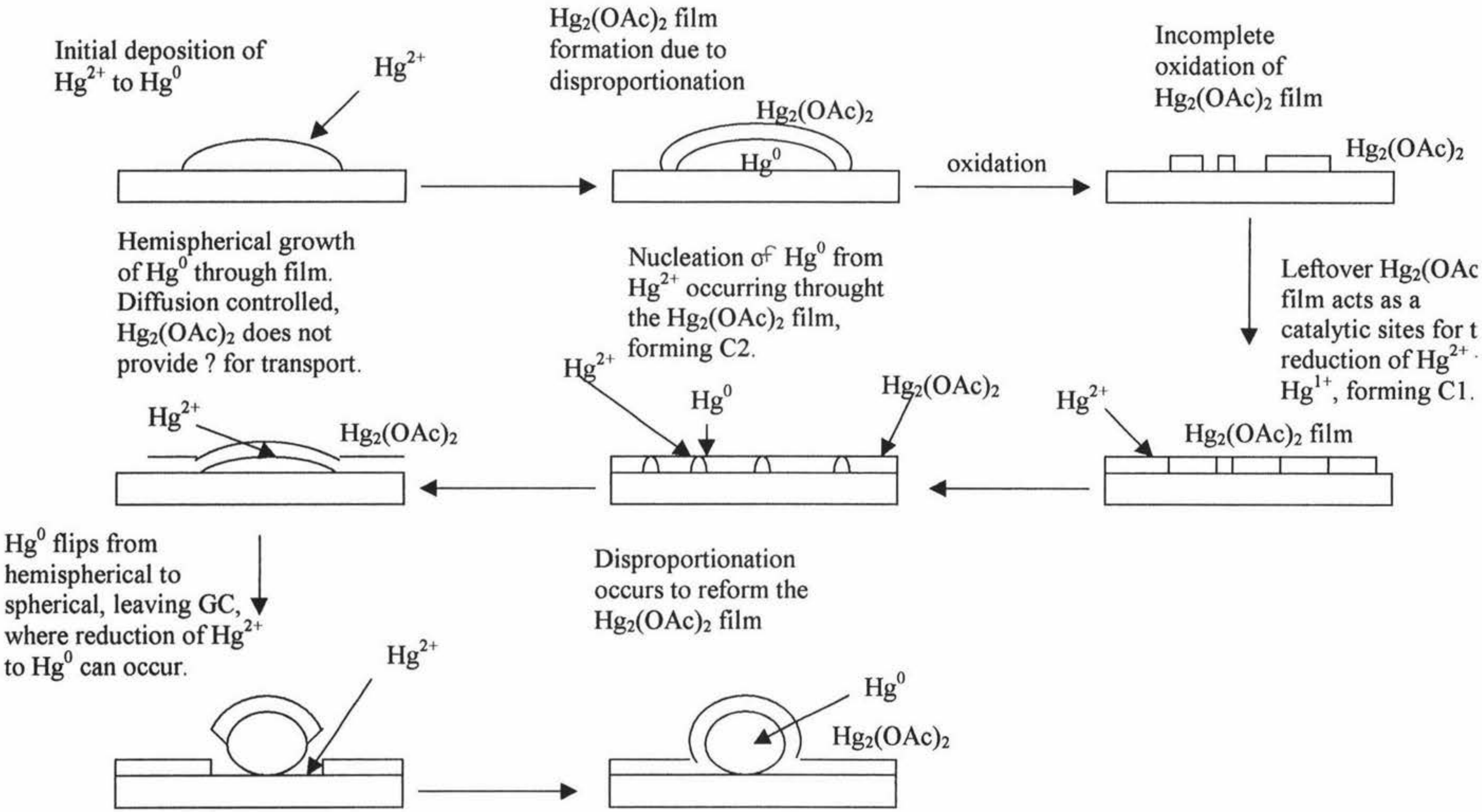

Fig 5.12 A schematic diagram for Model I.

droplet through a $Hg_2(OAc)_2$ film and $Hg_2(OAc)_2$ film remaining on the surface of the GC electrode acting as a catalyst for Hg^{2+} reduction to Hg^0 giving rise to the shift in E_{red}. During the reduction the predominate reactions are the two electron reduction of Hg^{2+}

$$Hg^{2+}{}_{(aq)} \quad + \quad 2\,e^- \quad \rightarrow \quad Hg^0 \tag{1.1}$$

together with the disproportionation reaction to give the semi-passivating film $Hg_2(OAc)_2$

$$Hg^{2+}{}_{(aq)} + 2OAc^-{}_{(aq)} + Hg^0 \rightarrow Hg_2(OAc)_{2\,(film)} + Hg_2(OAc)_{2\,(aq)} \tag{5.22}$$

$Hg_2(OAc)_2$ is sparingly soluble so some of this is lost to the aqueous phase. These reactions are mass–transport controlled by D_{Hg} since the Levich model is followed.

It is thought that there are three parallel reductions occurring after the first cycle. C1 is thought to be due to the reduction of $Hg_2(OAc)_2$ film containing small Hg^0 droplets remaining after the A1 peak of the first cycle.

$$2\,Hg^{2+}{}_{(aq)} + 2e^- + 2OAc^-{}_{(aq)} \xrightarrow{GC,\ Hg_2(OAc)_2} Hg^0 \tag{5.23}$$

The gaps of bare GC between the $Hg_2(OAc)_{2(S)}$ film decreases with the formation of more $Hg_2(OAc)_2$. This accounts for the shift in E_{red}.

C2 is thought to be due to the reduction of $Hg_2(OAc)_2$ film free of underlying Hg^0 but that is still in contact with Hg^0 or GC, or $Hg_2(OAc)_2$ free of Hg^0, reducing on GC,

$$Hg_2(OAc)_2 \quad + \quad Hg^0 \xrightarrow{GC,\ Hg_2(OAc)_2} Hg^0 \tag{5.24}$$

which is progressively impeded by the disproportionation reaction

$$Hg^{2+}{}_{(aq)} \quad + \quad Hg^0 \quad + \quad 2OAc^- \rightarrow Hg_2(OAc)_2 \tag{5.25}$$

When C1 is large C2 is not, this is due to the overlap of a decreased surface area since C2 needs GC, $Hg_2(OAc)_2$, and Hg^{2+} to form.

As C1 decreases with cleaning C2 increases to a point where there is an ideal situation. Once that ideal situation is dropped below then C2 also starts to decrease.

During the oxidation sweep it is thought that these reactions occur

$$Hg_2(OAc)_{2(S)} \xrightarrow{\text{GC (slow)}} 2Hg^{2+}_{(aq)} + 2OAc^-_{(aq)} + 2e^- \tag{5.26}$$

$$Hg_2(OAc)_{2(S)} \xrightarrow{\text{Hg (fast)}} 2Hg^{2+}_{(aq)} + 2OAc^-_{(aq)} + 2e^- \tag{5.27}$$

and is thought that A1 is due to

$$Hg^0 \xrightarrow{\text{Hg (fast)}} Hg^{2+}_{(aq)} + 2e^- \tag{5.28}$$

with the oxidation of A2 thought to be due to be due to

$$Hg_2(OAc)_2 \xrightarrow{\text{GC}} 2Hg^{2+} + 2e^- \tag{5.29}$$

It is assumed that Equation 5.26 is slow due to the results for the cleaning potential experiment. For example $Hg_2(OAc)_{2(S)}$ may be removed by oxidation at +1000 mV but this takes a very long time. If however a potential of +1600 mV is employed, the cleaning time is 40 times faster. At this stage it is also assumed that the GC surface is predominately free of $Hg_2(OAc)_2$ film. Electrochemical-cleaning reduces the size and the number of $Hg_2(OAc)_{2(S)}$ film sites which implies that there is a size distribution of this film islands.

$$Hg_2(OAc)_2 \xrightarrow{\text{GC}} 2Hg^{2+} + 2e^- \tag{5.30}$$

There are least three possibilities for the current spikes. First, that they are due to the flipping of mercury droplets from hemispherical too spherical. Secondly, isolated $Hg_2(OAc)_2$

coming into contact with Hg^0, and lastly the reduction of extra $Hg_2(OAc)_2$ film to give continuous thickness.

This model also works for the observations of C1 and C2 increasing and decreasing with rotation rate and scan rate which Model I did not do.

Figure 5.13 incorporates these and other new features of Model II in a modified form of the scheme shown in Fig 5.12.

Figure 5.14 links the events to a schematic voltammogram.

5.13 Conclusions

A number of important conditions involved with the deposition of mercury on glassy carbon have been identified in this work and have been found to include: deposition potential; scan rate effects; hydrodynamic effects; electrode pre-treatment; mercury concentration; and composition of the electrolyte.

These factors have been studied and a number of generalities and specific effects on mercury deposition have been identified and explained.

The deposition potential has been shown to have a great effect on the reduction of mercury as seen in the ME work. When the E_2 potential was outside the limits of 100 and 0 mV the growth transient seen in Fig 4.7 were not observed any longer, either the current dropped to very low values at potentials below 0 mV, or at potentials above 100 mV transient did not grow.

The scan rate and hydrodynamic effects have also been shown to be important. At high scan rates current spikes are seen which are not seen at lower scan rates. At low concentrations as the scan rate is increased the height of A1 decreases which it does not do at higher concentrations. Rotation rate effects the amount of Hg^{2+} reaching the surface of the electrode, therefore effecting the steady state current being reached. The rotation rate also effects the ability for the formation of C1 and C2.

The concentration has been shown to be important. This can be seen by the fact that C1 and C2 are not seen at the low concentration where they are at higher ones. The amount of material being reduced and therefore reacting in the ways seen for Model II, and hence the amount of $Hg_2(OAc)_2$ film that could form at the lower concentrations is much less than at higher concentrations.

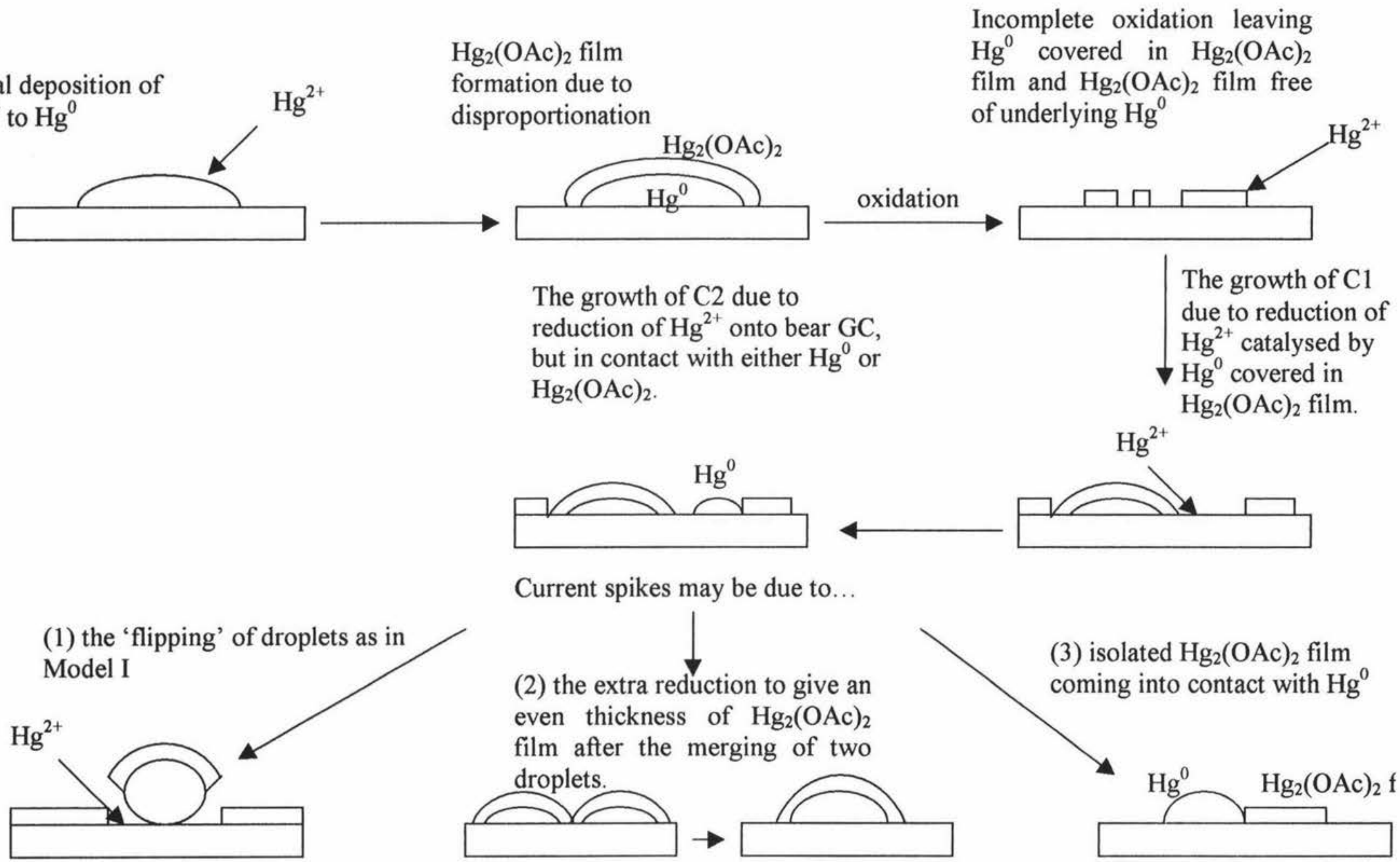

Initial deposition of Hg^{2+} to Hg^{0}

$Hg_2(OAc)_2$ film formation due to disproportionation

Incomplete oxidation leaving Hg^{0} covered in $Hg_2(OAc)_2$ film and $Hg_2(OAc)_2$ film free of underlying Hg^{0}

The growth of C1 due to reduction of Hg^{2+} catalysed by Hg^{0} covered in $Hg_2(OAc)_2$ film.

The growth of C2 due to reduction of Hg^{2+} onto bear GC, but in contact with either Hg^{0} or $Hg_2(OAc)_2$.

Current spikes may be due to…

(1) the 'flipping' of droplets as in Model I

(2) the extra reduction to give an even thickness of $Hg_2(OAc)_2$ film after the merging of two droplets.

(3) isolated $Hg_2(OAc)_2$ film coming into contact with Hg^{0}

Fig 5.13 A schematic diagram for Model II.

Origin of spikes

(1) hemisphere to sphere flipping, or

(2) extra reduction to give even $Hg_2(OAc)_2$ film thickness, or

(3) isolated $Hg_2(OAc)_2$ film coming into contact with Hg^0.

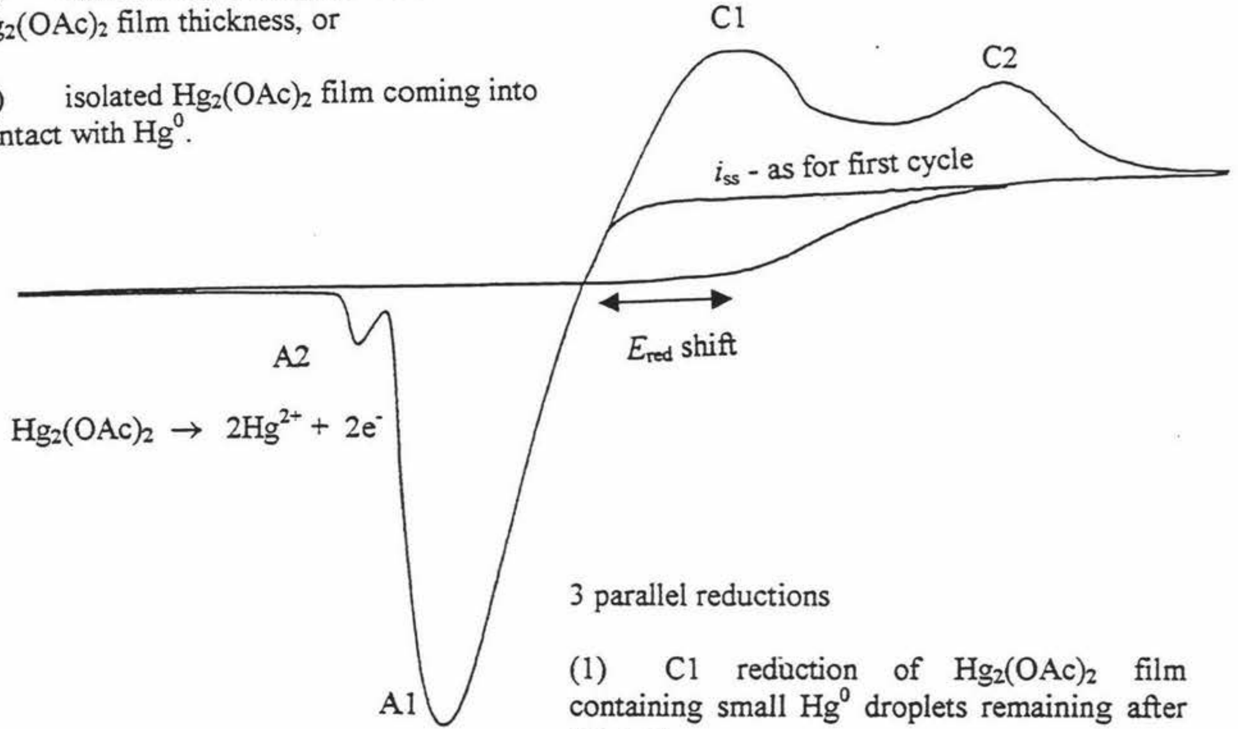

3 parallel reductions

(1) C1 reduction of $Hg_2(OAc)_2$ film containing small Hg^0 droplets remaining after A1, and

(2) C2 reduction of $Hg_2(OAc)_2$ film free of underlying Hg^0 but in contact at edge with Hg^0 or GC, and

(3) $Hg_2(OAc)_2$ free of Hg^0 reducing on GC.

Fig 5.14 A schematic voltammogram for Model II.

The choice of whether or not the electrode undergoes pre-treatment has also been shown to matter. The choice of mechanically-cleaning or electrochemically-cleaning has also been shown to be of concern if the electrode was going to undergo pre-treatment.

The last parameter of the composition of the supporting electrolyte is very important. It is presumed that the disproportionation reaction occurs both in nitrate and acetate but it has been shown here that there is a large difference between what is seen for the deposition of mercury in both of these supporting electrolytes. In acetate the disproportionation product is insoluble and is thought to form a $Hg_2(OAc)_2$ film effecting the further deposition of mercury. This leads to a shift in E_{red} in acetate and the formation of C1, C2 and A2. The disproportionation product in nitrate is soluble so as it is formed it disperses into the bulk not effecting the further deposition of mercury, and hence C1 and C2 are not seen in nitrate solutions of mercury.

A qualitative model has been developed (Model II, section 5.12.2) to account for most of these observations. A quantitative nucleation and growth model has been successfully identified for the hemispherical growth of mercury in ME work where the growth rate is controlled by the small perimeter not covered by a semi-passivating $Hg_2(OAc)_2$ film. This film having been formed by disproportionation and subsequent precipitation.

5.14 Future work

There is a great deal of work that could be undertaken as a result of the finding presented in this thesis.

(i) A detailed study into the effects of all parameters for mercury deposition in nitrate electrolyte.

(ii) A more detailed study into the ME work to elucidate more about the kinetics of $Hg_2(OAc)_2$ film growth.

(iii) Temperature dependence experiments.

(iv) The use of random array microelectrodes (RAM) may be used to explore nucleation rates.

(v) Surface analysis techniques such as scanning electron microscopy (SEM), scanning tunnelling microscopy (STM), and atomic force microscopy (AFM), throughout the deposition stage on microelectrodes to attain visual microscopic conformation of the growth of mercury.

REFERENCES

1. J. Heyrovsky, *Chem. Lists*, 16 (1922) 256.

2. M. Powrbaix, *Electrochim. Acta*, 16 (1971) 173.

3. X. Lu, Z Wang, Z. Geng, J. Kang, J. Gao, *Talanta*, 52 (2000) 411.

4. P. K. Tamrakar, R. C. Pawar, K.S. Pitre, *Rev. Anal. Chem.*, 19 (2000) 31.

5. M. de Sousa, R. Bertazzoli, *Anal. Chem.*, 68 (1996) 1258.

6. J. Wang, "*Electroanalytical Chemistry*", edited by A. J. Bard, Marcel Dekker, New York, 1988, Vol. 16, pp.1-87.

7. M. M. Ghoneim, A. M. Hussanein, E. Hammam, A. M. Beltagi, *Anal. Lett.*, 367 (2000) 378.

8. Attkin, "*Physical Chemistry*" Edition 3, pp. 836.

9. D. A. Skoog and J. J. Leary, "*Principles of Instrumental Analysis*", 4th Edition, Saunders College Publishing, 1992.

10. Frank-Michael Matysik, S. Matysik, A. M. O. Brett, C. M. A. Brett, *Anal. Chem.*, 69 (1997) 1651.

11. C. M. A. Brett, M.B. Garcia, L. J. Quinaz, *Electrochim. Acta.*, 15 (1997) 351.

12. J. C. Ball, R. G. Compton, C. M. A. Brett, *Phys. Chem.*, 102 (1998) 162.

13. C. M. A. Brett, B. Garcia, J. Lima, *Electrochim. Acta.*, 13 (1995) 505.

14. A. Economou, P. R. Fielden, *Analyst*, 121 (1996) 1903.

15. A. Economou, P. R. Fielden, *Talanta*, 46 (1998) 1137.

16. G. Sanna, M. I. Pilo, P. C. Piu, A. Tapparo, R. Seeber, *Anal. Chim. Acta.*, 415 (2000) 165.

17. Christa L. Colyer, Keith B. Oldham, *Electroanal. Chem.*, 290 (1990) 33.

18. F. J. Miller, H. E. Zittel, *Electroanal. Chem.*, 9 (1965) 305.

19. Ikram Morcos, *Electroanal. Chem. And Interfac. Electrochem.*, 50 (1974) 373.

20. W. T. de Vries, E. Van Dalen, *Electroanal. Chem. And Interfac. Electrochem.*, 14 (1967) 315.

21. Wolfgang Frenzel, *Anal. Chim. Acta*, 273 (1993) 123.

22. M. A. Baldo, S. Daniele, M. Corbetta, G. A. Mazzocchin, *Electroanalysis*, 7 (1995) 980.

23. M. Stulikova, *Electroanal. Chem.*, 48 (1973) 33.

24. H. E. Zittel, F. J. Miller, *Anal. Chem.*, 37 (1965) 261.

25. S. Yamada, H. Sato, *Nature*, 193 (1962) 261.

26. J. C. Bokros, *Carbon*, 15 (1977) 355.

27. G. N. Kamau, *Anal. Chim. Acta*, 207 (1988) 1.

28. W. E. Van de Linden, J. W. Dieker, *Anal. Chim. Acta*, 119 (1971) 1.

29. G. M. Jenkins, K. Kawamura, *Material Science*, 5 (1970) 262.

30. G. M. Jenkins, K. Kawamura, *Nature*, 231 (1971) 175.

31. H. Monien, H. Specker, K. Zinke, *Z. Anal. Chem.*, 225 (1967) 342.

32. J. F. Alder, B. Fleet, P. O. Kane, *Electroanal. Chem.*, 30 (1971) 427.

33. C. M. A. Brett, *Electroanalysis*, 11 (1999) 1013.

34. C. M. A. Brett, A. M. O. Brett, Frank-Michael Matysik, S. Matysik, S. Kumbhat, *Talanta*, 43 (1996) 2015.

35. C. M. A. Brett, D. A. Fungaro, J. M. Morgado, M. H. Gil, *Electroanal. Chem.*, 468 (1999) 26.

36. C. M. A. Brett, D. A. Fungaro, *Talanta*, 50 (2000) 1223.

37. J. Wang, J. Lu, S. B. Hocevar, A. M. Percio, *Anal. Chem.*, 72 (2000) 3218.

38. M. Goto, K Ikenoyo, D. Ishii, *Anal. Chem.*, 51 (1979) 110.

39. T. R. Copeland, J. H. Christe, R. A. Osteryoung, R. K. Skogerboe, *Anal. Chem.*, 45 (1973) 2171.

40. A Economou, P. R. Fielden, *Analyst*, 118 (1993) 47.

41. C. D. Evens, I. Nicic, J. Q. Chambers, *Electrochem. Acta.*, 40 (1995) 2611.

42. Personal communication by P. R. Fielden with S. B. Hall, 1998, UMIST.

43. A. Economou, P. R. Fielden, *Trends in Anal. Chem.*, 16 (1997) 286.

44. D. Jagner, L. Renman, S. H. Stefansdottir, *Anal. Chim. Acta*, 281 (1993) 305.

45. A. M. Dobney, G. M. Greenway, *Analyst*, 119 (1994) 293.

46. J. Wang, J. Lu, C. Yarnitzky, *Anal. Chim. Acta*, 280 (1993) 61.

47. J. Wang, J. Lu, L. Chen, *Anal. Chim. Acta*, 259 (1992) 123.

48. A Economou, P. R. Fielden, *Electroanalysis*, 7 (1995) 447.

49. J. Wang, T. Baomin, R. Setiadji, *Electroanalysis*, 6 (1994) 317.

50. C. M. A. Brett, A. M. O. Brett, J. L.C. Pereira, *Electroanalysis*, 3 (1991) 683.

51. C. B. Pascual, V. A. Vicente-Beckett, *Anal. Chim. Acta*, 224 (1989) 97.

52. E. Sahlin, D. Jagner, *Anal. Chim. Acta*, 333 (1996) 233.

53. C. M. A. Brett, A. M. O. Brett, L. Tugulea, *Anal. Chim. Acta*, 322 (1996) 151.

54. G. W. Schieffer, W. J. Blaedel, *Anal. Chem.*, 49 (1977) 49.

55. A. Economou, P. R. Fielden, *Analyst*, 118 (1993) 1399.

56. S. Daniele, C. Bragato, M. A. Baldo, *Electroanal. Chem.*, 439 (1997) 153.

57. S. Mo, J. Na, H. Mo, L. Chen, *Anal. Letters*, 25 (1992) 899.

58. B. Hoyer, T. M. Florence, G. E. Batley, *Anal. Chem.*, 59 (1987) 1608.

59. J. Zen, S. Huang, *Anal. Chim. Acta*, 77 (1994) 77.

60. B. Hoyer, N. Jensen, *Talanta*, 42 (1995) 767.

61. J. Zen, N. Chi, F. Hsu, M. Chung, *Analyst*, 120 (1995) 511.

62. C. Wechter, J. Osteryoung, *Anal. Chim. Acta*, 234 (1990) 275.

63. J. Wang, X. Rongrong, T Baomin, Jianyan Wang, C. Renschler, C. A. White, *Anal. Chim. Acta*, 193 (1994) 43.

64. S. B. O. Adeloju, F. Pablo, *Anal. Chim. Acta*, 270 (1992) 143.

65. C. M. A. Brett and A. M. O. Brett, "*Electrochemistry. Principles, methods and applications*", Oxford University Press Inc., New York, 1993, pp 137.

66. K. R. Wehmeyer, M. R. Deakin, R. M. Wrightman, *Anal. Chem.*, 57 (1985) 1913.

67. P. H. Rieger, "*Electrochemistry*", 2nd edition, Chapman and Hall Inc., 1994, pp. 208.

68. J. Wang, "*Analytical Electrochemistry*", VCH Inc., 1994.

69. V. G. Levich, "*Physiochemical Hydrodynamics*", Prentice-Hall, Englrwood cliffs, NJ., 1962, pp. 62-70.

70. E. Gileadi, "*Electroode kinetics for chemists, chemical engineers and material scientists*", VHC Pubishers Inc., New York, 1993.

71. *C. R. C. Handbook of Chemistry and Physics*, 63rd edn., 1982-1983, pp. D-154 and D-155.

72. J. Koryta, J. Dvorak and L. Kavan, "*Principles of electrochemistry*", 2nd edn., John Wiley and Sons Ltd., England, 1993.

73. P. T. Kissinger and W. R. Heinman, "*Laboratory Techniques in Electroanalytical Chemistry*", Marcel Dekker Inc, 2nd Edn., 1996.

74. J. O'M. Bockris, "*Surface electrochemistry: a molecular level approach*", Plenum, New York, 1993.

75. A. J. Bard and L. R. Faulkner "*Electrochemical Methods; Fundamentals and Applications*", Wiley, New York, 1980, pp 298-304.

76. C. T. Kingzett, *J. Chem. Soc.*, 37 (1980) 792.

77. M. Kaupp, H. Von Schnering, *Inorg. Chem.*, 33 (1994) 4179.

78. S. Sasic, A. M. Antic-Jovanovic, M. G. Jeremic, *Phys. Chem. '98', Int. Conf. Fundam. Appl. Aspects Phys. Chem.*, 4th (1998) 119-121.

79. S. Sasic, A. M. Antic-Jovanovic, M. G. Jeremic, *Chem. Soc., Faraday Trans.*, 94 (1998) 3255.

80. M. Heyrovsky, P. Mader, S. Vavricka, V. Vesela, M. Fedurco, *Electroanal. Chem.*, 430 (1997) 103.

81. F. Zamora, M. Sabat, B. Lippert, *Inorg. Chem.*, 35 (1996) 4858.

82. L. F. Kozin, Y. P. Sushkov, *Ukr. Khim. Zh.*, 57 (1991) 611, as cited in Chemical Abstracts, AN 1992:161070.

83. D. D. Macdonald, "*Transient Techniques in Electrochemistry*", Plenum Press, New York, 1977, pp 397.